Design and Optimisation of Direct-driven PM Variable-Flux Synchronous Generators for Directly Grid-Connected Slip-Synchronous Wind-Turbines

Lilian Livutse Amuhaya

Dissertation presented for the Degree of Doctor of Philosophy in the Faculty of Engineering,
at Stellenbosch University

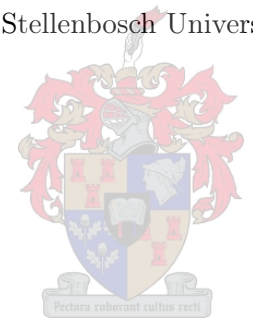

Promoter:
Prof. Maarten J. Kamper

December 2017

Declaration

By submitting this dissertation electronically, I declare that the entirety of the work contained therein is my own, original work, that I am the sole author thereof (save to the extent explicitly otherwise stated), that reproduction and publication thereof by Stellenbosch University will not infringe any third party rights and that I have not previously in its entirety or in part submitted it for obtaining any qualification.

Signature: L. L. Amuhaya

Date: December 2017

Acknowledgements

I wish to thank my supervisor Prof. Kamper for his valuable guidance, knowledge and patience in this work. I am glad that under his guidance I got to understand and appreciate machines as a field on its own, this is from the endless discussions and always having time for any comments and clarifications. For the opportunity to have two prototype generators being funded is all due to my Prof, and I am forever grateful.

I would like to acknowledge Schlumberger Foundation faculty for the future program for research support.

The EMLab group all the conversations and cakes made the clock tick. To all the EM Lab technicians who worked tirelessly in the prototype assembly and mounting.

To my family, parents, brothers and sisters you have walked with me all the steps in very special ways. My husband you have been a pillar. My daughter Amanda, I am indebted to all the times you had to sit in the lab and allowing me to push harder and sometimes take a break. I love you daughty.

Lastly to God the Almighty... You are the main Designer.

Abstract

This dissertation presents design, optimisation and prototype tests of radial-flux, low-speed, permanent magnet (PM) and copper excited, synchronous generators with a new topology. The designed generators are for use in direct-drive directly grid-connected slip-synchronous wind-turbine systems.

For direct-drive systems, (PM) generators deployment is more attractive due to the convenience of high-energy permanent magnet types for example NdFeB.Thus, replacing conventional PM synchronous generators with PM variable flux synchronous generators (PM VFSGs) has recently gained great interest. PM VFSG (have some rotor windings, which result in a flux variation capability and therefore they give better performance in grid compliance than purely PM excited SGs. In addition, they offer better efficiency and reduced mass when compared to purely electrically excited synchronous generators (EESGs).

Using analytical and FEM analysis, the PM VFSG design with non-overlap concentrated windings was carried out applying three optimisation algorithms, i.e. modified method of feasible direction (MMFD), non-sorted genetic algorithm (NSGA II) and particle swarm optimisation (PSO). Using simplified equivalent magnetic circuit and PM properties, an initial iterative preliminary design for the proposed generator was carried out. The rotor field coil analysis was performed using FE analysis in MagNet solver to numerically evaluate four generator designs from a benchmarked surface-PM VFSG calculated analytically. The aim of the electromagnetic analysis is to satisfy a grid compliance design, where flux variation is necessary. The rotor design values changes depending on the amount of magneto-motive force (MMF) required, supplied by magnets and rotor field coils. From the analysed rotor designs, it was found that the rotor slot area is a key constraining factor. Another key outcome of the study is that the location of the PMs on/in the rotor tooth influences the flux linked to the stator . The rotor design corresponding to the lowest rotor copper losses was adopted.

The optimisation procedure uses $d-q$ analysis at steady state and no-load, to investigate the size, efficiency and active mass of 13 kW, 100 kW and 1 MW generators with a base winding of 34/36. The buried-PM topology is found to achieve the least mass and highest efficiency. The outer diameters of the optimised generators have marginal difference with other conventional systems. Compared with other direct drive generator systems, the proposed generator has a larger air-gap diameter and heavier rotor but with comparable total active mass.

The prototype generators were constructed using rare-earth permanent magnets NdFeB-48H with a remanent flux density of 1.41 T. The rotor and stator lamination cores were laser cut but can be punched in mass production. Open-slots with straight teeth were adopted for the stator with double-layer non-overlap concentrated windings. The short

end-winding characteristic of the winding topology enhanced efficiency and lower active mass. Rectangular blocks of permanent magnets with flux in radial direction are used. The surface-PM VFSG topology has the PMs segmented and glued on the rotor tooth surface. On the other hand, the buried-PM VFSG design has full rectangular PMs inserted into the rotor cores. The constructed prototype generator was tested as a three-phase fixed-low-speed generator with varied load conditions under grid compliance. Good correlation in the theoretical prediction and the experimental results were obtained.

Opsomming

Hierdie proefskrif bied ontwerp-, optimalisasie en prototipe toetse van radiale flux, lae spoed, permanente magneet (PM) en koper opgewekte, sinkroniese kragopwekkers met 'n nuwe topologie. Die ontwerpte kragopwekkers is vir gebruik in direkte dryfkrag-verbindings glipsinchroniese windturbinesisteme. Vir direkte dryfstelsels is die implementering van kragopwekkers aantrekliker as gevolg van die gemak van hoë-energie-permanente magneet tipes, byvoorbeeld NdFeB. By die vervanging van konvensionele PM-sinkroniese kragopwekkers met PM-veranderlike flux -sinchroniese kragopwekkers (PM VFSGs) het onlangs groot vertoning gekry. belang. PM VFSG (het 'n paar rotor windinge, wat 'n flux- variasievermoë tot gevolg het en gevolglik gee hulle beter prestasie in rooster-nakoming as suiwer PM-opgewonde SG's. Daarbenewens bied hulle beter doeltreffendheid en verminderde massa in vergelyking met suiwer elektries opgewekte sinkroniese kragopwekkers (EESG's).

Met behulp van analitiese en FEM-analise is die PM VFSG-ontwerp met nie-oorvleuel-gekonsentreerde windings uitgevoer met behulp van drie optimaliserings algoritmes, dws gewysigde metode van uitvoerbare rigting (MMFD), nie-gesorteer genetiese algoritme (NSGA II) en partikel swerm optimalisering (PSO) . Deur gebruik te maak van vereenvoudigde ekwivalente magnetiese stroombaan- en PM-eienskappe, is 'n aanvanklike iteratiewe voorlopige ontwerp vir die voorgestelde generator uitgevoer. Die rotor voedselanalise is uitgevoer met behulp van FE-analise in MagNet-solver om vier generatorontwerpe numeries te evalueer van 'n gekontroleerde oppervlak-PM VFSG wat analities bereken is. Die doel van die elektromagnetiese analise is om 'n rooster nakomingsontwerp te bevredig, waar flux-variasie nodig is. Die rotor ontwerpwaardes verander, afhangende van die hoeveelheid magneto-motiewe krag (MMF) wat benodig word, voorsien deur magnete en rotor veldspoele. Uit die ontleed rotor ontwerpe is gevind dat die rotor gleuf area 'n sleutelbeperkende faktor is. Nog 'n belangrike uitkoms van die studie is dat die ligging van die PM's op / in die rotor tand die vloei wat aan die stator gekoppel is, beïnvloed. Die rotor ontwerp wat ooreenstem met die laagste rotor koper verliese is aangeneem.

Die optimaliserings prosedure gebruik d-q- analise teen bestendige toestand en geen vrag, om die grootte, doeltreffendheid en aktiewe massa van 13 kW, 100 kW en 1 MW kragopwekkers met 'n basiswinding van 34/36 te ondersoek. Die begrawe-PM-topologie is gevind om die minste massa en hoogste doeltreffendheid te behaal. Die buitenste diameters van die geoptimaliseerde kragopwekkers het marginale verskil met ander konvensionele stelsels. In vergelyking met ander direkte dryfgeneratorstelsels het die voorgestelde kragopwekker 'n groter luggaping deursnee en swaarder rotor, maar met vergelykbare totale aktiewe massa.

Die prototipe kragopwekkers is gebou met behulp van seldsame permanente magnete NdFeB-48H met 'n remanent vloeistofdigtheid van 1,41 T. Die rotor- en stator laminerings kern was laser gesny, maar kan in massaproduksie gepons word. Oop gleuwe met reguit

tande is aangeneem vir die stator met dubbel laags nie-oorvleuel gekonsentreerde windings. Die kort einde-kronkelende eienskap van die kronkel topologie het doeltreffendheid en laer aktiewe massa verbeter. Reghoekige blokke van permanente magnete met vloed in radiale rigting word gebruik. Die oppervlak-PM VFSG topologie het die PM's gesegmenteer en vasgeplak op die rotor tand oppervlak. Aan die ander kant het die begraafde PM VFSG-ontwerp volle reghoekige PM's in die rotor kern. Die vervaardigde prototipe kragopwekker is getoets as 'n drie-fase vaste lae spoed generator met gevarieerde laai voorwaardes onder rooster nakoming. Goeie korrelasie in die teoretiese voorspelling en die eksperimentele resultate is verkry.

To Lihabi my mother and daughter, and
T.M Amuhaya, my father.

Contents

List of Figures

List of Tables

Nomenclature

α_{Cu}	Copper mass ratio
α_{Cu}	Copper mass ratio
α_{Cu}	Copper factor
α_{ph}	Angle between subsequent spokes
α_s^e	stator slot angle
β	Current angle
η	Efficiency
μ	permeability
ω_{el}	Electrical speed
ω_m	mechanical speed
ω_s	Synchronous speed
$\phi_{arm,pp}$	Flux per-pole due to armature winding
σ_{Cu}	Copper conductivity
σ_{Ftan}	Tangential stress
$\tau_{m,sp}$	Magnet span
τ_p	Pole-pitch
τ_s	Slot pitch
d	Load angle
l_d, l_q	Flux linkage on $d-$ and $q-$ axis
l_m	PM flux linkage

A_{load}	Electric loading
A_{rs}	Rotor slot area
A_{ss}	Area stator slot
Av	Vector potential
B	Flux density
B_g	Air-gap flux density
$B_{g,av}$	Magnetic loading
B_{pls}	Flux density in the pole-shoe
b_{pls}	Width of the pole-shoe
b_{rs}	Width rotor slot
b_{rt}	Width rotor tooth
b_{ss}	Width stator slot
b_{st}	Width stator teeth
C_{ChCe}	Core loss coefficients
D_g	Air-gap diameter
D_{in}	Inner diameter
D_{out}	Outer diameter
d_{pm}	diameter depth of PM into the rotor tooth
F_f	MMF from rotor field coils
f_s	Frequency
F_{pm}	MMF from PMs
g	Air-gap
G_1	Goodness factor of mass per power (kg/kW)
G_2	Goodness factor of torque per volume (kN/m^3)
G_3	Goodness factor of rotor copper loss to rated power(W/kW)
G_4	Goodness factor of PM mass to volume (kg/m^3)

G_p	Generator periodicity
G_{cs}	Generator coil sections
g_{eff}	Effective air-gap
$gbest$	Global best position
H	Field intensity
h_{rs}	Height rotor slot
h_{rt}	Height rotor teeth
h_{ry}	Height rotor yoke
h_{ss}	Height stator slot
h_{st}	Height stator teeth
h_{sy}	Height stator yoke
I_s	Stator current
I_{rfc}	Current in the rotor field coils
I_{rms}	RMS current
J	Current density
J_r	Rotor current density
J_s	Stator current density
J_s	Stator current density
K_w	Winding factor
K_{ff}	Slot filling factor
L_d, L_q	$D-$ and $q-$ inductances
$L_{r,ew}$	Length of rotor end winding
L_{rfc}	Length of rotor copper coils
L_{stk}	Stack length
m	Number of phases
$M_C u, r$	Mass rotor copper

$M_C u, s$ Mass stator copper

M_p Generator repeatition

M_{core} Core mass

M_{Cu} Mass copper

M_{pm} Mass PM

N_r Rotor turns

p Pole-pair

P_{core} Core loss

P_{Cu} Total copper loss

P_{loss} Total loss in the genrator

P_{out} Output power

P_{rat} Rated power

P_{rfc} Rotor field coils' power

q Slots-per-pole

Q_s Stator slots

Q_{grid} Reactive power requirement

R_g Air-gap radius

R_g Resistance in the air-gap

R_r Rotor resistance

R_s Stator resistence

R_{pm} Resistance in the PMs

R_{rfc} Rotor field coils' resistance

R_{rt} Resistance in the rotor teeth

R_{ry} Resistance in the rotor yoke

R_{st} Resistance in the stator teeth

R_{sy}	Resistance in the stator yoke
T	Torque
V_d, V_q	Voltages in the $d-$ and $q-$ axis'
V_s	Stator voltage
V_{act}	Active volume
V_{core}	Volume of the core
V_{pm}	Volume of PMs
V_{rfc}	Rotor field coils' voltage
V_{rfc}	Voltage in the rotor field coils
V_{rfc}	Volume for rotor copper
ψ_S	Flux linking the stator coils
AF	Axial
DE	Differential Evolutionary
DESM	Double excited synchronous machine
DFIG	Double fed induction generator
DSPM	Double salient permanent machine
EESG	electrically excited syncronous generator
FE	Finite Element
FEM	Finite element method
G_5	Goodness factor of rated torque to square root power losses (kNm/kW)
GA	Genetic algorithm
HEM	Hybrid excited machine

HESMs Hybrid excited synchronous machine

IPM Interior permanent magnet

LCM Least common multiple

LVRT Low voltage ride through

M_{Tot} Total active mass

MMF Magneto-motive force

MMF magneto-motive force

MMFD Modified Method of Feasible Direction

MOPSO multi-objective particle swarm optimisation

N-OCW Non-overlap concentrated winding

NdFeB Neodimium Iron Boron

NSGA-II Non-sorted Genetic Algorithm

$P_{Cu,r}$ Rotor copper loss

PM permanent magnet

PM permanent magnet

PM-VFSGs Permanent magnet variable-flux synchronous generator

PMSG Permanent magnet synchronous generator

PSO Particle Swarm Optimization

RF Radial flux

RS Response surface

S-SG Slip-synchronous generator

SG Synchronous generator

SGs synchronous generators

SUMT Sequential Unconstrained Minimization Technique

TF Transverse flux

TSOs Transmission system operators

VFSG Variable-flux synchronous generator

Chapter 1

Introduction

1.1 Background

As environmental concerns and the need to adapt to the effects of climate change, increased renewable energy generation sources are desirable. To enable the large-scale application of wind energy without compromising power system stability, transmission system operators have decided on grid code specifications for the quality and the form in which power is delivered to the system. Hence, it is preferable that directly grid-connected wind turbine generator systems that can meet these specifications be used.

Thus, replacing conventional PM synchronous generators with PM variable flux synchronous generators (PM VFSGs) has recently gained great interest. PM VFSGs have some rotor winding, which results in flux variation capability and therefore they give a higher performance in grid compliance than purely permanent magnet (PM) excited SGs. In addition, they offer better efficiency and reduced mass when compared to purely electrically excited synchronous generators (EESGs). For the stator design, non-overlap windings are adopted when considering issues in the winding factor, harmonic influence on the PMs and cogging torque.

1.2 Objective

The general objective with this research is to design, optimise, build and test a radial flux, low speed, grid compliant, PM and copper excited, synchronous generator with a new topology. The specific objective is to carry out a design optimisation of this grid-compliant PM VFSG for a 13.3kW, 88rpm wind generator used in slip-synchronous wind turbine application, to study this new topology, the validity of the design optimisation procedure and the closeness of the practical results to theoretical results.

1.3 Main contribution of the thesis

The contribution to design optimisation procedure proposed, is the use of $d-q$ analysis in steady state as well as no-load operation, to meet design and grid code specifications. The optimisation procedure is demonstrated with three different algorithms and it is scalable to higher power levels. The proposed new topology of the grid-compliant generator has a higher efficiency, reduced mass and magnets buried deep in the rotor core.

1.4 Outline of the thesis

The thesis is organized as follows: In Chapter 2 there is an overview of the slip-synchronous wind turbine technology and the various variable flux synchronous generators. Non-overlap concentrated winding is evaluated for the stator design and a pole/slot combination chosen in Chapter 3. In Chapter 4 there is an analytical evaluation of typical VFSG topologies and the results of three topologies are compared. In chapter 5, a FEM analysis of different rotor designs is carried out. In Chapter 6 the focus is on the design optimisation procedures and methods, followed by a presentation of the results and the discussion of optimum designs ranging from 13 kW to 1MW power levels in Chapter 7. A prototype generator and the experience in building is discussed in chapter 8.

1.5 List of publications

1. Amuhaya, L. L and Kamper, M. J, "Design by optimisation of a buried PM variable-flux wind generator for grid connection", in Optimization of Electrical and Electronic Equipment (OPTIM) & International Aegean Conference on Electrical Machines and Power Electonics. (2017), pp. 305--310.

2. Amuhaya, L. L and Kamper, M. J, "Design and optimisation of variable-flux synchronous generators over the grid-code range using analytical and PSO methods", in International Conference on Domestic Use of Energy (DUE), (2017), pp. 160--166.

3. Amuhaya, L. L. and Kamper, M. J., "Effect of rotor field winding MMF on performance of grid-compliant hybrid-PM slip synchronous wind generator", IEEE PES PowerAfrica (2016).

4. Amuhaya, L. L and Kamper, M. J, "Design and optimisation of grid compliant variable-flux PM synchronous generator for wind turbine applications", in IEEE Energy Conversion Congress and Exposition (ECCE), (2015), pp. 829--836.

5. Amuhaya, L. L. and Kamper, M. J., "Design analysis of a hybrid-PM synchronous generator for wind energy applications", 2015 International Conference on the Domestic Use of Energy (DUE) (2015).

6. Erasmus, AS and Amuhaya, LL and Kamper, MJ, "Power factor correction and reactive power control of a slip-synchronous permanent magnet wind generator using variable flux", in Southern African Universities Power Engineering Conference (SAUPEC) (2015).

Chapter 2

Drive-Train for the Generator System Directly Coupled to the Grid

This chapter is a review of the state of the art in direct drive and directly grid-connected generator systems. There is an overview of the wind-turbine systems (WTS), and various generator topologies that are applied in the system are described. Examples of the direct drive generator topologies depending on their flux direction are presented together with their advantages. Various direct-grid connected systems are briefly described. Then control strategies are described and how they impact on the grid code requirements. Finally, variable flux synchronous generators (VFSG) are discussed.

2.1 Wind turbine concepts

Various wind turbine systems (WTS) are explored [1–6] with increase in wind energy production. to satisfy these grid requirements and standards, the WTS influence on total weight of the nacelle, cost, reliability ease of maintenance and yearly energy yield. The type of generator varies depending on the wind turbine system and grid integration as shown in Figure 2.1. A geared system has a high speed rotor of the generator connected to the turbine blades through a gearbox as shown in Figures 2.1a,-c. This allows them to achieve the required low speed and high torque (examples are Figures 2.1.a - SCIG, 2.1.b - DFIG, 2.1c - PMSG). Direct-drive synchronous generators are a trend in the turbine [3, 4]. Connection to the grid for these direct-drive turbine systems is through converters, or the use of capacitor and inductors. As the wind energy penetration into the power system has led to strict grid code requirements being set. This has led to other studies on how the grid connection can be achieved such as the slip-synchronous wind turbine system [5, 6] and such a topology considered in this research is as shown in Figure 2.2 .

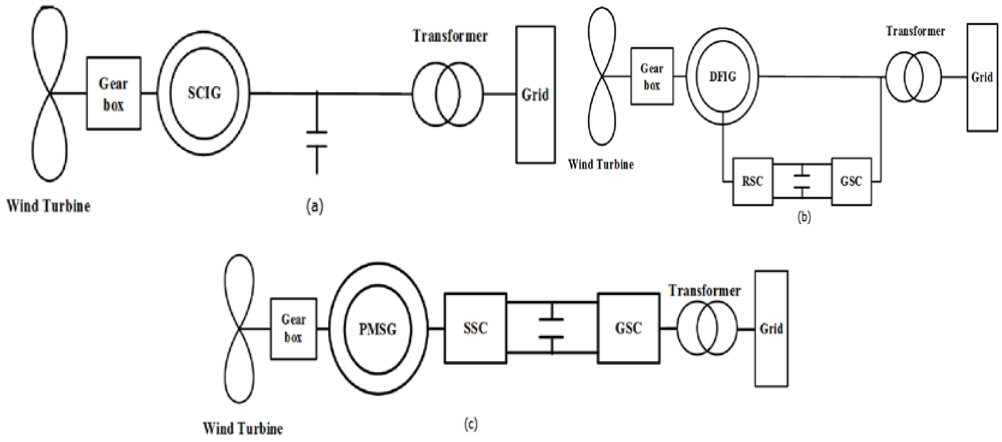

Figure 2.1: Illustration of wind turbine concepts of the common generator types and grid connections.

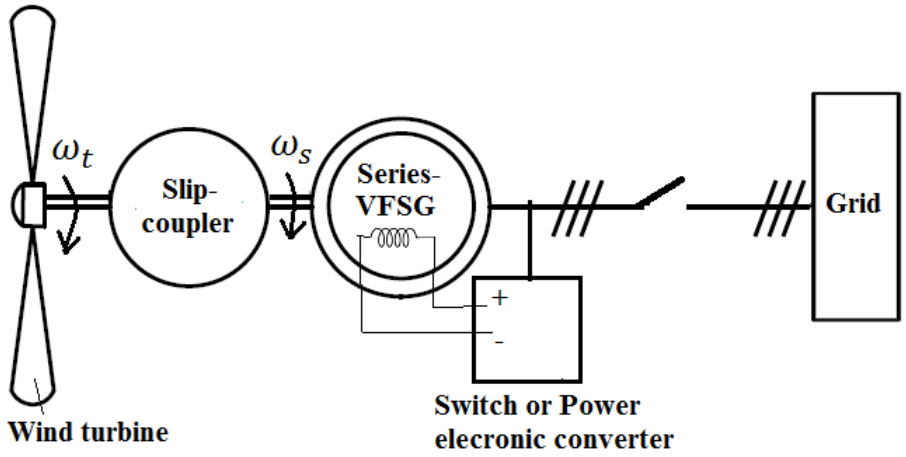

Figure 2.2: Direct drive slip-synchronous wind turbine system for the studied generator

2.2 The Slip synchronous wind turbine system

The slip synchronous wind turbine system illustrated in Figure 2.2, is a direct drive system consisting of a horizontal axis turbine, a slip-coupler, the rotor which is connected to the turbine, and a synchronous generator, with its stator directly connected to the grid.

The mechanical to electrical conversion of the slip-synchronous wind turbine system is performed by the slip-coupler and the PM VFSG. The slip-coupler is an induction generator the rotor of which is short-circuited and mechanically connected to the wind-turbine. It rotates at a slip speed with respect to the PM VFSG which rotates at a synchronous speed. Therefore, the voltage induced in the slip-coupler is at slip-frequency.

The supply of the rotor field coils is separately done from either a battery source or a power-electronic converter with a low power rating. By utilizing the rotor field current, PM VFSGs provide a more efficient system with substantial advantages over competing grid

Figure 2.3: Electrically excited direct drive wind generator type E-126 from Enercon.

compliant wind-turbine systems [6].

2.3 Direct drives

The number of wind turbine installations has increased greatly during the past years. Most of the installed wind turbines have a gearbox enabling a generator to rotate at high speed. A survey of the statistical data of wind power turbine failures and downtime shows that the gearbox is the most troublesome component in a typical turbine: The gearbox is responsible for 20 % of the total downtime and requires in average 256 hours of reparation time per failure [2, 7].

Direct drive wind turbine systems require a low rotating speed and a high torque. The emergence of PM machine technology in the recent past offers another alternative. PM machines can rotate directly at low speed and high torque, making it possible to eliminate the gearbox in the drive (Figure 2.1.c). Depending on the turbine size, the power of the generator can be from a few kilowatts to several megawatts. The nominal shaft speed of large direct drive wind turbines is approximately 10 - 25 rpm at optimum wind speed.

Generators for direct-drive wind turbines are widely studied and some have already been manufactured. Synchronous generator types are widely used in direct drive wind turbine systems. They can be either electrically excited such as Enercon 4.5 MW or PM excited as shown in Figures 2.3 and 2.4 (courtesy pictures) with power ratings of 7.5 MW and 6 MW respectively. Some manufacturers also make use of induction generators i.e. direct-

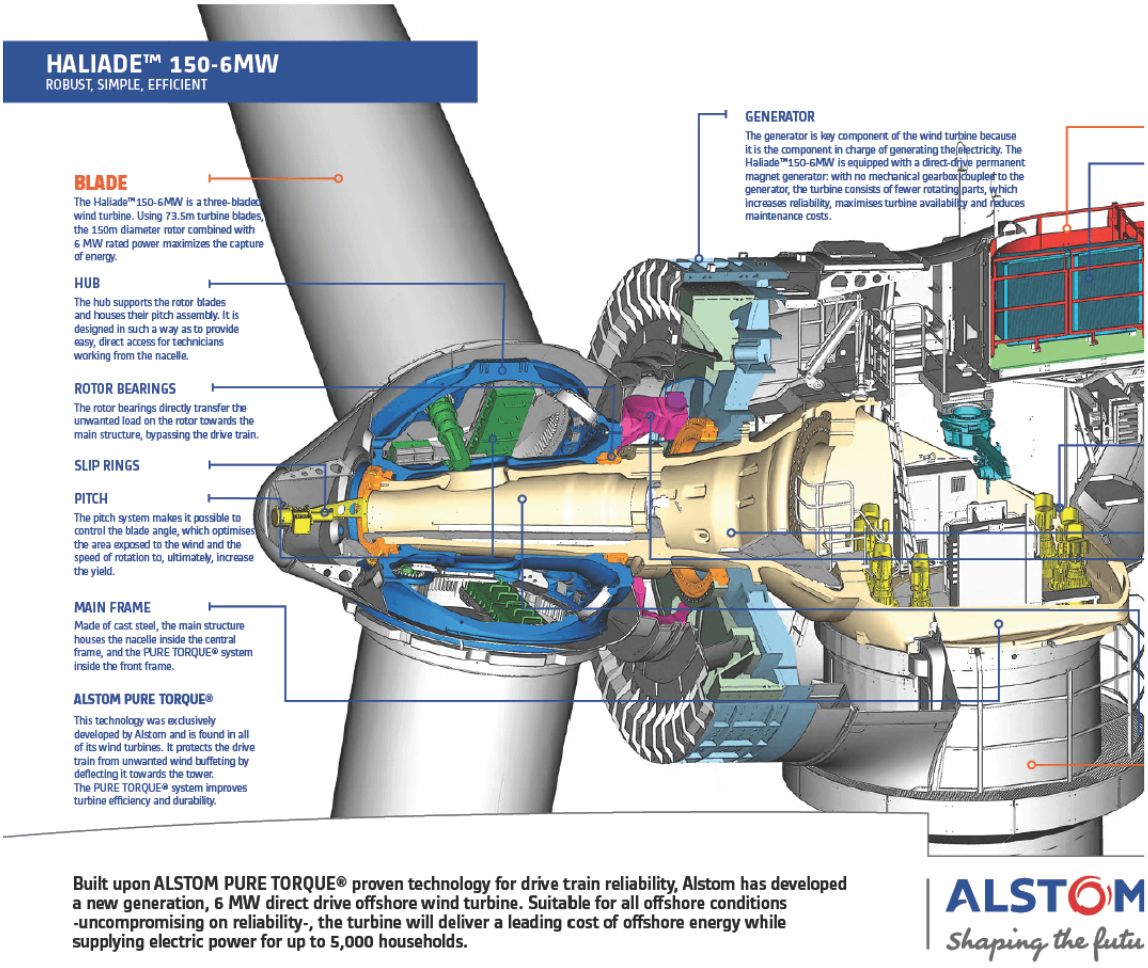

Figure 2.4: PM excited direct drive generator courtesy Alstom-Hallade 6 MW.

drive doubly-fed induction generator (DFIG) in a 2 MW turbine. Nevertheless, PM excited generators offer a significant weight reduction compared to EESGs or DFIGs, which is of significance for the nacelle placement of the generator.

2.3.1 Advantages of direct drives

Direct drives have many advantages over geared drives, as a result of the simplified transmission system with fewer components. These advantages include:

- Lower maintenance costs - A gearbox requires regular lubrication maintenance to reduce friction.
- Reduced noise - Mechanical parts of the transmission system such as gearbox, belts or pulleys are sources of noise. With fewer mechanical parts, the direct drives may thus be less noisy.

- Higher efficiency - Removing the gearbox means also removing a potential cause of friction losses.
- Increased reliability - Lack of a gearbox, results in elimination of its associated failures, and thus a drive with a longer lifetime.
- Lower mass- This can be achieved when compared to all the components of a geared drive.

Other merits in direct drives are specific to the examples as provided in the examples. Notwithstanding, the direct drives have disadvantages such as large generator diameters, turbine support structure issues, difficulty to transport the parts to sites.

2.3.2 Examples of direct drive wind generators

Some examples of direct-drive wind-turbine systems with PM generators in the market are listed below, which are dependent on the flux direction in the generator:

• Radial-flux (RF) - RF generators are quite common in direct-drive wind turbines. The simplicity of the flux direction/ orientation makes it a favourite choice for double-excited generators, as discussed in [8–11]. One of the largest direct-drive wind turbines with its 7.58MW generator is E-126 which is PM excited is shown in Figure. 2.3. Details of a design of a wind turbine along with its RF generator consisting of a DFIG can be found in [12]. A detailed design and optimisation of a 15 kW direct drive directly grid-connected wind turbine system is discussed in [5, 13].

• Axial-flux (AF) - AF generators are also widely investigated [14, 15] and manufactured by some wind-turbine producers.

• Transverse-flux (TF) - TF machines are interesting because of their high torque density [16]. Several research studies have been carried out [16–18] on them. The unique feature of a TF machine that distinguishes it from RF machines is the decoupled nature of the magnetic and electric loading, which can be set independently. This allows the TF machines to attain higher torque densities. At the time of writing, no large wind turbines (over 1 MW) equipped with TFPM generators have been installed. TFPM generators with a power of up to 10 kW have been built with the goal of the commercial production of higher power generators.

2.4 Grid Connection and grid-code specifications

To enable the large scale application of wind power, grid code rules and regulations are stipulated by transmission system operators (TSOs) to ensure safety and no compromise to the electric network. Wind-turbines are required by the modern grid-codes specifications as a renewable plant to:

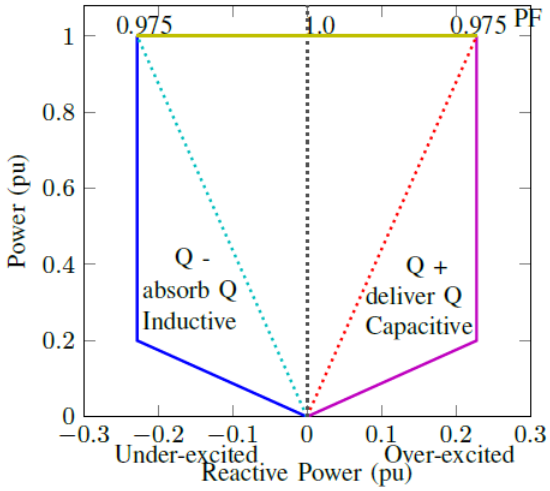

Figure 2.5: Grid code requirements of power-factor and reactive power control for sub 100 KW generators as per South african grid-code requirement.

1. Provide fault-ride-through capability (low voltage ride through (LVRT)) - they have to stay connected and contribute to the grid in case of a disturbance such as a voltage dip.

2. Supply both active and reactive power for voltage and frequency control in the power system similar to conventional power sources.

The specifications for a sub 100 kW wind turbine system are as shown in Figure 2.5.

2.4.1 Examples of direct grid-connected wind turbine systems

Wind-turbine systems that are directly grid-connected include slip-synchronous generator systems [5, 6, 10], as shown in Figure 2.2, those which use a spring and damper system [19], and those which use a hydro-dynamically controlled gearbox [20]. Recent developments in direct drive directly grid-connected wind turbine systems have led to a renewed interest in grid-connected PM generators as the issues of grid instability are addressed [6, 21, 22].

2.5 Variable-Flux Synchronous Generator types

As discussed earlier, direct drive systems are characterised by large diameters and are heavy. To minimise mass, PMs are adopted. The high density permanent magnets as a source of excitation, offer advantages such as higher efficiency and reliability. However, their constant MMF supply is a drawback to the direct grid-connection of a wind turbine system. To assist in achieving flux variation, the use of field coils is essential. Such machines that have the capability to vary their flux are termed variable flux machines, double excited synchronous machines (DESM) [9, 23], hybrid excited synchronous machines (HESMs) [24] or mixed-pole

hybrid machines as in [25]. In this dissertation these machines are termed as variable flux synchronous generator (VFSG).

2.5.1 Electrical Excited machines

These machines form the conventional synchronous generator types. They use field coils conventionally from copper as the source of excitation. In this dissertation they are reffered to as non-PM VFSG. They have the merits of variable flux capability, These generators have been in use with gearboxes as medium or high speed generators. They are a difficult choice for direct drive wind turbine systems but Enercon has a 4.5 MW EESG installed this is due to the weight issues that are associated with these generator types. Introduction of PMs into the SG can increase the efficiency of the non-PM VFSG as well as mass reduction from a reduced pole-pitch size, as studied in this research.

2.5.2 PM-variable flux machines

This type of machines have the flux from the PMs adjusted by means of either hybrid-excitation [8, 21, 22, 25–27], mechanical adjustments [28–32] or other means of adjustments [33–35]. The hybrid-excited machines (HEM) have their flux variation from field coils. They are further grouped depending on the location of the MMF sources or the type of connection.

2.5.2.1 Series or parallel excitation of the MMF sources

Double excited or hybrid excited machines have a combination of the MMF sources, the magnetic circuits of which can be divided into series- or parallel- excited depending on the flux paths. For series connected MMF sources, the PMs and field excitation coils have their flux in series or the flux produced by the field excitation goes through the PMs. The advantages of series-DESGs include simple topology, good flux variation capability (both boosting and weakening) and the hybridization of the MMF sources has little effect on torque density. The main drawback in this flux variation method is the demagnetisation risk. Examples include the double excited synchronous machine (DESM) of [23] and double salient permanent machine (DSPM) of [36] as shown in Figure 2.6.

In the parallel connected MMF group, the flux from the respective MMF sources have their own paths. It is the most common connection adopted for several studies due to no risk of demagnetisation.

2.5.2.2 Location of the MMF sources

The machines in this category can be classified into stator excited [37, 38] or rotor excited [6, 21, 23] depending on the location of the MMF sources. However, there are some machines with either of the MMF sources in either the stator or rotor as depicted in Figure 2.7.

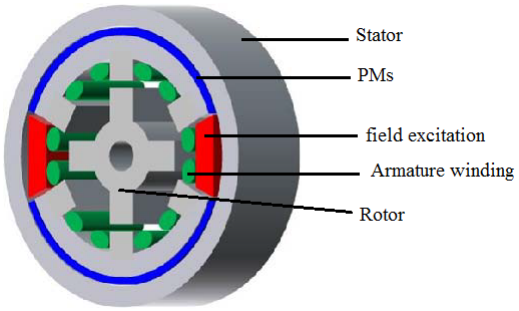

(a) Stator excited DSPM [36]

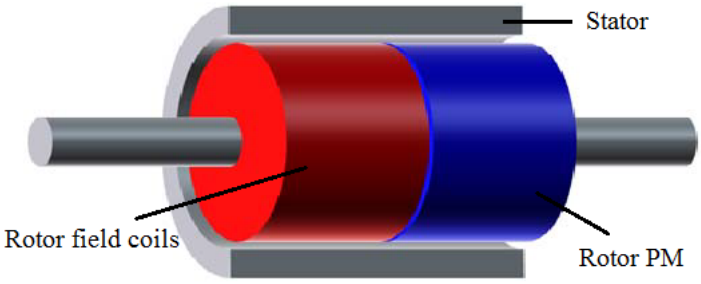

(b) Inner Rotor PMs and rotor field coils

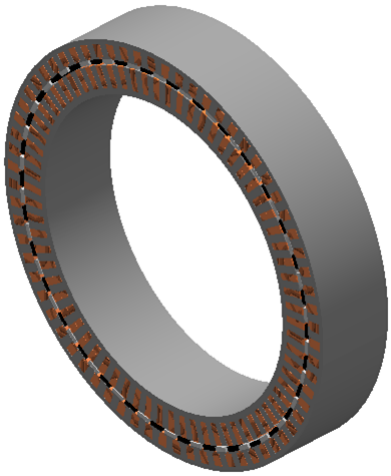

(c) Outer rotor with PMs and rotor field coils

Figure 2.6: Double excited machines with MMF sources connected in series (a) and (c) and parallel connection in (b) [36].

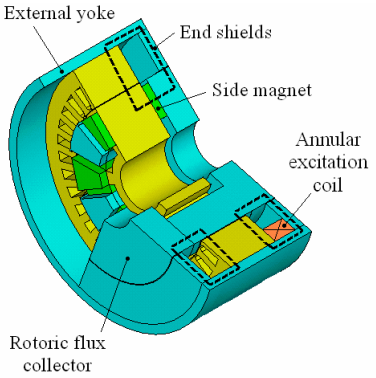

(a) Homopolar flux path

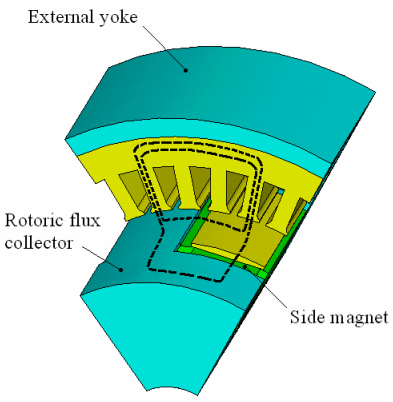

(b) Bipolar flux from PMs

Figure 2.7: Fluxes homopolar path [24].

The rotor excited machines have a relatively simple topology however, there is need for slip-rings for the rotor field coils. The stator excited machines have all the MMF sources i.e field coils and PMs in the stator. They have the merits of a simple and robust rotor, good flux variation capabilities and high torque density. An example is the double salient PM machine (DSPM) in [36], where both excitations are in the stator and the need for sleep-rings is avoided. In this topology, the use of flux focussing is made, and ferrite magnets can be used for excitation purposes.

2.5.2.3 Mechanical adjustment for flux variation

For these machine types, the mechanical structure is adjusted to regulate the flux. These adjustments include:

- Increase in air-gap size as introduced in an axial PM machine [28], provides flux enhancement or weakening. The current is supplied from the stator and the machine's air-gap is adjusted by a spring and a hinge.
- Additional leakage paths that is applicable only for flux weakening purposes. Leakage paths are introduced to adjust the PM flux [29, 39]. End plates are also used to cause a short circuit leakage path. During normal operation the end plates are positioned far with the help of springs and full flux is provided for by the PMs. If flux weakening is necessary, the end-plates are pushed into the rotor to provide a leakage path.
- Adjustment of flux barriers has been proposed in literature to alter the leakage paths of flux barriers. An example is a low speed rotor Interior permanent magnet (IPM) machine [30], iron segments of which are located outside the flux barriers. The segments are pushed into the barriers, as the rotor speed increases, to provide the PM flux with a leakage path.
- Rotation of rotor or stator sections as described in [31, 32].

2.5.2.4 Other machines with special means of flux variation

Some PM machines have two sets of 3-phase armature winding [33]. The flux variation in this machine is such that the two sets of winding operate individually or together in a series connection.

Another machine type is where Alnico magnets are magnetised and de-magnetised using a short pulse of negative $d-axis$ current [35], and reported to have effective flux variation. The complex mechanism could have an effect on the torque density and the manufacturability of such machines.

2.6 Conclusions

An overview of the currently used wind turbine systems is described with focus on direct drives and directly grid connected systems. Different variable flux machines are explored with regard to the ways in which the flux-variation is achieved. It is concluded that some of the designs, with the mechanical adjustments or special means have complicated structures and control hence not desirable in this research. A rotor-excited, series-connected MMF paths is chosen for further analysis.

Chapter 3

Non-Overlap Concentrated Winding for stator design

Direct drive wind generators are characterised by large diameters. The design and analysis of such generator models inherently require effective inter procedural analysis and choice of stator design. There are several existing literature [15, 40–45] and software tools such as Emetor on non-overlap concentrated windings (N-OCW) showing the merits of the winding topology and wide application usage. The study and analysis were carried out to support the choice of stator design. In this chapter, N-OCW details and features useful in this research, which include the choice of pole/slot combination for the generator design, manufacturability and unbalance magnetic effects are described.

N-OCW also termed as fractional slot winding has been widely used in the design of permanent magnet machines for its low cogging torque, fault tolerant and easy manufacturing features. It also has short end-windings compared to distributed winding, resulting in low copper losses [40, 44].

3.1 Non-overlap concentrated winding(N-OCW)

PM generators for low-speed and direct-drive applications are characterised by the high number of poles of the machine. For a multi-phase machine with a design where the number of stator slots Q_s is close to or equal to the number of poles $2p$, the non-overlap concentrated winding is particularly suitable. This is due to the slots-per-pole q always being lower than 1 as

$$q = \frac{Q_s}{2pm} \leqslant 1 \tag{3.1}$$

The τ_s and the stator slot angle are key design parameters for the armature winding. They are calculated from the number of armature slots, poles and the D_g as

$$\tau_s = \frac{\pi D_g}{Q_s} \tag{3.2}$$

and

$$\alpha_s^e = \frac{2\pi p}{Q_s} \tag{3.3}$$

Therefore for a small pole-pitched topology, the slot size is also limited, however for the three-phase being studied here as shown in (3.1), space in the slots is not an issue.

Armature windings having $q < 1$ are referred to in literature [42] in various ways that include: fractional-slot pitch concentrated windings [44], tooth concentrated windings [43], concentrated winding [15], fractional slot concentrated windings [45], fractional slot wound [40], fractional-slot with non-overlapped coils [41].

Concentrated windings used to refer to windings having one slot per pole per phase, but in recent years, the term is largely used for windings that are wound (concentrated) around the tooth, i.e. with no overlapping. On the other hand, for the fractional slot windings type, it is possible for both overlapping and non-overlapping options. In this dissertation, the term non-overlap concentrated winding is used to refer to non-overlapping tooth wound coils with a double layer.

The merits of the N-OCW are shorter end turns, higher efficiency, higher power density, higher slot fill factor, lower manufacturing cost, better flux-weakening capability resulting in wider constant power vs. speed range, fault-tolerance and a smooth torque [15, 40, 42, 44, 45]. However, the N-OCW presents challenges that include the presence of high MMF harmonic [40], large synchronous inductance and a lower winding factor. These challenges are mitigated by the choice of a pole slot combination with a high winding factor, high least common multiple (LCM) value and a machine periodicity greater than one, as discussed later in the chapter.

3.1.1 Generator periodicity

For low speed machines that have a high pole number, the generator can have coil sections equal to

$$G_{cs} = gcd(Q_s, 2p) \tag{3.4}$$

where the winding repeats itself either with positive or negative periodicity (also referred to as base winding). Whereas the full machine/generator is repeated by factor

$$M_p = gcd(Q_s, p) \tag{3.5}$$

and a periodicity value

$$G_p = \frac{G_{cs}}{M_p}. \tag{3.6}$$

Positive and negative periodicity is indicated by $G_p = 1$ and $G_p = 2$ respectively. The number of stator slots and poles constitutes a fraction mq that consists of two integers with no common factor that takes the form

$$mq = \frac{Q_s}{2p} = \frac{n_{mq}}{d_{mq}}. \tag{3.7}$$

that consists of d_{mq} poles and n_{mq} slots. For each generator section (G_{cs}) with d_{mq} poles and n_{mq} slots, the phase inductances and subsequently $d-$ and $q-$axis inductances are equal.

3.2 Choice of pole-slot combination

The choice of pole numbers is dependent on the rated speed of the generator (turbine) and grid frequency. With the arbitrary number of poles, a slot combination for this poles is then selected depending on the winding factor, LCM and machine periodicity.

3.2.1 Star of slots

The design of the winding is used by means of star-of-slots [40], where the main EMF harmonics phasor is represented for each individual coil in a phase. For a given pole-slot combination, the corresponding star-of-slot is characterised by $^{Q_s}/_{M_p}$ spokes consisting of M_p phasors. The angle between the neighbouring spokes is

$$\alpha_{ph} = \frac{2\pi M_p}{Q_s}, \tag{3.8}$$

and the electrical angle between the EMF phasors of two successive slots is as given in 3.3. For $^{Q_s}/_{M_p} = i \cdot m$ for $i = 1, 2, 3, \ldots$ then each phase has equal number of phasors (for an $m-$phase generator). This condition must be satisfied for the pole-slot combination to have a feasible winding scheme.

3.2.2 Winding factor

The fundamental winding factors for different combinations of pole and slot numbers are given in Table 3.1 for double-layer winding from 60 to 90 poles, and in Table 3.2 for the single-layer winding. For the pole/slot combinations, the M_p value is used to determine the harmonic effects in the generator.

Modular PM machines have an MMF distribution with fewer poles than rotor poles Thus, the MMF harmonic component that interacts in the mean torque production is not the fundamental but a higher harmonic component of the same order as the number of pole pairs p/2. It is then called the main harmonic component or synchronous frequency component. The order of the synchronous frequency component for the 68-pole, 72-slot

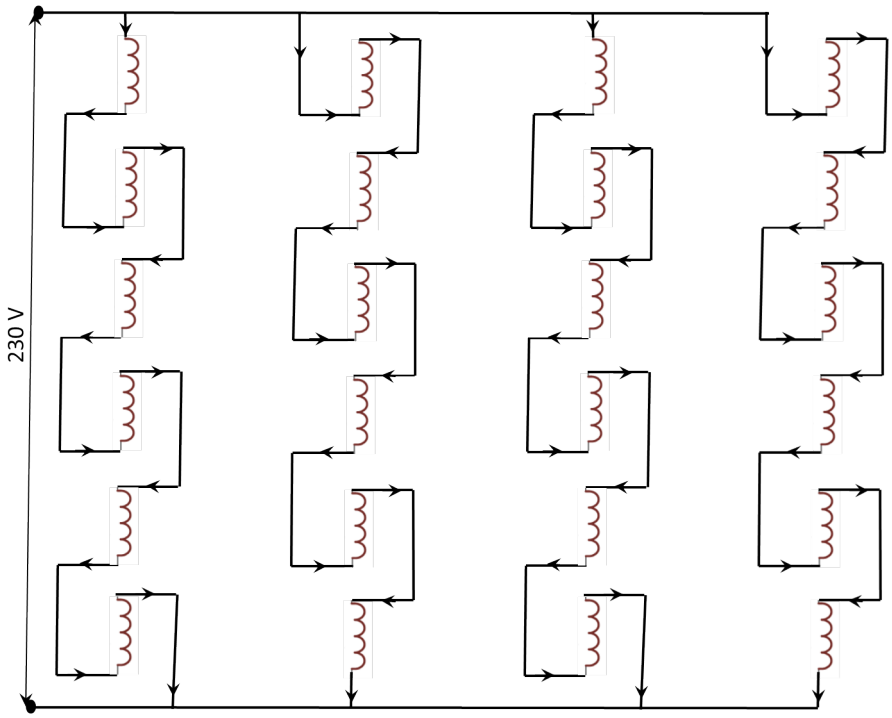

Figure 3.1: Stator coil connection for each of the 3-phases constituting a total of 24 coils in 4 parallel paths (each path has 6 coils).

machine is then The corresponding winding factor is then called the winding factor of main harmonic.

3.2.3 LCM values and machine sections

According to the turbine specifications provided, the generator could have pole numbers between 60 and 90 the corresponding winding factors of which are presented in Table 3.1, with their corresponding slot numbers. The generator can be sectioned depending on the G_s as shown in Table 3.4. For the 68/72 pole slot generator choice, it has four generator sections and negative periodicity as from (3.6). The higher number of the generator sections yields a design with a balanced magnetic pull.

The LCM values are critical for determining the cogging torque of the generator. The higher this value the better the performance of the pole/slot combination with regard to cogging torque. The LCM values for the high pole slot combination are presented in Table 3.3.

The winding for the chosen pole-slot combination is as shown in Figure 3.1, where each phase has 6 coils and 4 parallel paths, a total of 24 coils, and they are wound as shown in the Figure 3.1.

Table 3.1: Winding factors for double-layer varied pole-slot combinations.

$Q_s \diagdown poles$	60	62	64	66	68	70	72	74	76	78	80	82	84	86	88	90
51	-	0.901	0.880	-	0.866	0.796	-	0.725	0.686	-	0.599	0.552	-	0.480	0.485	-
54	0.945	0.930	0.915	0.902	0.877	0.854	0.866	0.798	0.766	0.735	0.695	0.656	0.617	0.571	0.525	0.5
57	-	0.946	0.937	-	0.912	0.894	-	0.852	0.866	-	0.770	0.737	-	0.666	0.627	-
60	-.	0.954	0.951	-	0.936	0.933	-	0.892	0.874	-	0.866	0.801	-	0.742	0.711	-
63	0.953	0.955	0.955	0.953	0.948	0.945	-	0.919	0.905	0.890	0.870	0.850	0.866	0.802	0.775	-
66	-	0.951	0.954	-	0.954	0.951	-	0.938	0.928	-	0.903	0.887	-	0.849	0.866	-
69	-	0.943	0.945	-	0.955	0.955	-	0.949	0.943	-	0.925	0.913	-	0.884	0.867	-
72	0.933	0.933	0.945	0.949	**0.953**	0.954	-	0.954	0.953	0.949	0.945	0.933	0.933	0.911	0.902	-
75	-	0.920	0.930	-	0.945	0.951	-	0.955	0.955	-	0.951	0.945	-	0.930	0.920	-
78	-	0.906	0.917	-	0.934	0.943	-	0.952	0.954	-	0.954	0.952	-	0.943	0.936	-
81	0.877	0.891	0.904	0.915	0.925	0.933	0.945	0.946	0.950	0.954	0.955	0.955	0.954	0.951	0.946	0.945
84	-	0.875sl	0.890	-	0.913	0.933	-	0.939	0.945	-	0.953	0.954	-	0.954	0.953	-
87	-	0.859	0.874	-	0.898	0.910	-	0.923	0.936	-	0.947	0.951	-	0.955	0.955	-
90	0.866	0.843	0.858	0.874	0.886	0.902	-	0.918	0.927	0.936	0.946	0.946	0.951	0.953	0.955	-
93	-	0.866	0.843	-	0.871	0.884	-	0.906	0.916	-	0.932	0.939	-	0.948	0.952	-
96	-	0.811	0.866	-	0.857	0.870	-	0.894	0.905	-	0.933	0.930	-	0.942	0.949	-
99	0.778	0.795	0.811	0.866	0.842	0.856	-	0.881	0.892	0.903	0.912	0.920	0.928	0.935	0.945	-
102	-	0.780	0.796	-	0.866	0.841	-	0.868	0.880	-	0.901	0.910	-	0.926	0.933	-
105	-	0.764	0.81	-	0.812	0.866	-	0.854	0.866	-	0.890	0.900	-	0.917	0.9245	-
108	0.735	0.749	0.766	0.783	0.798	0.813	0.866	0.841	0.854	0.867	0.877	0.888	0.902	0.907	0.915	0.933

Table 3.2: Winding factors for single-layer configuration

$Q_s \diagdown poles$	60	62	64	66	68	70	72	74	76	78	80	82	84	86	88	90
54	0.945	0.930	0.915	0.902	0.877	0.854	0.866	0.798	0.766	0.735	0.695	0.656	0.617	0.571	0.525	0.5
60	x	0.955	0.951	-	0.936	0.966	-	0.893	0.874	-	0.866	0.802	-	0.742	0.711	-
66	-	0.951	0.954	x	0.954	0.951	-	0.893	0.928	-	0.903	0.887	-	0.849	0.866	-
72	0.966	0.933	0.945	0.958	0.956	0.955	x	0.955	0.956	0.958	0.945	0.933	0.966	0.912	0.902	-
78	-	0.906	0.917	-	0.936	0.943	-	0.952	0.954	x	0.954	0.952	-	0.943	0.936	-
84	-	0.876	0.890	-	0.913	0.966	-	0.940	0.945	-	0.953	0.955	x	0.955	0.953	-
90	0.866	0.843	0.858	0.874	0.886	0.902	-	0.918	0.927	0.936	0.945	0.946	0.951	0.953	0.955	x
96	-	0.812	0.866	-	0.859	0.870	-	0.894	0.907	-		0.966	0.931	-	0.943	0.958-
102	-	0.780	0.796	-	0.866	0.841	-	0.868	0.880	-	0.907	0.910	-	0.926	0.933	-
108	0.735	0.749	0.766	0.783	0.798	0.813	0.866	0.841	0.854	0.867	0.877	0.888	0.902	0.907	0.915	0.933

Table 3.3: LCM factors for the varied pole-slot combinations.

Q_s poles	60	62	64	66	68	70	72	74	76	78	80	82	84	86	88	90
51	-	3162	3264	(1122)	204	3570	(1224)	3774	3876	1326	4080	4182	(1428)	4386	1	-
54	5401	1672	1728	594	1836	1890	216	1998	2052	702	2160	4182	756	2322	2	18
57	(1140)	13534	3648	(1254)	3876	3990	(1368)	4218	228	(1482)	4560	4674	(1596)	4902	1	-
60	-x	1860	960	(660)	1020	420	(360)	2220	1140	(780)	240	2460	(420)	2580	4	-
63	1260	3906	4032	1386	4284	630	(504)	4662	4788	1638	5040	5166	252	5418	1	-
66	(660)	2046	2112	x	2244	2320	(792)	2442	2508	(858)	2640	2706	(924)	2838	22	-
69	(1380)	4278	4416	(1518)	4692	4830	(1656)	5106	5244	(1794)	5520	5658	(1932)	5934	1	-
72	360	2232	576	792	**1224**	2520	x	2520	1368	936	720	2952	504	3096	8	-
75	300)	4650	4800	(1680)	5100	1050	(1800)	5500	5700	(1950)	1200	6150	(2100)	6450	1	-
78	(780)	2418	2496	(858)	2652	2730	(936)	2886	2964	x	3120	3198	(1092)	3354	2	-
81	1620	5022	5184	1782	5508	5870	648	5994	6156	2106	6480	6642	2268	6966	1	9
84	(420)	2604	1344	(924)	1428	420	(504)	3108	1596	(1092)	1680	3444	x	3612	4	-
87	(1740)	5394	5568	(1914)	5916	6090	(2088)	6438	6612	2262	6960	7134	(2436)	3612	1	-
90	180	2790	2880	990	3060	630	(360)	3330	3420	1170	720	3690	1260	3870	2	x
93	(1860)	186	5952	(2046)	6324	6510	(2232)	6882	7068	(2418)	7440	7626	(2604)	7998	1	-
96	(480)	2976	192	(1056)	1632	3360	(288)	3552	1824	(1248)	480	3936	(672)	4128	8	-
99	1980	6138	6336	198	6732	6930	(792)	7386	7524	2574	7920	8118	2772	8514	11	-
102	(1020)	3162	3264	(1122)	204	3570	(1224)	3774	3876	(1326)	4080	4182	(1428)	4386	2	-
105	(420)	6510	6720	(2310)	7140	210	(2520)	7770	7980	(2730)	1680	8610	(420)	9030	1	-
108	540	3348	1728	1188	1836	3780	216	3996	2052	1404	2160	4428	756	4644	4	18

Table 3.4: Machine periodicity for varied pole slot combinations

$Q_s \setminus poles$	60	62	64	66	68	70	72	74	76	78	80	82	84	86	88	90
51	-	1	1	-	17	1	-	1	1	-	1	1	-	1	1	-
54	6	2	2	6	2	2	18	2	2	6	2	2	6	2	2	18
57	-	1	1	-	1	1	-	1	19	-	1	1	-	1	1	-
60	-.	2	4	-	4	10	-	2	4	-	20	2	-	2	4	-
63	3	1	1	3	1	7	-	1	1	3	1	1	21	1	1	-
66	-	2	2	-	2	2	-	2	2	-	2	2	-	2	22	-
69	-	1	1	-	1	1	-	1	1	-	1	1	-	1	1	-
72	12	2	8	6	**4**	2	-	2	4	6	8	2	12	2	8	-
75	-	1	1	-	1	5	-	1	1	-	5	1	-	1	1	-
78	-	2	2	-	2	2	-	2	2	-	2	2	-	2	2	-
81	3	1	1	3	1	1	9	1	1	3	1	1	3	1	1	9
84	-	2	4	-	4	14	-	2	4	-	4	2	-	2	4	-
87	-	1	1	-	1	1	-	1	1	-	1	1	-	1	1	-
90	30	2	2	6	2	10	-	2	2	6	10	2	6	2	2	-
93	-	31	1	-	1	1	-	1	1	-	1	1	-	1	1	-
96	-	2	32	-	4	2	-	2	4	-	16	2	-	2	8	-
99	3	1	1	33	1	1	-	1	1	3	1	1	3	1	11	-
102	-	2	2	-	34	2	-	2	2	-	2	2	-	2	2	-
105	-	1	1	-	1	35	-	1	1	-	5	1	-	1	1	-
108	12	2	4	6	4	2	36	2	4	6	4	2	12	2	4	18

3.3 Manufacturing methods

The large diameters of direct drive machines make the manufacturing of the stator core and coils neither as easy nor inexpensive. In this section, the manufacturability of the stator cores and coils with non-overlap concentrated winding is investigated. This is due to the sizes of the direct drive generators that influence the cost and labour.

3.3.1 Stator cores

The stator core can be punched as a whole or segments as shown in Figure 3.2. For laminations with large diameters, segmented core is a preferred choice as a full segment can be difficult to work with. The segmented cores have the advantages of conventional manufacturing methods. The main drawback is the large waste of core materials (but better than a complete core) leading to an increased cost of the cores. The other option is to have the laminations laser-cut. However this method is expensive and takes a longer time for production. Other methods in literature include join lapped cores and spiral laminated cores. These methods though they have low waste of the iron material, they require special manufacturing techniques and production machines.

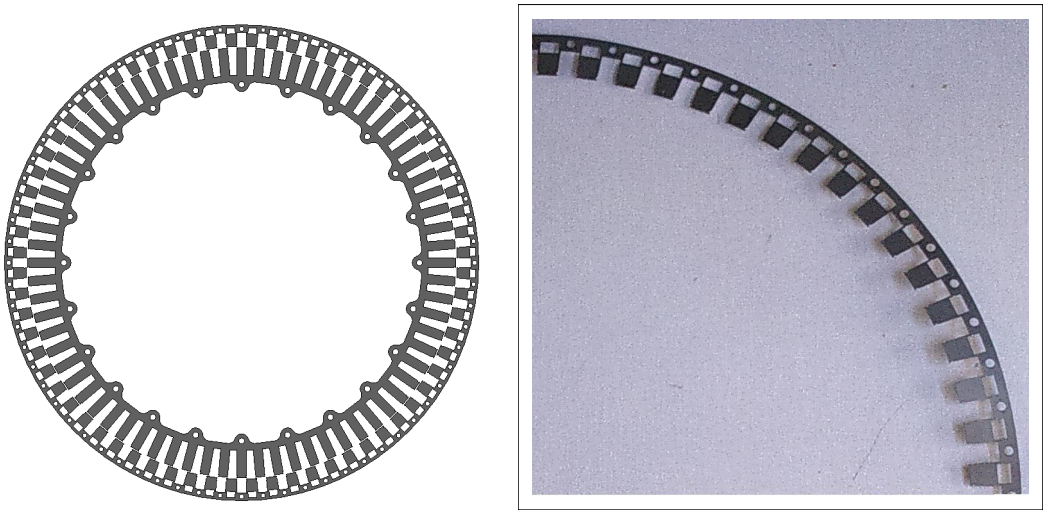

(a) Full lamination. **(b)** Quarter segment of a core lamination.

Figure 3.2: Stator core lamination a) full, and b) a segment.

3.3.2 Stator coils

A complete or segmented laminated core can be wound by a special winding machine or manually done, or pre-formed coils placed in the slots. The use of a special machine that is an automated conventional procedure results in a low fill-factor. Manually wound coils can achieve high fill factors and is also a conventional method. However, this method is slow and with high production cost.

The third method is the use pre-formed coils, which can achieve high fill factor with the right stator core. For the non-overlap winding topology, shorter end windings are resultant from these coils. The other merit of these coil types is that they are easy to fix into the stator slots. The main drawback is fitting the coils in semi-closed slots or designs with deep slanted teeth which is challenging.

3.4 Conclusion

The choice of a 68/72 pole/slot combination results in a design with high a winding factor, mitigates the cogging torque in the generator, low harmonics and posses a balanced magnetic pull from the four machine sections. An open slot topology achieves a high filling factor and can make use of pre-formed coils with N-OCW. Production of the stator cores in segments reduces the cost, eases the labour and manufacturability.

Chapter 4

Analytical Calculation of Variable Flux SGs

In this chapter, an analytical design model is developed for a grid compliant variable-flux synchronous generator (VFSG). A comprehensive derivation of the analytical model shows the step by step design procedure of the wind generator taking into consideration the total magneto-motive force (MMF) required. For a variable-flux SG that consists of two magneto-motive force (MMF) sources (PMs and rotor field coils), the choice of the amount each source can contribute to the total MMF required, termed as the hybrid ratio [9,25] is critical in the design process. Therefore, the need for fast and flexible methods is crucial in an iterative design procedure. Analytical methods offer models that predict the machine behaviour and are computationally efficient [9,46–48]. With an analytical procedure or tool a larger design space can be considered. An analytical procedure to calculate the structural mass of the PM machines in the terms of the inner and outer diameters, axial length and peak value of air-gap flux density is presented in [17]. In this proposed method, the concept of total magneto-motive force (MMF) required by a generator is used. Then equations on torque, power, copper and core losses, current densities and maximum flux densities in the air-gap or the cores are used to size the generator. For simplicity, the air-gap flux density and the air-gap diameter which is the main dimension are taken as constants. In addition, the steel has a linear characteristic in the calculations.

4.1 Design specifications and material characteristics

The specifications requirement for the generators are listed in Table 4.1. They are derived from grid-code requirements and previous prototype generator data. From the given specifications computationally efficient models that accurately capture the relationship between design objectives and inputs are used to develop a VFSG analytical model with high accuracy in generator design for grid compliance, performance analysis and quick comparison of

Table 4.1: Design specifications and material characteristics for Variable-flux synchronous generator (VFSG)

Rated Power	13 kW
Rated torque	1300 Nm
Voltage	400 V L-L
Rated frequency	50 Hz
Phases	3
Rated speed	88 rpm
Air-gap diameter	0.620 m
Air-gap size	2 mm
Stack length	0.1-0.2 m
Stator current density, maximum	4 A/mm^2
Rotor current density	6 A/mm^2
Copper fill factor	0.5
Core maximum flux density, teeth/yoke	1.8/1.5 T peak
Core loss coefficient	0.37 $W/m^3/Hz^2$
Hysterisis loss coefficient	256 $W/m^3/Hz$
Copper resistivity	$20n\Omega m$ @ 75^0C
Remnant flux density	1.2 T
Magnet resistivity	1.4 $\mu\Omega$
Magnet mass density	7500 kg/m^3
Copper mass density	8950 kg/m^3
Steel mass density	7880 kg/m^3

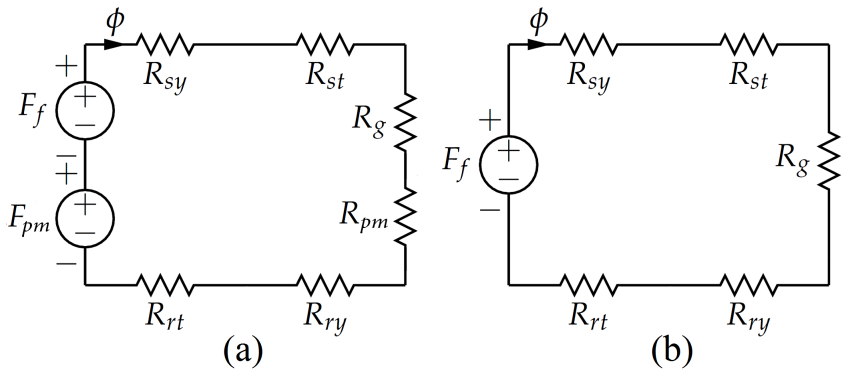

Figure 4.1: Simplified magnetic equivalent circuit for (a) PM VFSG, and (b) non-PM VFSG.

varied design models. There are three design models to be analysed:

1. Surface-PM VFSG: This design model has a conventional PM placed on the rotor tooth surface. It has the simplicity of a series magnetic equivalent circuit analysis as shown in Figure 4.1.a where the MMF from both sources pass through the PMs. Due to the PMs having a relative permeability almost equal to that of air, the effective air-gap size is increased as in (4.3)

2. Buried-PM VFSG: In this design model it is assumed that the MMF from the field coils does not have to go through the PMs. Therefore the magnetic circuit does not entirely have the two MMF sources connected in series. The reduced effective air-gap leads to a lower copper mass in the surface-PM VFSG.

3. Non-PM VFSG: In this design all the MMF is supplied by the rotor field coils as shown in Figure 4.1.b.

4.2 Design equations

4.2.1 Surface-PM VFSG design

The permanent magnet NdFeB-48H type, is chosen due to the high remanent flux density B_r=1.4 Tesla characteristic. The air-gap flux density is then expressed as

$$B_g = \frac{B_r}{1 + \frac{g}{h_{pm}}}. \tag{4.1}$$

With a peak air-gap flux density (B_g) of 0.8 T, and an air-gap size (g), the height of the magnet is calculated from (4.2) as

$$h_{pm} = \frac{g}{\frac{B_r}{B_g} - 1}, \tag{4.2}$$

such that the effective air-gap size is

$$g_{eff} = g + h_{pm}. \tag{4.3}$$

For a 3-phase design, one of the machine's design requirement is that it can achieve three times the maximum current, therefore the ampere-turns per phase per pole-pair are taken to be three times. The resultant magneto-motive force (MMF) required is calculated as

$$F_{rated-pp} = \frac{2}{3}\frac{B_g}{\mu_0}(g_{eff}) = (NI)_{pp} \tag{4.4}$$

The rated torque can be expressed from the output power and rated speed that are given in the specifications as

$$T_{rat} = \frac{P_{out}}{\omega_m} \tag{4.5}$$

where mechanical speed $\omega_m = \frac{2pi}{60} rad/sec.$ From the torque expression of

$$T_{rat} = 2\pi L_{stk} R_g \sigma_{Ftan} \tag{4.6}$$

and the tangential stress σ_{Ftan} is between 12-21kPa, the R_g is the air-gap radius, the stack length can be calculated as

$$L_{stk} = \frac{T_{rat}}{2\pi \sigma_{Ftan} R_g^2}. \tag{4.7}$$

The electric loading is given by

$$A_{load} = \frac{2mF_{rated-ph}}{3\pi D_g} \tag{4.8}$$

where m is the number of phases, and $F_{rated-ph} = pF_{rated-pp}$. The magnetic loading is

$$B_{g,av} = \frac{B_g}{\sqrt{2}} \tag{4.9}$$

The total ampere turns in a phase ($N_{s,ph}I_s$) produced by the rated MMF, with $N_{s,ph}$- being the total number of turns per phase in the stator, and I_s - the rms stator phase current, is

$$N_{s,ph}I_s = \frac{3\sqrt{2}\sigma_{Ftan} D_g}{mB_{g,av}}. \tag{4.10}$$

The number of pole pairs (p) required to produce the required ampere-turns per phase can be calculated from (4.4) and (4.10). Therefore the number of pole-pairs (p) that can produce the required MMF in a circuit is then equal to

$$p = \frac{F_{rated-ph} = N_{s,ph}I_s}{F_{rated-pp}}. \tag{4.11}$$

The tangential stress depends on the electric loading and magnetic loading as

$$\sigma_{Ftan} = \frac{\pi}{2} k_w A_{load} B_{g,av} \tag{4.12}$$

The frequency, f_s, is determined from the specifications as 50 Hz, from this the angular velocity can be expressed as

$$\omega_{el} = 2\pi f_s \tag{4.13}$$

and mechanical as

$$\omega_m = \frac{\omega_{el}}{p}. \tag{4.14}$$

4.2.1.1 Magnetic flux evaluation

The pole pitch is calculated as

$$\tau_p = \frac{\pi D_g}{2p}. \tag{4.15}$$

Taking the magnet span $\tau_{m,sp} = 0.8\tau_p$, the permanent magnet will produce a flux per pole equivalent to

$$\phi_{pm,pp} = B_g \tau_{m,sp} L_{stk}. \tag{4.16}$$

The flux per pole due to the armature field winding is

$$\phi_{arm,pp} = \frac{\mu_0 F_{rated,pp}}{2g_{eff}} \tau_p L_{stk}. \tag{4.17}$$

The rotor field coils supply a variation to the flux supplied by the PMs by a factor K_{rfc}. For grid compliance this factor is equal to 0.1 so that the voltage is increased by 10%. The flux per pole due to the rotor field winding is then

$$\phi_{rfc,pp} = K_{rfc} \phi_{pm,pp}. \tag{4.18}$$

Taking a maximum flux density of $B_{t,max} = 1.8\,T$ and $B_{y,max} = 1.3\,T$, in the core teeth and yokes respectively, then the stator tooth width (b_{st}) is

$$b_{st} = \frac{\phi_{pm,pp} + \phi_{arm,pp}}{m B_{t,max} L_{stk}}. \tag{4.19}$$

The stator slot width is then

$$b_{ss} = \tau_p - b_{st}. \tag{4.20}$$

From specifications $J_s = 4\,A/mm^2$ and the slot fill factor $K_{ff} = 0.5$, the slot area required to conduct the necessary ampere-turns or current is calculated as

$$(NI)_{pp} = J_s K_{ff} A_{ss}, \tag{4.21}$$

where $A_{ss} = h_{ss} b_{ss}$. This low current density value is chosen to reduce temperature effects from the coils as cooling is from circulating air. Thus, the stator slot height is

$$h_{ss} = \frac{(NI)_{pp}}{\sqrt{2} J_s K_{ff} b_{ss}}. \tag{4.22}$$

As open slots are used, and assuming a wedge clearance height (equal to the pole-shoe height for the semi-closed slots) $h_{pls} = 2\,mm$, then the pole shoe width $b_{pls} = b_{st}$. For other design considerations the $b_{pls} = \tau_{m,sp}$. The flux density in the pole shoe is

$$B_{pls} = \frac{\phi_{pm,pp} + \phi_{arm,pp}}{b_{pls} L_{stk}}. \tag{4.23}$$

The flux density in the yokes can have a maximum value of 1.5 T,

$$h_{sy} = h_{ry} = \frac{\phi_{pm,pp} + \phi_{arm,pp}}{B_{y,max} L_{stk}}. \tag{4.24}$$

The rotor tooth width is calculated as

$$b_{rt} = \frac{\phi_{pm,pp} + \phi_{arm,pp}}{B_{t,max} L_{stk}}, \tag{4.25}$$

and the slot width height as

$$b_{rs} = \tau_p - b_{rt}. \tag{4.26}$$

The rotor slot height is then

$$h_{rs} = \frac{(NI)_{rot,pp}}{\sqrt{2} J_r K_{ff} b_{rs}} \tag{4.27}$$

where $J_r-$is the current density in the rotor field coils, and the rotor ampere-turns$(NI)_{rot,pp}$, to increase the total flux produced from the PMs by 10 % is

$$(NI)_{rot,pp} = \frac{0.2 \phi_{pm,pp} g_{eff}}{\mu_0 \tau_p L_{stk}}. \tag{4.28}$$

The rotor and stator tooth heights are calculated respectively as

$$h_{rt} = h_{rs} + h_{pls} \tag{4.29}$$

and

$$h_{st} = h_{ss} + h_{pls} \tag{4.30}$$

The outer diameter is twice the outer radius $D_{out} = 2R_{out}$, with R_{out} being

$$R_{out} = R_g + g + h_{pm} + h_{rt} + h_{rs}, \tag{4.31}$$

and the inner diameter $D_{in} = 2R_{in}$ where

$$R_{in} = R_g - h_{st} - h_{sy}. \tag{4.32}$$

4.2.1.2 Mass and volume calculation

The total active volume considering a lamination stack factor of 0.95

$$V_{act} = \pi(R_{out}^2 - R_{in}^2)\frac{L_{stk}}{0.95}. \tag{4.33}$$

The stator coil area is defined as

$$A_{sc} = 0.5 h_{ss} b_{ss}, \tag{4.34}$$

whereas the length of the copper wire per phase is

$$l_{sc} = 2(\frac{L_{stk}}{0.95} + \frac{\pi}{2}\tau_p)\frac{Q_s}{3}, \tag{4.35}$$

giving a total volume of stator armature winding of

$$V_{s,arm} = 3 A_{sc} l_{sc}. \tag{4.36}$$

Consequently the rotor coil area is defined as

$$A_{rfc} = 0.5 h_{rs} b_{rs}, \tag{4.37}$$

whereas the length of the rotor copper wire is

$$l_{rfc} = 4p(\frac{L_{stk}}{0.95} + \frac{\pi}{2}\tau_p), \tag{4.38}$$

and the total rotor copper volume is

$$V_{rfc} = A_{rfc} l_{rfc}. \tag{4.39}$$

The mass of the copper windings is then calculated as

$$M_{Cu} = M_{Cu,r} + M_{Cu,s}\,, \tag{4.40}$$

where individual masses of the stator and rotor windings are

$$M_{Cu,s} = 8950 V_{s,arm}, \quad and\ M_{Cu,r} = 8950 V_{rfc}. \tag{4.41}$$

The volume of PMs required is

$$V_{pm} = 2p\tau_{m,sp} h_{pm} L_{stk} \tag{4.42}$$

and the total PM mass is calculated as

$$M_{pm} = 7500 V_{pm}. \tag{4.43}$$

The approximate core volume for a pole-pair is calculated as

$$V_{core,pp} = L_{stk}[2h_{pls}b_{pls} + 2h_{ss}b_{ss} + 2h_{rs}b_{rs} + 2\tau_p(h_{sy} + h_{ry})] \tag{4.44}$$

and the total core volume as

$$V_{core} = pV_{core,pp}\,. \tag{4.45}$$

The total core mass is then

$$M_{core} = 7880V_{core}\,. \tag{4.46}$$

The total machine mass is

$$M_{tot} = M_{Cu} + M_{pm} + M_{core}\,. \tag{4.47}$$

4.2.1.3 Iron loss calculation

Iron loss is estimated using the general loss equation in W/kg as

$$P_{Fe} = C_{hyst}fB_{max}^2 + C_{edy}f^2B_{max}^2, \tag{4.48}$$

which is dependent on the frequency, f, and maximum flux density, B_{max}, in the iron cores. C_{hyst} and C_{edy} are the loss coefficients of the hysteresis and eddy current that are found in the steel manufacturer catalogue. The total core loss is then calculated as [

$$P_{core} = C_{ChCe}pL_{stk}[2B_{pls}^2h_{pls}b_{pls} + 2B_{t,max}^2(h_{ss}b_{ss} + h_{rs}b_{rs}) + 2B_{y,max}^2\tau_p(h_{sy} + h_{ry})] \tag{4.49}$$

where $C_{ChCe} = C_{hyst}f + C_{edy}f^2$ is a constant calculated from the loss coefficients and the frequency.

4.2.1.4 Copper loss calculation

The copper loss is calculated with an estimation without considering the influence of skin effect by

$$P_{Cu} = p(I_{ph}^2R_{s,pp} + I_{r,pp}^2R_{r,pp}), \tag{4.50}$$

where stator resistance per pole-pair is given by

$$R_{s,pp} = \rho_{Cu}\frac{\frac{3}{Q_s}l_{sc}}{A_{sc}} \tag{4.51}$$

and the rotor resistance per pole-pair is given by

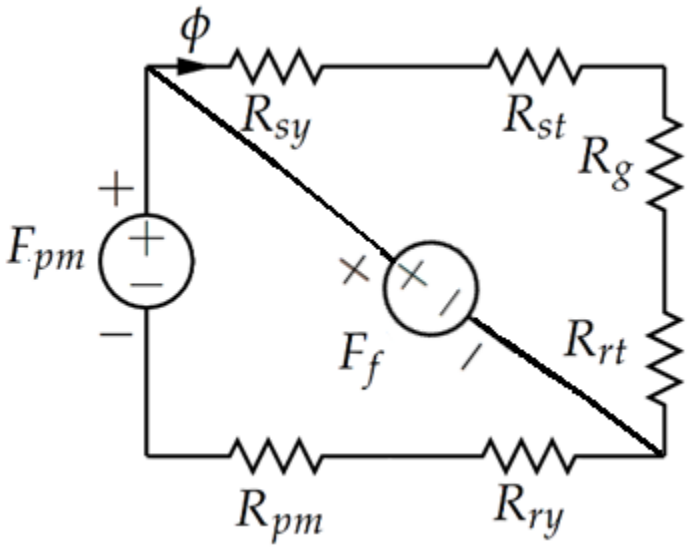

Figure 4.2: Simplified magnetic circuit for buried-PM VFSG.

$$R_{r,pp} = \rho_{Cu} \frac{\frac{l_{rfc}}{p}}{A_{rfc}}. \tag{4.52}$$

The efficiency of the generator is then found by

$$\eta = \frac{P_{out}}{P_{out} + P_{Cu} + P_{core}}. \tag{4.53}$$

4.2.2 Buried-PM VFSG design

As the requirements of this topology is the same as the same of those of the previous model with surface mounted PMs, the output power, rated synchronous speed, torque, core flux densities, magnetic and electric loading are same. The air-gap diameter is also constant. However, the magnetic circuit changes to Figure 4.2. This is on the assumption that the MMF from the flux will go through the rotor teeth, air-gap and stator teeth and yoke than go through the PMs (with $\mu_{pm} \approx \mu_0$).

The stator armature coils now has a flux linkage equal to

$$\phi_{arm,ppII} = \frac{\mu_0 F_{rated,pp}}{2g} \tau_p L_{stk}. \tag{4.54}$$

As the stator dimensions are taken as a constant, the analysis is the same as that of buried-PM VFSG above. The only difference is the amount of rotor-field coils MMF supplied, which is

$$(NI)_{rot,ppII} = \frac{0.2\phi_{pm,pp} g}{\mu_0 \tau_p L_{stk}}, \tag{4.55}$$

and the new rotor slot height is

$$h_{rs,II} = \frac{(NI)_{rot,ppII}}{\sqrt{2}J_r K_{ff} b_{rs}}. \tag{4.56}$$

What will change in the generator dimension is the rotor field coils which influences the outer radius which is then

$$R_{out,II} = R_g + h_{pls} + h_{rs,II} + h_{ry}\,. \tag{4.57}$$

4.2.3 Non-PM VFSG design

This is the conventional synchronous generator that is electrically excited, refered to as EESG. This generators types do not have permanent magnets to supply the MMF requirement hence termed in this work as a non-PM VFSG. This model has an air-gap size that is equal to the chosen air-gap value. It is taken that the slot is semi-closed with a pole shoe Hence a high flux density can be achieved. The total MMF required is reduced when compared to the MMF required for the PM VFSG topologies. This is due to the reduced effective air-gap size and no PMs' reluctance.

For a given air-gap size, the procedure as for the surface-PMs is followed. For an equivalent power rating and an equal air-gap flux density, the dimensioning is done. The stator slot height is then

$$h_{ss,III} = \frac{(NI)_{pp,III}}{\sqrt{2}J_s K_{ff} b_{ss}} \tag{4.58}$$

where

$$(NI)_{pp,III} = \frac{2\phi_{pp,III} g}{\mu_0 \tau_p L_{stk}}\,. \tag{4.59}$$

The rotor slot height is

$$(NI)_{rot,ppIII} = \frac{2.2\phi_{pp,III} g}{\mu_0 \tau_p L_{stk}}\,, \tag{4.60}$$

and the new rotor slot height is

$$h_{rs,III} = \frac{(NI)_{rot,ppIII}}{\sqrt{2}J_r K_{ff} b_{rs}}\,. \tag{4.61}$$

The generator's outer diameter then becomes

$$R_{out,III} = R_g + h_{pls} + h_{rs,III} + h_{ry}. \tag{4.62}$$

Table 4.2: Comparison of the three VFSG topologies using the analytical method.

	Initial-PM SG	Surface-PM VFSG	Buried-PM VFSG	EESG
Mass rotor [pu]	1	1.49	1.08	1.97
Mass PM [pu]	0.167	0.208	0.262	0
Efficiency [%]	96.4	94.8	95.5	87.2

4.3 Mass comparison of the three designs

The rotor mass of the non-PM VFSG (EESG) is almost double that of the initial PMSG and the efficiency is reduced by almost 10 % as given in Table 4.2. There is a minimum reduction of 1.6 % in the efficiency of the buried-PM VFSGs. As the PM height is increased, the amount of MMF required varies as shown in Figure 4.3, where the topology with a PM height $h_{pm} = 0$ is the non-PM VFSG and the chosen topology with $h_{pm} = 8$ mm is the surface-PM VFSG. During normal operation, the MMF is supplied by the PMs only. Depending on the direction of the rotor field current, boosting or weakening operation is achieved. Therefore the PM VFSG topologies with nominal MMF from the the PMs are a suitable choice for the grid-compliant wind turbine system.

A copper factor - α_{Cu} defined in (4.63), is dependent on the maximum air-gap flux density as well as the air-gap size as shown in 4.4.

$$\alpha_{Cu} = \frac{F_{max(PMVFSG)}}{F_{max(Non-PMVFSG)}}. \tag{4.63}$$

This is the ratio of the amount of copper necessary for the flux variation capability to be achieved in the PM VFSG to the non-PM VFSG designs. The MMF used in both designs is the maximum amount needed for flux boosting or strengthening. An increase in the air-gap results in an exponential decrease in α_{Cu} value as represented in Figure 4.4. This implies that for large machines, PM VFSG designs are favourable as they achieve a better copper factor.

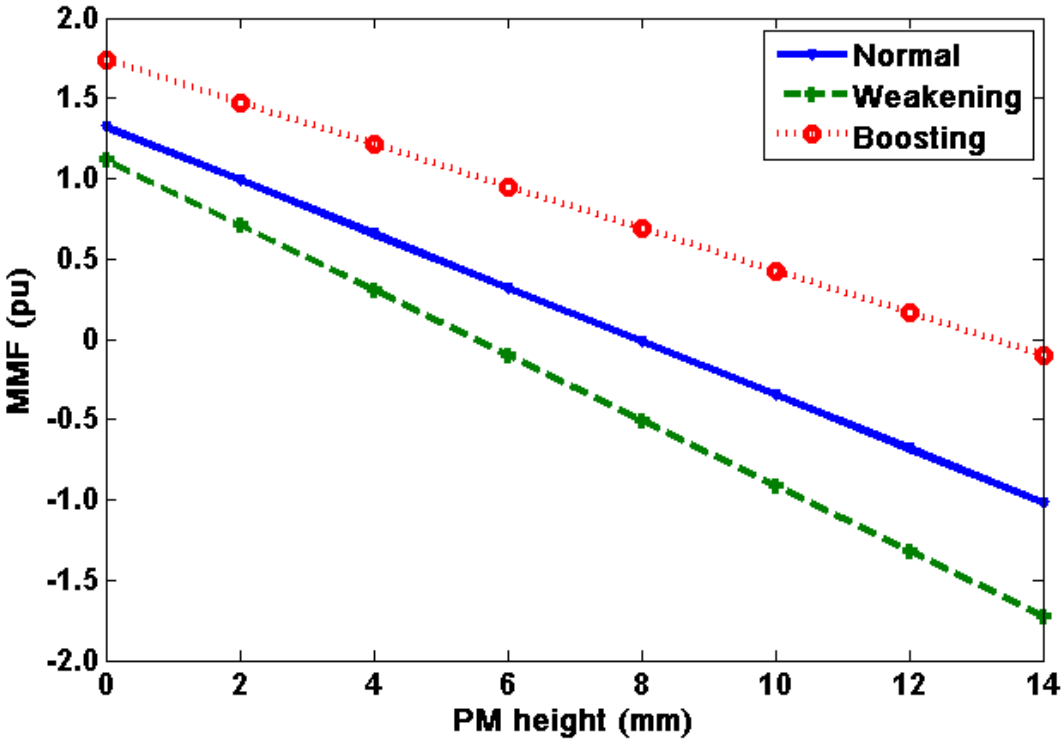

Figure 4.3: MMF versus PM height.

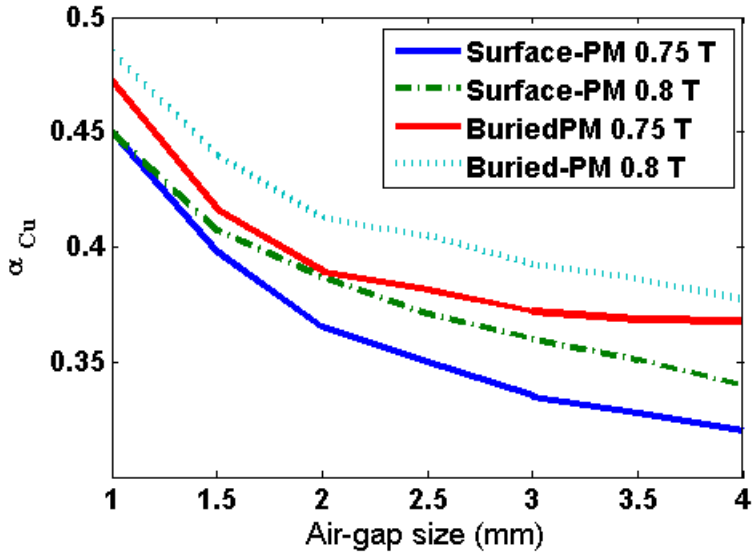

Figure 4.4: Copper mass ratio (α_{Cu}) versus air-gap size.

4.4 Conclusion

In this chapter, analytical expressions and design aspects of variable flux synchronous generators with different topologies and three-phase stator winding were investigated for a grid-compliant wind turbine system. Using the analytical model, the generator topologies were compared in terms of rotor mass and overall efficiency. From the analysis it is possible to make a choice of the preferred PM VFSG topology to be used. The analytical model/expression showed very good performance when evaluated with varied air-gap sizes, maximum air-gap flux density and so on. This is advantageous to the generator design procedure as numerical modelling allows a lot more flexibility than prototype testing does.

From the analytical design, a defined copper mass factor shows that the buried PM VFSG topology with a 2 mm air-gap, achieves 39 % low amount of copper to achieve 10 % flux variation for grid compliance,

Therefore, in particular, the significance of this chapter is the possibility of reproducing an actual grid-compliant generator design with clarity and comparative accuracy, when compared to the FEM analysis which is discussed in the next chapter.

Chapter 5

FEM modelling and rotor design analysis

In this Chapter PM VFSG topologies are analysed. The selected PM VFSG topologies consist of two MMF sources both placed in the rotor cores combining the merits of PMs and rotor-field-coils.

From the turbine of a 15 kW, surface magnet mounted, permanent magnet synchronous generator (PMSG) that was built and tested in the EMLab of Stellenbosch University, together with the results of the analytical analysis from the previous chapter, a surface-PM design model is chosen as a benchmark surface-PM VFSG for this dissertation study. In this chapter the analysis of the rotor design to validate the proposed models and design procedure is described. The proposed PM VFSG models are then used to analyse the rotor designs with identical stator constraints for the initial directly grid-connected PMSG. Two topologies discussed in the previous chapter as well as two other rotor design topologies are compared and analysed in terms of their generator geometry, MMF excitation sources, stator back-EMF per phase, developed electromagnetic torque (T_{em}) for both no-load and rated-load conditions, as well as the rotor voltage source. Conclusions are presented on the four approximate models, and two generator design outputs are afterwards adopted for a design optimisation procedure carried out.

5.1 Magnetic Field Problems Computation

There are a number of tools that have been developed over the years to study and approximate electrical machine behaviour in linear and non-linear modes. In this chapter, a synchronous generator with two MMF sources in a rotating rotor is analysed by utilising the finite element method [49] in MagNet solver from Infolytica. MagNet is a commercial software tool that can solve several low frequency electrostatic and electromagnetic problems in $2-D$ as well as in $3-D$. In this study, the four generator geometries are analysed using

their equivalent $2-D$ FE models. MagNet is used to analyse the proposed generator rotor construction, with regard to variation in geometry specification, MMF sources, rotor field current supplied, number of turns in the rotor etc., to obtain the adequate variables which satisfy the desired mode of operation with regard to grid-compliance.

Magnetic fields are present around current carrying conductors and also exist around magnetised objects such as permanent magnet material. The magnetic circuit quantities are represented by magnetic flux, reluctance, and magneto-motive force. These magnetic quantities can be thought of as analogous to electrical circuit quantities, such that the electrical circuit analysis rules are applicable to magnetic circuits [10, 50–52].

Magneto-static problems are problems in which the fields are time-invariant [52]. In this case, the field intensity (H), flux density (B), and current density (J) must obey (5.1) and (5.2)

$$J = \nabla H \tag{5.1}$$

$$\nabla B = 0 \tag{5.2}$$

subject to a constitutive relationship between B and H for each material [49]

$$B = \mu H \tag{5.3}$$

If the material is non-linear (saturating iron or permanent magnet material), the permeability, μ, is a function of B as in (5.4) [49]

$$\mu = \frac{B}{H(B)} \tag{5.4}$$

The MagNet solver converges such that (2.1) to (2.3) are satisfied via a magnetic vector potential approach. Flux density is expressed in terms of the vector potential, Av, as in (5.5)

$$B = \Delta A_v, \tag{5.5}$$

$$J = \Delta B(\frac{1}{\mu(B)}) \tag{5.6}$$

$$J = (\frac{1}{\mu})\Delta^2 A_v \tag{5.7}$$

This definition of B always satisfies (5.2). Then, (5.1) can be rewritten as 5.7. For a linear isotropic material and assuming the Coulomb gauge, ($\Delta.Av = 0$), (5.6) reduces to 5.7, then FE retains the form of (5.6) so that magneto-static problems in a non-linear $B-H$ relationship can be solved.

The advantage of using the vector potential formulation is that all the conditions to be satisfied have been combined into a single equation. If A_v is found, B and H can then be deduced by differentiating A_v. Hence, the FE solver technique is based on the division of the volume or domain in which this equation is valid into smaller volumes or domains or so-called finite elements. Within each element a simple polynomial is used to approximate the solution via iterative methods which in MagNet are conjugate-gradient, and Newton-Raphson methods.

The procedure for numerical computation of magnetic field problems using MagNet is divided into three steps, pre-processor, processing, and post-processing. In pre-processor mode, the generator outline is drawn in the MagNet solver. The material properties are defined, boundary conditions assigned and mesh generation is done. In the Processing mode, the Maxwell's equations are used in problem solution and in obtaining the field distribution in the analysed domain of the generator. In post-processing mode, the calculations of characteristics, and the obtaining of the necessary generator parameters are done.

5.2 Choice of generator topology

In this section, the generator topologies that will be analysed are discussed and their advantages mentioned. All the generator topologies have an outer rotor and the flux in radial direction due to the merits discussed in previous chapter, specifically for a direct-drive directly grid-connected generator. The outer rotor has the advantage of easir connection with the slip-IG component and the wind turbine. Moreover, the outer rotor results in reduced outer diameter and hence generators volume.

5.2.1 PM-VFSG Generator concept

The choice of radial-flux design is due to the simplicity of the overall design structure, and a small air-gap size is achievable, leading to better active material utilisation.

The stator core is open-slotted for winding. These open slots permits the use of preformed coil which leads to easier manufacturing procedure. This also leads to reduced mass of the PMs to be used when compared to a non-slotted (air-gap winding) topology. The slots are wide and shallow to allow a better fill factor. The winding type is a non-overlap concentrated winding with a double layer. A three phase winding is adopted (to fit the direct grid-connection) and two adjacent phases share the last/first slot in a group coil. The base winding is 34-poles 36-slots with a winding factor of 0.953.

The outer rotor allows for direct connection with the rotor of the slip-IG unit and subsequently direct connection to the turbines. Double excitation in the rotor is used due to the fact that the PMs give high efficiency and reduced mass, and allow the use of small pole pitches (desirable in high pole/slot numbers) that lead to reduced end winding. The rotor field excitation (copper) on the other hand, allows the generator to achieve variable flux

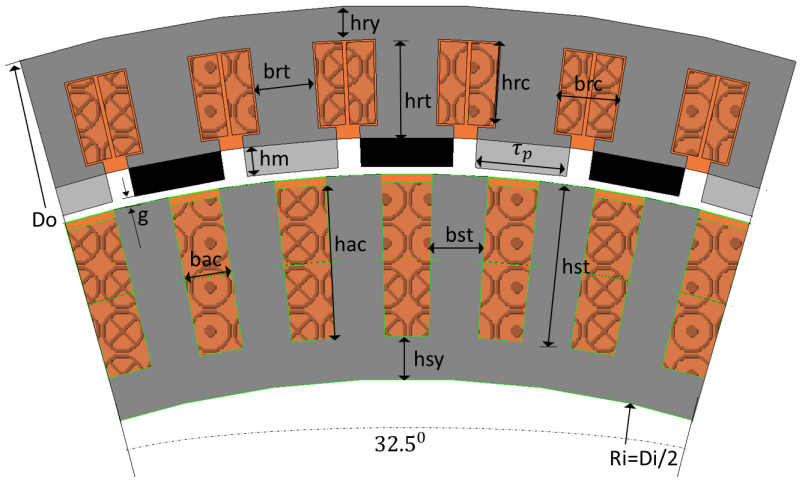

Figure 5.1: Cross-section of a surface-PM VFSG with an outer rotor.

Table 5.1: Surface-PM initial generator parameters as shown in Figure 5.1.

Parameter	D_i	g	τ_{pm}	h_m	h_{st}	h_{sy}	h_{rt}	h_{ry}	τ_S
Value	650	2	21.5-28.7	6	42	13	18	6.5	17.6

capabilities, that are crucial to direct grid connection. The MMF from the PMs therefore produce a nominal constant flux linkage in the stator coils, whereas the MMF from the copper excitation produces flux that is dependent on the amount and direction of the current supplied to the rotor field coils. The magnets are placed on the rotor surface termed as surface-PM VFSGs or buried in the rotor cores called buried-PM VFSGs. The NdFeB type of PMs chosen for this generator topology leads to light weight, but has the disadvantage of costs when compared to other magnet types like those made from ferrites. The rotor core is slotted and the field coils filled with the copper on either side of the PMs as shown in Figure 5.1.

The initial surface-PM VFSG is illustrated in Figure 5.1, showing the stator and rotor with surface mounted PMs and coils on either side. The main dimensions of the generator

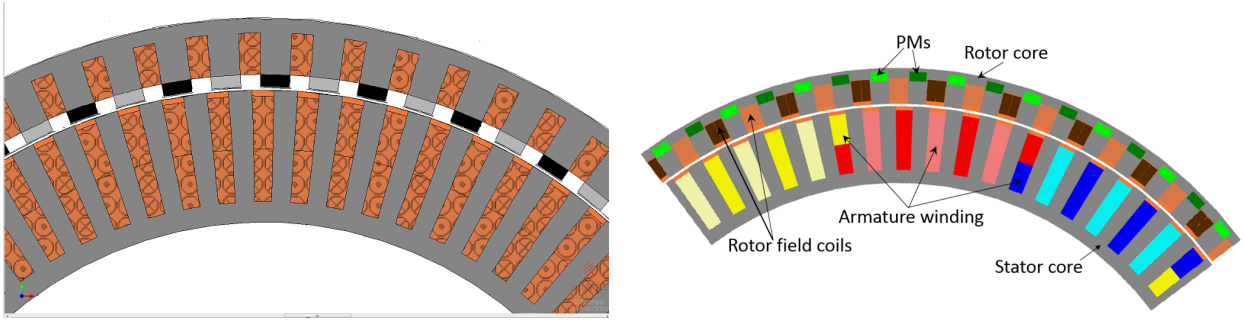

(a) Surface-PM (design II) **(b)** Buried-PM (design III)

Figure 5.2: Cross-section of open slots VFSG with N-OCW and outer rotor topology.

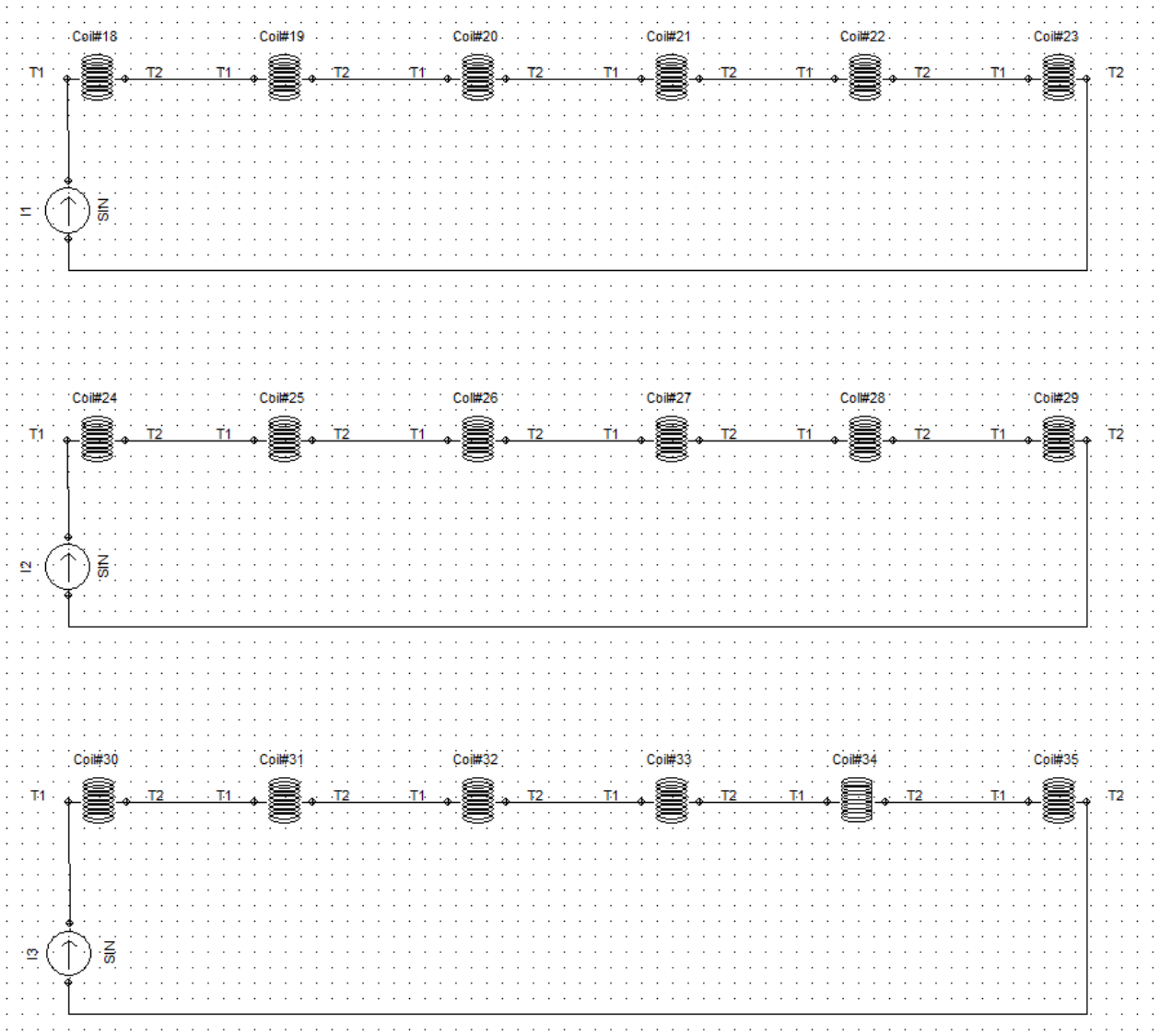

Figure 5.3: Stator winding topolgy for the three phases (quarter generator) in MagNet.

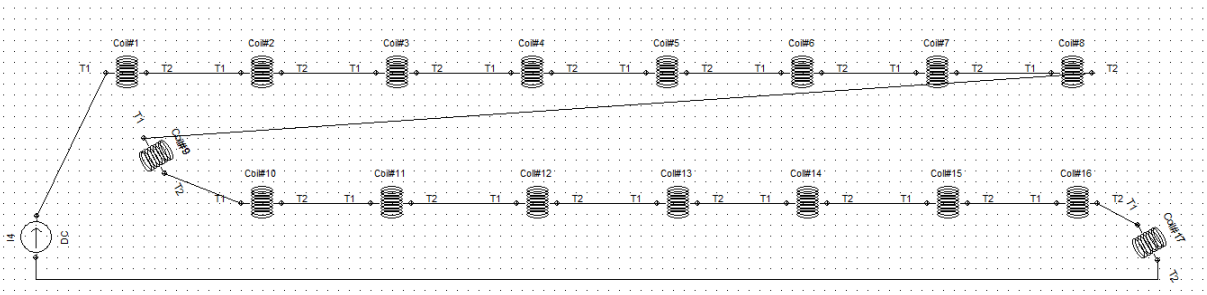

Figure 5.4: Winding topology of the rotor coils all in series in MagNet..

parameter values as defined in the figure are also given in Table 5.1. Figure 5.3 illustrates the stator coil-connections in MagNet solver, for a section of all the generator designs being investigated. The 17 rotor coils are connected in series as shown in Figure 5.4.

5.2.2 Materials used in the FEM model

In the FEM model one quarter of the generator has negative generator periodicity. This is the advantage of the chosen pole/slot combination with four sections. Figure 5.5 illustrates the second version of the benchmark surface-PM VFSG with open slots. The $2-D$ model in the figure illustrates the material description in FEM. The definition is the same for all the four generator topologies that were analysed (surface-PM semi-closed slots, surface-PM open slots, buried-PM open-slots and buried-PM open slots but with two parallel rotor coil connections). Material assignment in MagNet is via blocks. Each model part has a specific name, a material assigned from the component library, and for the coils and an associated current together with a circuit showing the connection as shown in Figure 5.3 and Figure 5.4. A PM-VFSG consists of four materials and air that form its components:

1. Air: For all air-gaps inside and around the generator model.
2. US Steel Type M470-50A : For the stator and rotor parts (laminations-0.5mm thickness) of the generator.
3. Permanent magnet: NdFeB-48H: Sintered Neodymium-iron-boron permanent magnet material used for the generator's rotor permanent magnets.
4. Copper 5.77e7 Siemens/metre: Used for the stator phase windings and rotor field coils.
5. Epoxy: NOMEX:-for filling the coil slots.

Having set up the machine problem at the pre-processing stage, the MagNet from Infolytica solves the magnetic field equations and produces results, for example the distribution of magnetic flux in the machine. This can be done after the meshing process which is shown in Figure (5.5b).

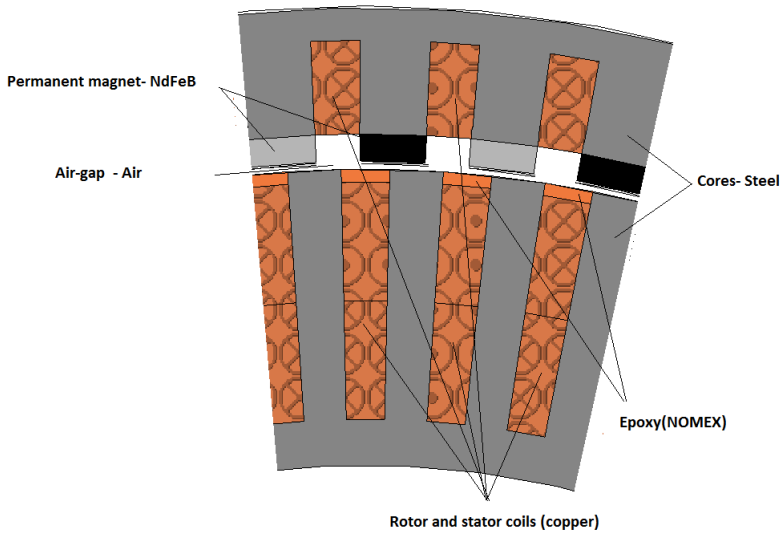

(a) Material description in FEM using MagNet solver for surface-PM open-slots design.

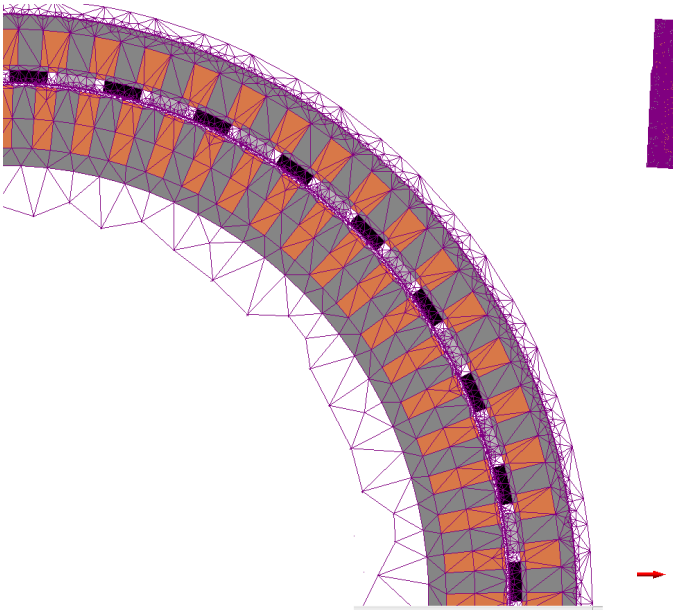

(b) Meshing in surface-PM with coarse meshing especially in the cores.

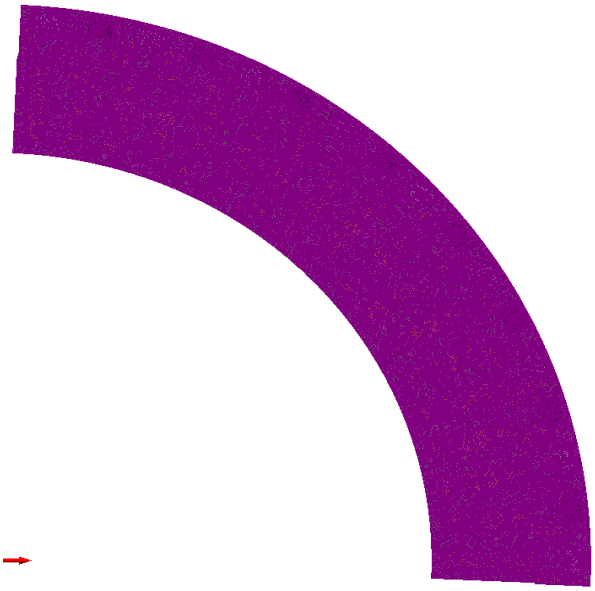

(c) Buried-PM with fine mesh.

Figure 5.5: Model in 2-D FEM. The coarse meshing shown in (b) takes 2 seconds for a static solution to be solved, whereas a fine mesh as shown in (c) takes 300 seconds.

In MagNet scripting languages supporting common object model (COM) such as VB or python can be used to write scripts that automates the sequence of tasks. Typical tasks in the script tasks [49] are:

- (a) Open a desired model in MagNet.
- (b) Apply a 'For-loop' function that is controlled by a specified rotor angular step.
- (c) Solve and analyse the model.
- (d) Save the analysed data in a new file.
- (e) Rotate the desired parts of the machine by angular steps.
- (f) Solve and analyse the new rotated model.
- (g) Loop back to (d) or exit the for loop function when the desired final angle value is reached.
- (h) Stop the analysis.

Post-processing of the solved field solution is then used to carry out further analysis of the generator performance. MagNet solver provides the desired data for either stationary or rotation of magneto-static fields. Thus the generator's characteristic performance can be predicted for different conditions of operation. To consider machine rotation it was necessary to produce multiple field solutions from which the the generator's back-EMF is determined.

5.3 Rotor design Analysis

The stator core and the winding design are the same for the different rotor types to be studied either with surface-PM or buried-PM VFSG topologies. The rotor field coils are equal to the number of PM poles. Three design topologies have the rotor coils in series connection, while the fourth design has parallel connection. The rotor field coils are designed to develop equal stator flux levels at no-load (I_s=0). The steps used to develop the rotor design model are :

- Draw the model in MagNet using preliminary design values of an existing generator model.
- Get the no load stator flux linkage (MMF from PMs only).
- Switch on the current in the rotor field coils to increase the stator flux linkage by 10 %
- Adjust the rotor model with respect to the field coils, to investigate the impact of key rotor magnetic circuit dimensions on overall design.

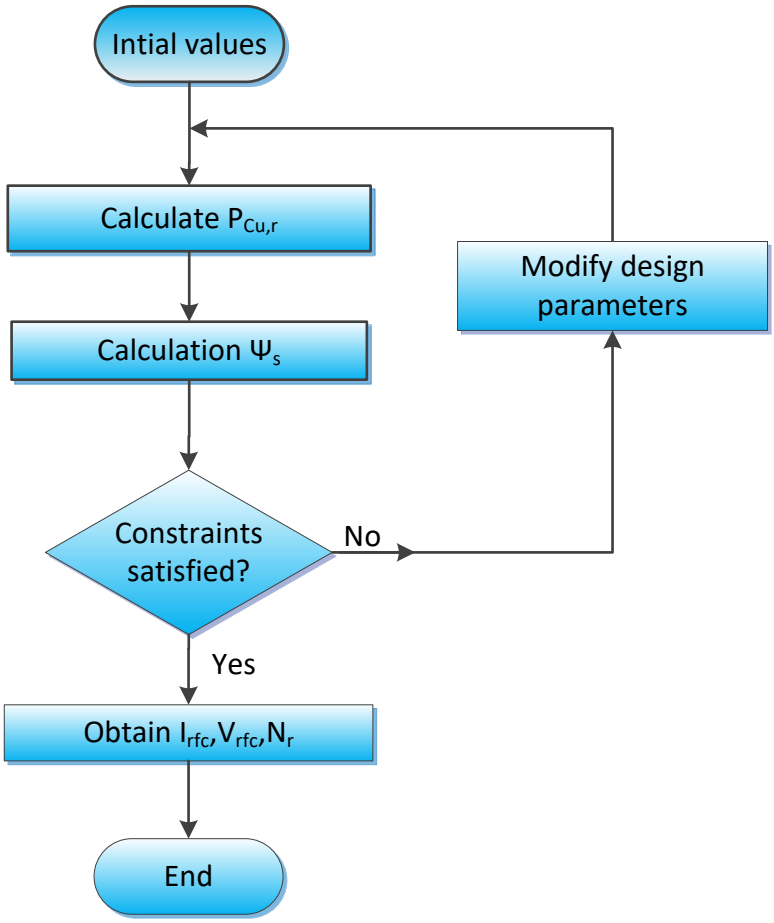

Figure 5.6: Rotor field coil design algorithm.

5.3.1 Finite element analysis for the rotor field coil design

Analysis for the rotor MMF sources to

- Achieve maximum air-gap flux density (B_g) with minimum rotor field current I_{rfc}.
- The rotor copper loss $P_{Cu,r}$ and saturation should be minimal.

The best design will need to develop maximum air-gap flux density with minimum rotor field excitation current (I_{rfc}) and voltage (V_{rfc}) for a given rotor copper loss ($P_{Cu,r}$max =150 W). The equations governing the design procedure are

$$N_r = \frac{J_r A_{rs}}{K_{ff} I_{rfc}}\,, \tag{5.8}$$

$$L_{rfc} = N_r(2L_{stk} + 2\pi L_{r,ew})\,, \tag{5.9}$$

Table 5.2: Condition 1 results with constant rotor curent density J_r =4 A/mm^2

Rotor design	ψ_S	$P_{Cu,r}$
Surface-PM semi-closed slots	0.045	193
Surface-PM open slots	0.045	124
buried-PM open slots	0.083	69.19
buried-PM open slots (parallel rotor coils)	0.0825	66.56

$$R_{rfc} = \frac{pN_r L_{rfc}}{\sigma_{Cu} A_{rs}}\,, \tag{5.10}$$

$$V_{rfc} = I_{rfc} R_{rfc}\,, \tag{5.11}$$

$$P_{rfc} = I_{rfc}^2 R_{rfc}\,, \tag{5.12}$$

where, N_r is the rotor turns, J_r is the rotor current density, A_{rs} is the rotor slot area, I_{rfc} is the current flowing through the rotor field coils, L_{rfc} is length of copper per rotor excitation, coil, σ_{Cu} is the copper conductivity, whereas R_{rfc}, V_{rfc}, and P_{rfc} are the rotor field coils' resistance, voltage and copper loss respectively. $L_{r,ew}$ is the length of the rotor end winding estimated as equal to $\pi\tau_p$.

Figure 5.6 shows the algorithm used to calculate the number of turns and rotor field coil excitation. As defined by equation (5.8) through (5.12), the rotor designs are evaluated under three conditions.

1. Condition 1: Calculating the rotor copper loss and required rotor supply voltage, keeping the rotor current density J_r constant at 4 A/mm^2. The rotor field current (I_{rfc}) together with the rotor coil turns N_r, are varied for the optimum combination to be achieved.

2. Condition 2: A constant number of rotor turns is chosen and I_{rfc} is varied to calculate the stator flux, ψ_S, rotor current density J_r, V_{rfc} and $P_{Cu,r}$.

3. Condition 3: Constant rotor field coils turns N_r is taken and I_{rfc} is varied to calculate the required P_{rfc} and voltage it will produce in the stator with a fixed stator current density $J_s = 6\,A/mm^2$. (For the best design).

The algorithm allows, for each combination of ψ_S, and $P_{Cu,r}$, a selection of I_{rfc}, V_{rfc} and N_r combination which minimises the $P_{Cu,r}$. The rotor designs satisfying the above design criteria are then chosen as suitable candidates.

For a rotor voltage supply of 48 V the rotor field coils N_r equal 46 turns for the different rotor design topologies, however their copper losses are not the same as shown in Table. 5.2. Table 5.2 further shows that the stator flux per coil, is almost doubled when the design

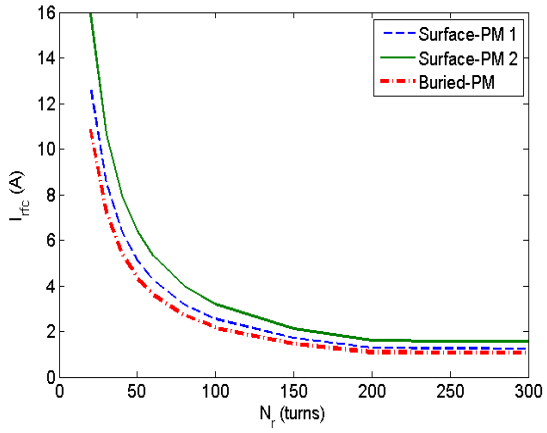

Figure 5.7: Variation of I_{rfc} with increase in rotor turns N_r of the rotor field coils for surface-PM 1 (with semi-closed slots), surface-PM 2 (with open slots), and buried-PM designs.

Table 5.3: Summary of the analysis that satisfies condition 2 for N_r equals 30 turns

Rotor design	I_{rfc}	J_r	V_{rfc}	$P_{Cu,r}$	ψ_S
1	5.4	6.2	48	259.2	0.05
2	4.8	5.8	27.02	131.4	0.05
3	4.5	2.1	10.44	46.96	0.083
4	10	2.3	4.93	49.28	0.084

changes from surface-PM to buried-PM generator type for a constant rotor current density equal to 4 A/mm^2. Each rotor design type, either surface-PMs or buried-PMs, has similar outputs of stator flux linkage irrespective of the slot type or parallel connection of the rotor-field-coils respectively. Overall the buried-PMs design yields the best results in terms of the stator flux linked and the rotor copper loss.

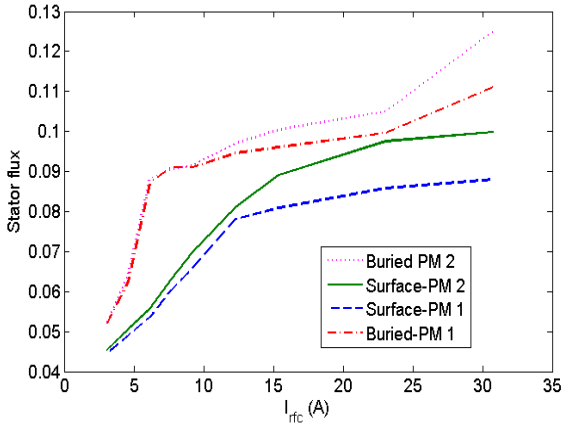

Figure 5.9: Stator flux versus rotor coils current density for four rotor designs.

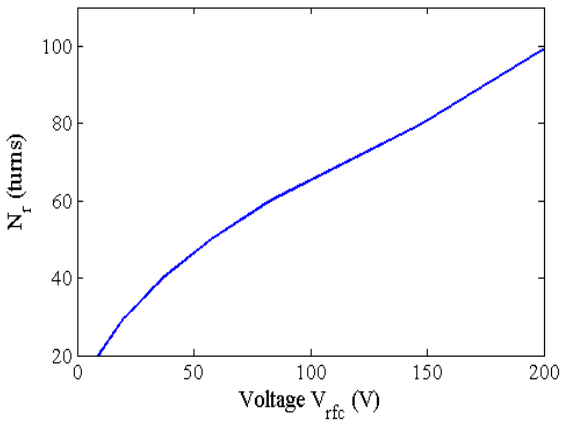

Figure 5.8: Typical representation of N_r versus rotor voltage source for surface-PM.

The results of the study under condition-2 are summarised in Table 5.3 and shown in Figure 5.9. After around 200 turns for all the design topologies studied, an increase in rotor turns does not result in a reduced current as depicted in Figure 5.7. As the losses in the rotor coils are needed to be minimal, the rotor turns in a coil for a series connection will not be more than 80 turns as represented in Figure 5.8.

For a given rotor coil turns, an increase in the rotor current causes an increase in the stator flux as depicted in Figure 5.9. The surface-PMs with semi-closed slots design has a lower gradient in the stator flux increase with low rotor currents, then saturates. The surface-PM open slot design follows with the same gradient but increases the stator flux more when rotor currents are more than 12 A, before starting to saturate. The early saturation in the design with semi-closed slot couls be due to the leakage flux. The buried-PM topologies have a steep gradient in the stator flux with low current levels. There is a saturation region then again a step increase with high rotor currents (greater than 25 A) shown in Figure 5.9.

The buried-PM topology is designed with rotor current less than 10 A for best performance. further increase in the rotor currents does not yield significant results as shown in Figure 5.10. where for rotor current less than 10 A there is a less gradient in the power to current relationship then becomes steep with higher rotor currents. This results implies higher flux leakage, where not linear relationship is achieved in results of Figure 5.10b between the output stator voltage produced to the rotor current supplied.

It is demonstrated that buried-PM VFSG, with open slot and series connection of the rotor field coils, is considered the best design choice of the four rotor MMF designs. The maximum air-gap flux density for all of the PM VFSG designs is around 0.71 T, however the slot current density and copper losses at this air-gap flux density are high for the surface-PM designs.

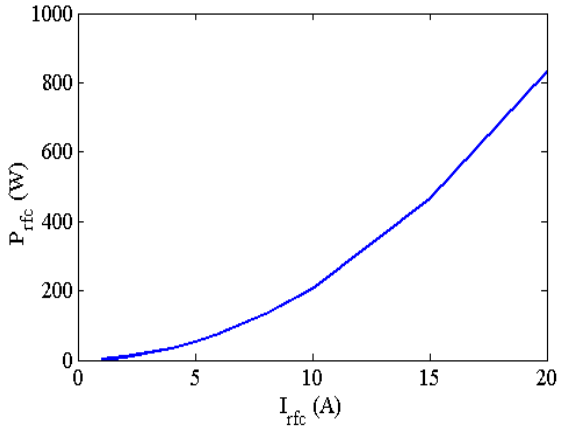

(a) Rotor copper loss versus rotor field current

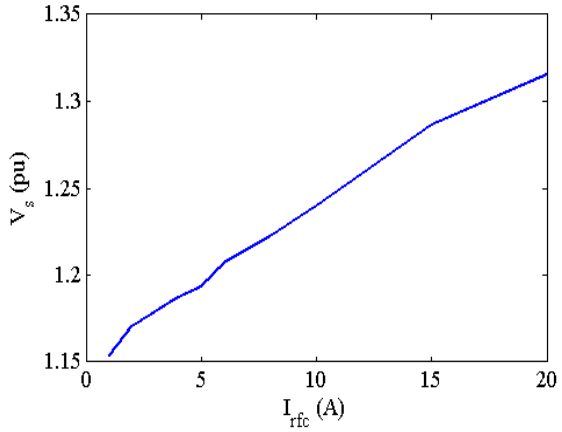

(b) Stator voltage versus rotor fied current

Figure 5.10: The third condition of design analysis for the buried-PM design with 30 turns in the rotor coil, showing influence from the leakage flux.

5.4 Postprocessing

After FEM solutions post-processing is carried out to retrieve quantities such as co-energy, force, torque, flux and flux density. From FE several outputs that are achieved include,

- Force and torque: These are calculated using Maxwell stress. Other methods include Lorentz force and virtual.
- Back EMF: Variation of flux and flux linkage against rotor motion is used to obtain the back EMF.
- Flux plots: These are helpful in estimating the leakage flux and determining the leakage permeance.
- Flux density calculation: Which variation for each generator part can be achieved.

- Permanent magnet working point: The visual effect of demagnetisation is carried out from the B-H working point within each magnet element.

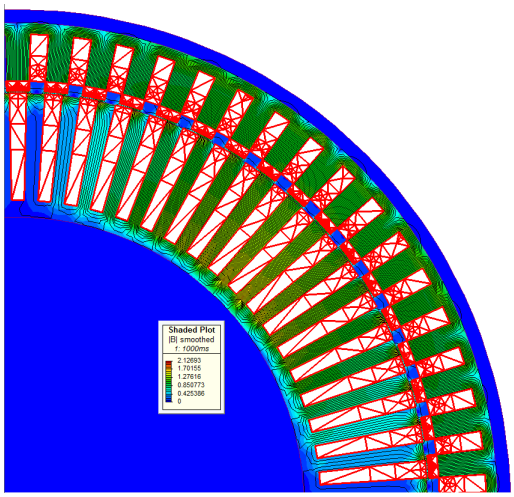

(a) Flux lines for the surface-PM VFSG

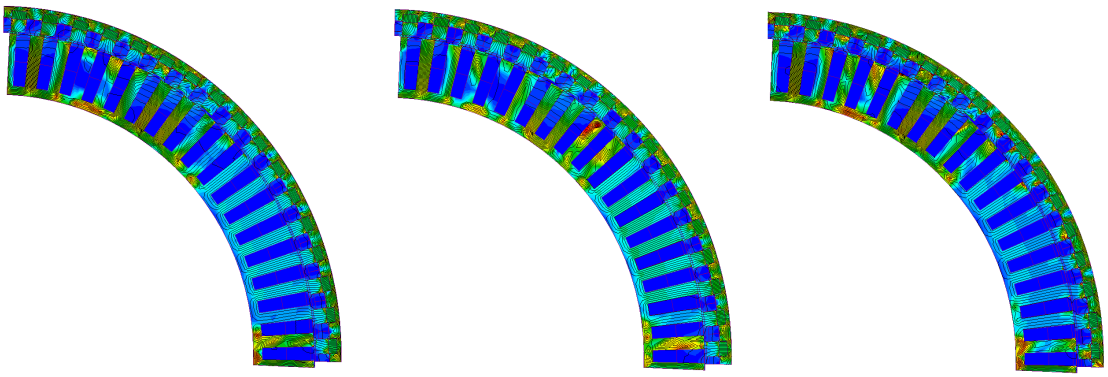

(b) For the buried-PM VFSG under the three three working conditions ofthe MMF sources (weakening (I_{rfc}= -1 pu), normal ($I_{rfc} = 0$), boosting ($I_{rfc} = 1$ pu))

Figure 5.11: Flux density distribution of chosen optimum designs

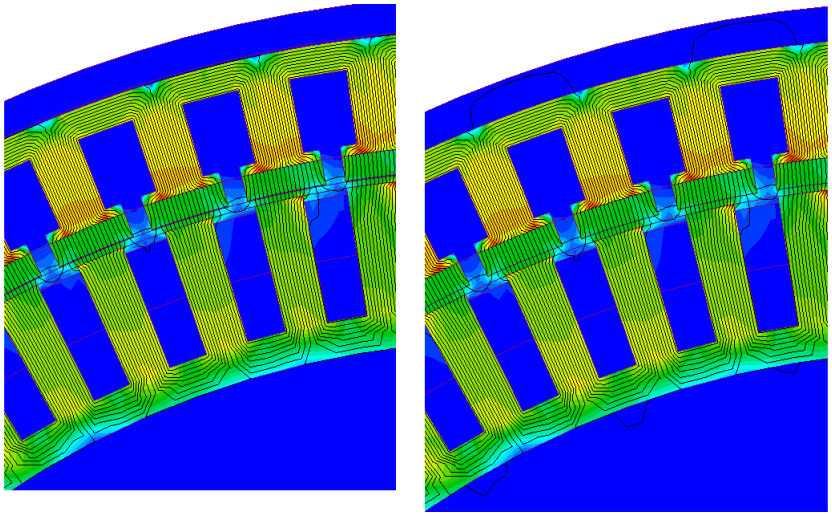

Figure 5.12: Flux leakage that occurs in the surface-PM design 1.

5.4.1 Rotor PM Demagnetisation

The hard magnetic material used on the PM rotor is sintered neodymium-iron-boron, NdFeB that has a linear 2nd-quadrant B-H characteristic at 20^0C. However, at higher temperatures, say 120 ^{0}C, the 2nd-quadrant characteristic becomes non-linear and there is potential for recoil working of the material. In terms of recoil working, an important area to consider is demagnetisation or partial demagnetisation due to the thermal operating environment of the permanent magnet. A typical open-circuit load line and how the 2nd-quadrant characteristic becomes non-linear with elevated temperature is shown in Figure 5.13. N48H has the material characteristics for the prototype generator. However it is not anticipated to reach temperatures higher than 75^0 C which is a safe operation temperature. The risk of rotor PM demagnetisation is taken in post-processing, where information was analysed to calculate the $B - H$ working point of each element defined in the rotor FE mesh. Figure 5.5b illustrates one of the rotor PMs with its internal mesh elements (triangles). Each of these elements has a varied flux density value that is dependent on the particular element as well as the rotor position. The flux density value for each rotor PM element is projected on the PM material demagnetisation curve to ensure that they are of the desired operating limits. In this analysis, each material is specified in the 2-D MagNET generator model with numerous mesh elements. Each mesh consists of three nodes, each of which constitutes an X, Y coordinate and vector potential as shown in Figure 5.5b. They are then solved using data from the MagNet solver, as clarified in the tutorial [49].

5.5 Observations and Conclusions

In this chapter, there is a description of how rotor field coil analysis was performed using FE analysis in MagNet solver to numerically evaluate four generator designs from a benchmarked

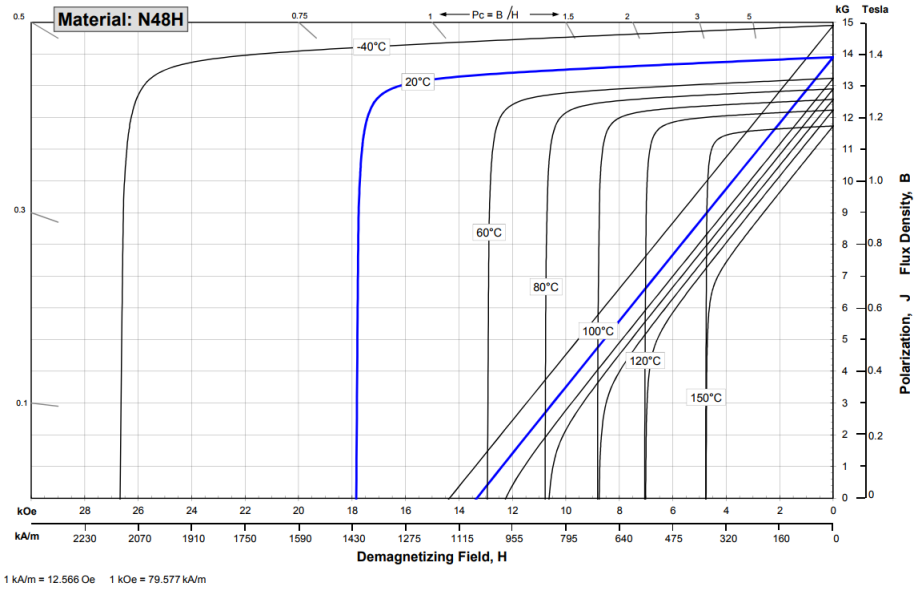

Figure 5.13: Rare-earth PM (NdFeB-48H) magnetic characteristics.

surface-PM VFSG calculated analytically. The electromagnetic analysis is carried out to satisfy grid compliance design. From the analysed rotor designs, it was found that the rotor slot area is a key constraining factor. Another key outcome of the study is that the location of the PMs on/in the rotor tooth where buried-PM design yields the rotor choice as it produces the highest stator flux linkage (ψ_S) with the lowest values of I_{rfc}, J_r, P_{rfc}, and V_{rfc}.

The magnetic circuit representations of the PM VFSG designs were obtained and the magnetic flux calculated by using FE analysis in 2D FE solver. The numerical results for the generator designs were successfully compared and showed good correlation with expected performance. In addition, the design topologies were investigated for their NO-load and rated back-EMF waveforms as well as their rated loss performance for a specified stator slot current density. The validity of the static FEM results for the PM VFSG wind turbine system with direct grid connection, was confirmed by a transient analysis in normal and boosting modes. In both cases, the flux densities in the back-irons, stator windings and rotor windings did not go beyond the maximum set value of 2 T. Thus, this alleviates the necessity of thermal analysis.

The best design for the grid compliant PM VFSG with the specific advantages is the combination of buried-PM and series rotor field coils in the rotor's open slots.

Chapter 6

Design Optimisation

The design optimisation of a grid-compliant permanent magnet variable-flux synchronous generator (PM-VFSGs) is a non-linear multi-objective problem. The solution to the electromagnetic problem of such generators is an iterative procedure with the classical objectives of minimal mass, reduced losses, and cost among others. In this chapter, a description of a design optimisation procedure for a grid-compliant PM-VFSG is presented. The aim is to achieve an optimum generator model, using design analysis and $d-q$ transformation at rated load and other operation points, defined by machine design specifications as well as grid-compliance specifications.

The optimisation process achieves this in two parts: (a) a no-load and steady state optimisation and analysis of the generator at normal generator operation using a novel approach that utilises a common representation for performance analysis, $d-q$ transformation, and MMF sources supply; and (b) a grid code specification design that exploits the optimum design using the control strategy of reactive power compensation to provide a combination of capabilities that is not reported in any previous wind generator optimisation approaches in literature.

The optimisation procedure involves the use of a commercially available generic optimisation software tool Visual DOC, analytical and FEM models. Three optimisation algorithms, Modified Method of Feasible Direction (MMFD), Particle Swarm Optimisation (PSO) and Non-Sorted Genetic Algorithm (NSGA II) search algorithms, are used with the aim of obtaining a global optimum with reduced computational cost that encapsulates all the design and grid-code inputs, constraints and objectives.

6.1 Optimisation

The overall design optimisation of the grid-compliant wind generator consists of initial aspects defined by design (dependent on material, mechanical and thermal) and secondly, aspects defined by the grid code requirements of voltage, power factor and reactive power. The optimisation algorithms available to achieve the best solutions for such generators can

be divided into deterministic or stochastic types.

The deterministic approach constitutes a scalar objective, which utilises a fitness function with a unique solution [53]. These methods exhibit a fast convergence in spite of gradient calculation. The main drawback of these methods is the convergence to a local minima.

The stochastic methods use iterative improvement processes with either a single output solution [22, 54–63] or population based outputs [4, 64–75]. These methods require more evaluations of design candidates but are gradient-free. Solutions of these stochachastic methods can be trapped by local minima only if the fitness function is poorly defined [76]. To solve problems, randomisation and local search are used by stochastic methods. A reduced computational cost can be achieved in the population-based algorithms by use of high performance computing techniques such as parallel computing [72, 77].

6.1.1 Gradient-based methods

These optimisation methods fall under the deterministic methods discussed above. A large variety of gradient methods are applied to machine design optimisation problems. A gradient-based optimization of permanent magnet generator design for a tidal turbine was carried out in [76]. Another typical example is the sequential quadratic programming (SQP) that first converts a constrained optimisation problem into a unconstrained one by penalty function and then applies sequential non-linear programming (BIGDOT) for optimization. SQP is able to converge to an optimum solution after a few iterations but requires gradient calculation. This method has been deployed for on-load calculation of HESG [22]. This method is very similar to Sequential Unconstrained Minimisation Technique (SUMT) [56] or sequential non-linear programming in machine design optimisation that are reported in [55] [78].

Other deterministic methods include error-based optimisation search [61], Hooke-Jeeves [62], Interval Branch and Bound method [63], interior-reflective Newton method [79], a combination of the sub problem approximation method and the first-order method [80], inverse problem method [81], and MMFD [5, 13, 46, 50]. A major drawback of gradient based search is the inability to use integer variables [76]. The MMFD is the algorithm in this category that is chosen to be used in this research as there are no integer variables in the optimisation procedure. The number of slots and poles are chosen and fixed during the optimisation process.

6.1.1.1 Modified method of Feasible direction (MMFD)

MMFD is a gradient-based method, that converges to a solution within a few iterations and easy is to implement [46]. MMFD is based on obtaining a sequence of feasible directions, that is directions that reduce the objective function while satisfying the constraints. The disadvantages include being trapped in a local minima [46, 50, 53, 76] and poor performance when constraints are highly non-linear or discontinuous.

6.1.2 Non-Gradient based methods

There are two main categories of the non-gradient-based methods that include techniques using genetic adaptation and those that are based on collective social behaviour. These methods require more evaluations of design candidates but are gradient-free and are not trapped by local minima. Examples of the former are genetic algorithm (GA) [64, 69–73, 75, 82–86] and differential Evolution (DE) [77]. They are population-based techniques, with performance criteria on survival-of the fittest. Other algorithms that have incurred interest in the recent years include the gravitational search algorithm. This is an algorithm inspired by natural behaviour and based on the Newtonian gravity. It has been used to optimise a PMSG for a vertical axis wind turbine [87].

The GAs are the most used optimisation techniques in machine design. With three genetic operators involving selection, crossover, and mutation, GA is efficient specifically where no mathematical representation is present, there is large and complex design space, it works with its own internal rules and is also used for problems that have a complex definition or are difficult to define and in case of a search space when the designer has little knowledge of the domain.

The DE just like the GAs uses populations of individuals to search for an optimal design. The mutation in the DE unlike that in the GA is as the result of an arithmetic combination of individuals. The DE is considered to be a reliable, accurate, robust and fast technique [53, 77]. When the optimisation process commences the performance of the algorithm is favoured by an exploration process of the mutation operator. As the evolution advances, the mutation operator favours exploitation.

Another method is the Ant Colony that has been used when optimising a PMSG for a DD wind turbine in [88]. Optimisation in this category constitutes a vector objective, which utilises a fitness function with a set of satisfactory/good solutions such as NSGA-II, or PSO algorithm that constitutes a scalar objective, which utilises a fitness function with a unique solution. In this work, non-gradient-based methods of PSO and NSGA-II algorithm are utilised to carry out the design optimisation of a PM VFSG

6.1.2.1 Particle Swarm Optimisation (PSO)

The Particle Swarm Optimisation (PSO) emulates the behaviour of a swarm of bees trying to locate places with the highest density of nectar/flowers [77] [66] where the optimal search is attained by a combination of self and swarm knowledge [74]. A representation of the process is as shown in Fig. 6.1 by Duan.

Implementation of PSO is such that in each iteration, every particle updates its position (6.1) and velocity (6.2) according to the following

$$X_{k+1}^{i} = X_{k}^{i} + \upsilon_{k+1}^{i} \tag{6.1}$$

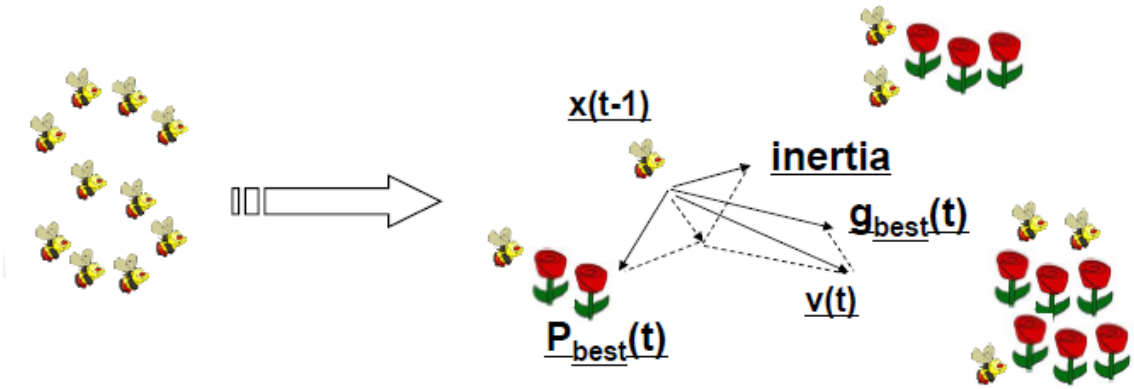

Figure 6.1: PSO optimisation process [4].

$$v_{k+1}^{i} = c_1 r_1 (P_{best,k}^{i} - X_k^i) + c_2 r_2 (g_{best,k}^{i} - X_k^i) \tag{6.2}$$

where

v_{k+1}^{i} is the particle velocity

X_k^i is the particle's position

c_1, c_2 are constants for self acceleration and social acceleration

r_1, r_2 are random numbers with values between 0 and 1

$P_{best,k}^{i}$ is the best position at the k-th iteration of a particle

$g_{best,k}^{i}$ is the best position at the k-th iteration of the swarm

PSO is robust to the values of its running coefficients [77] and hence by simply following a few guidelines [66], unlike in the case of DE, the PSO algorithm eliminates the need for manual tuning of the running coefficients / control parameters. PSO has a better diversity in the swarm than GAs the population of which evolves around a subset of the best individuals. It further has a more effective memory capability than GA. These attributes make PSO a choice as an optimisation method in this research where a single objective is used.

PSO is applied in [89] to a SMPM, to optimise a synchronous reluctance motor for traction applications, and in [77, 90] to induction machines. A better performance of PSO is achieved by several methods such as Auto-Tuning Multi-Grouped Particle Swarm optimisation (AT-MGPSO) proposed in [ch6] for optimizing multi-model functions and applied in [91, 92] to optimize an IPM generator. The mostly adopted way is to create a Pareto repository to store all the non-dominated solutions where personal or global best are selected and the particles are still moved as single-objective PSO. Vector optimisation targets to meet the optimal conditions for several objectives yielding what is commonly referred to as a pareto optimal front. A pareto-optimal solution occurs if the improvement of one objective function simultaneously decreases at least one of the other objective functions [93]. A multi-objective PSO (MOPSO) is an adaptation of scalar searching algorithms yielding multi-objectives target. Proposed ways of selecting *pbest* and *gbest* include a random selec-

tion [94] from the whole pareto repository, and from a specified portion of the repository based on certain pareto ranking scheme [95]. More examples and comparisons of MOPSO with other multi-objective algorithms can be found in [95, 96]. An important issue for MOPSO is how to select the personal and global best [66, 94, 96].

6.1.2.2 Non-sorted Genetic algorithm (NSGA-II)

The non-sorted genetic algorithm (NSGA-II) is an evolutionary algorithm proposed in 2002 [97], that is gradient free, has a simple implementation, is fast and effective, and makes use of multi- objectives and multiple solutions. Discrete values such as the number of turns, rotor poles ($2p$) and stator slots (Q_s) can be used in the optimisation procedure [46]. With all the properties of the GAs it further has the properties of a fast non-dominated sorting procedure, an elitist strategy, a parameter-less approach and a simple yet efficient constraint-handling method [46].

Since none of the vectors dominate, they are equally good solutions which provide invaluable insight to the decision maker on how to choose the best design to satisfy performance criteria. These non-dominant solutions belong to a pareto optimal set [53] .

Steps to implementing NSGA-II as mentioned in [97] involve:

i) Generation is a set of individuals or members,where each individual presents one generator design. The initial generation is randomly chosen inside the boundary constraints.

ii) Candidate population is obtained by a crossover and mutation process from the existing population.

iii) Next generation is obtained by comparing the existing candidate population by choosing members that satisfy boundary functions and/or have better objective functions.

iv) Search through the design space is either discrete - floating values or integers.

v) Stopping criterion is the maximum number of iteration that is chosen in the beginning.

This can be summarized as in Figure 6.2. of [97] where

- R_k is a combination of parent population $P_{NSGA,k}$ and children population $Q_{NSGA,k}$,
- $F_{NSGA,i}$ are the best solutions in the combined population
- $P_{NSGA,k+1}$ is the new population of size N that is used for selection, crossover and mutation to create a new population $Q_{NSGA,k+1}$ of size N.
  NSGA-II, is deemed the best choice for optimising PM VFSG designs with many diverse solutions.

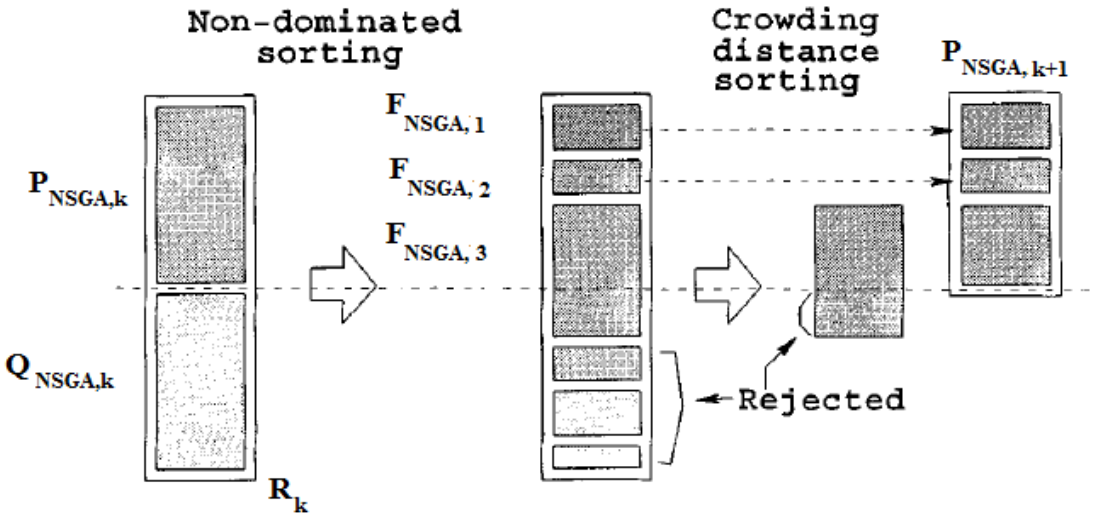

Figure 6.2: Implementation of NSGA-II [97]

.

6.2 Design model and optimisation procedure

6.2.1 Design aspects and considerations

An outer rotor topology's advantage is that for a given volume the air-gap diameter is large. The performance of the double excitation is that PMs produce the nominal MMF required for the normal operation of the generator. The rotor field coils then supply additional MMF that boosts the PMs flux just enough to achieve grid compliance. This operation principle ensures maximum PM excitation advantages that include high efficiency, reduced mass and allowing the use of high pole/slot numbers that lead to reduced end winding. The MMF from the PMs therefore produces a nominal constant flux linkage in the stator coils, whereas the MMF from the copper excitation produce flux that is dependent on the amount and direction of the current supplied to the rotor field coils. The NdFeB-48H type of PMs are chosen as they will lead to a generator with lighter weight and reduced rotor copper losses which are the key aims in the optimisation. Depending on the position of the magnets, two generator topologies can be achieved in the design procedure i) the magnets are placed on the rotor surface, termed as surface-PM VFSGs, or ii) buried in the rotor cores, and called buried-PM VFSGs. The rotor core is slotted on either side of the magnet pitch, and the slots filled with copper field coils on either side of the PMs. The rotor field coils are then all connected in series.

Table 6.1: Generator design specifications for the three power levels

Parameter	Value
Rated power P_{13}, P_{100}, P_{1MW}	13, 100, 1000 kW
Rated voltage V_{rat}	400 V line to line
Rated speed ω_s	88, 44, 22 rpm
Maximum voltage V_{max}	$1.1V_{rat}$
maximum rotor loss ratio $P_{rotloss}$	1 W/kW
Efficiency η	≥ 94,
Torque T_{13}, T_{100} , T_{1MW}	1.4, 21.6, 432, kNm
Poles $2p$	68, 136, 272
Slots Q_s	72, 144, 288
Reactive power Q, (pu)	0.228, 0.228, 0.31
Power factor $Cos(\varphi)_{min}$	0.95 or 0.975
Air-gap length, g	2, 2, 4 mm
Slot fill factor K_{ff}	0.5
Rotor bridge thickness	1.5,1.5, 5 mm
PM type (NdFeB-48H)	1.4 T
Maximum air-gap diameter, D_{gmax}	6000 mm
Stack length, $L_{stk,max}$	1500 mm

Table 6.2: Cost of active material per unit mass for the prototype.

Material	NdFeB-48H	Iron	Copper
Cost($/kg)	104.9	74.63	26.92

6.2.2 General design optimisation

The design specifications for the different power levels is provided in Table 6.1. It is shown that for the pole slot combination of the 13 kW is 68/72, which is from a base winding of 34/36 as previously discussed. With increase in power level, the number of poles and slots increase too. In this work is adopted that for the 100 kW generator the speed is approximately 44 rpm hence the choice of 136/144. Further reduction in the speed by half to 22 rpm is adopted for the 1 MW with the pole/slot considered being 272/288. All the power levels have the same base winding with varied machine sections.

Several design optimisation procedures of wind-turbine synchronous generators have been carried out [15, 18, 45, 85, 88, 89, 98–105]. In Figure 6.3, the general design procedure for the studied grid-compliant wind generator is presented. The optimisation procedure is divided into two main parts. After the initialisation, the electro-mechanical design is carried out to the satisfaction of the design specifications. From the initial dimensions, and the chosen pole/slot combination, the conductors and cores dimensions are optimised based on the electric and magnetic constraints. after the electromechanical design is complete, the generator characteristics, specific losses and efficiency are calculated and tested if they meet the set goals. After which, the grid compliance optimisation follows. In this part, the rotor

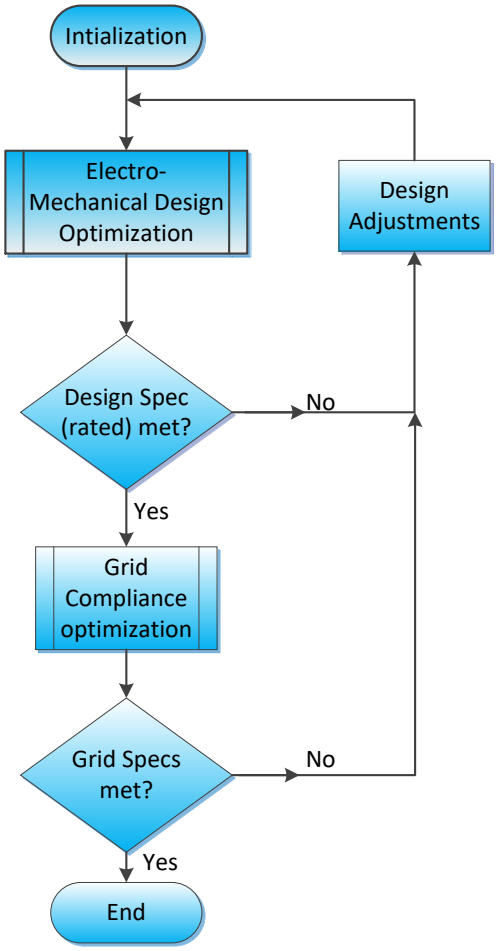

Figure 6.3: General flow chart for the design optimisation.

dimensions is critical. If the grid requirements of voltage, reactive power are not met the process is then iteratively solved till convergence.

6.2.3 Objectives of the optimisation

The objectives of the optimisation are:

1. To minimize total active mass M_{Tot}, and
2. To minimize rotor copper loss $P_{Cu,r}$.

subject to

1. Efficiency $\eta > 0.94$
2. Torque$T = T_{rated}$

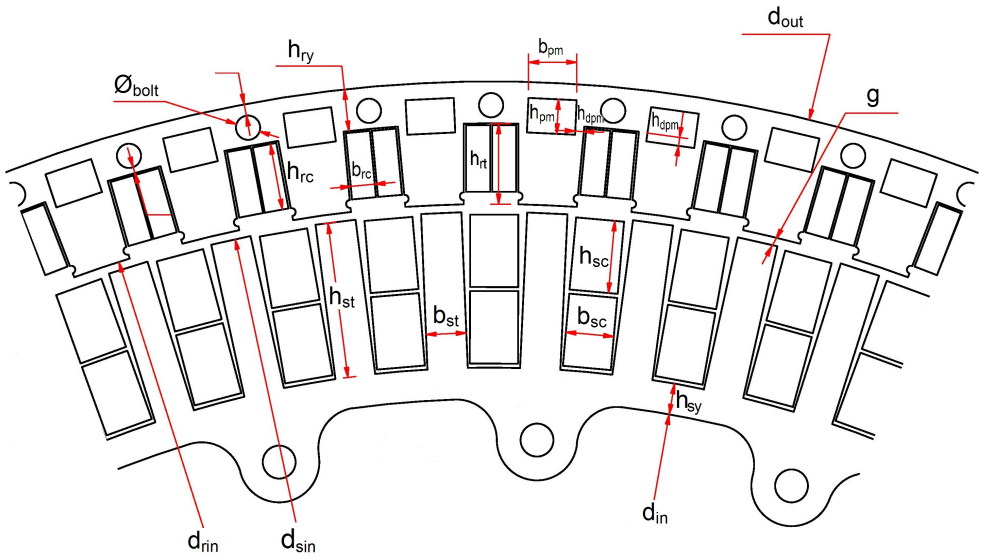

Figure 6.4: Cross-section of the generator with the variables used in the design optimisation.

3. Power-factor $cos(\theta) = 1, 0.975, 0.95$ (depending on power-level and generator operation)
4. Reactive power $Q_{gen} \leq 0.228$
5. No-load voltage = grid voltage $V_{N-L} = V_{rat}$
6. Maximum voltage $V_{max} = 1.1V_{rat}$

Due to the fact that flux variation is a prerequisite in the design model, a balance between the amount of MMF produced by the PMs and that of the copper excitation has to be reached. In [8, 24, 25] hybrid values are calculated and studied. In this research, it is taken that the 1 pu value of the total MMF is produced by the PMs and the approximate 0.1 pu incremental is produced by the rotor copper excitation. As deduced in this work, such operation yields in a generator model with grid compliance capability, reduced total mass, high efficiency and, in the event of failure in the rotor field excitation, the PM- VFSG can operate to rated performance as a conventional PMSG [6, 10].

6.2.4 Design variables

The optimisation procedure is carried out with 15 dependent and independent variables shown in Figure 6.4. and defined in Table 6.1. and Table 6.3. In the initial stages of the optimisation, the no-load voltage/ EMF from the PMs and when rotor field coils have a current supply are considered as variables. The variables are determined from winding and design factors such as

- Number of layers, pole-pitch, 2p
- Number of turns N_r, N_s,

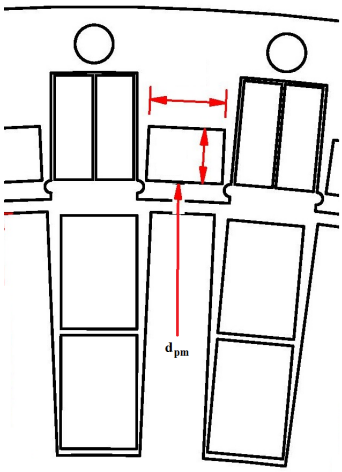

Figure 6.5: Cross-section of the generator topology showing d_{pm} variable with the lowest value specified in Table 6.3with PMs at the top of the rotor tooth. It will then vary to $d_{pm} = 1$ as in Figure 6.4. In the beginning of the optimisation $d_{pm} = 0$ when surface-PM designs are optimised.

Table 6.3: Variables and their ranges used in the design optimisation

Variables description	Variables and range
Stack length ratio	$0.3 \leq L_{stkP} \leq 2$
Air-gap diameter ratio for 13kW, 100kW, 1 MW	$0.08, 0.1, 0.3 \leq D_g \leq 1$
Stator tooth width to slot pitch ratio	$0.28 \leq b_{st}/\tau_s \leq 0.72$
Stator yoke height to stator coil height ratio	$0.2 \leq h_{sy}/h_{sc} \leq 1$
Rotor tooth width to pole pitch ratio	$0.28 \leq b_{rt}/\tau_p \leq 0.72$
Rotor yoke height to rotor coil height ratio	$0.2 \leq h_{ry}/h_{rc} \leq 1$
Stator and rotor current densities	$[2 \leq J_s, J_r \leq 12]\ A/mm^2$
PM depth into the rotor tooth	$0, 0.15 \leq d_{pm} \leq 1$

- Coil diameter
- Core, PM and winding material
- PM height
- Magnetization direction
- Teeth and slot type
- Inner and outer diameter
- Stack length

6.2.4.1 D_{pm} as a design variable

To generalise the design optimisation procedure, a variable d_{pm} is defined such as when its zero, the generator designs are optimised as surface-PMs and when it varies according to Table 6.3, then its a buried-PM topology as defined in section 6.2.1.

6.2.5 Design constraints

The aim is that the optimal designs obtain high efficiency with

i) $V_{nom} = V_{grid}$ produced by PM flux

ii) $P_{Cu,r} \leq 1\%\ P_{rat}$ rotor copper loss

iii) At V_{grid}= $1.1V_{nom}$ then $Q_{grid} = 0.228$ pu

iv) B_{max} =1.8T in any point in the generator

Constraints:

- PM type B_r=1.4T
- Air-gap size=2 mm
- Current density of field coils $J_s = 6$ and $J_r = 6$
- Slot fill-factor $K_{ff} = 0.5$
- Winding factor $K_w = 0.953$
- Flux density in the teeth and yoke cores $B_{t,max} = 1.8\,T$ and $B_{y,max} = 1.5\,T$
- Air-gap flux density $B_{g,min} = 0.7\,T$.

6.3 Problem formulation

In the four topologies studied in this work, a double layer stator core with 72 slots is adopted. In the modelling procedure in FEM, a quarter-section is used having 18 slots and with negative periodicity as discussed in chapter 2. The rotors considered are :

1. Surface-mounted-PMs which can further have a) open slots and straight teeth or b) semi-closed slots with straight slots.

2. Buried-PMs with open slots and straight teeth, and these are further divided according to the rotor coils as a) double layer and b) single layer.

For all the designs a clearance for the magnetic wedge is allowed to enhance the end tips as well as the teeth bridges that ensure mechanical strength as well as saturation effects of the teeth.In all the generator designs considered, the air-gap diameter, number of poles and slots, frequency and speed values summarized in Table 6.1 are taken as constants. The air-gap diameter is fixed to a value of 0.62 metres (for the 13 kW generator). The current densities in both the stator and rotor vary as the stack length varies. The MMF from the PM flux produces the no-load voltage (400 V as specified in Table 6.1). The NdFeB magnet remanence and relative permeability are equal to 1.4 T and 1.01, respectively. The steel lamination taken for the construction of both stator and rotor cores is M530-50A. The stator and rotor geometric design parameters and corresponding ranges used in the design process are summarised in Table 6.3. It should be noted that in the case of the semi closed surface-PM and open slot surface PM generator designs, 17 and 15 dependent and independent parameters are used respectively in the design procedure. Whereas, for the

open-slot buried-PM double layer rotor and open-slot buried-PM single layer rotor designs, 16 and 15 design parameters are used respectively, in the design optimisation procedure.

An additional search of an optimum current angle that results in maximum torque production at unity power factor or there about is performed for every generator design solution. In the optimisation procedure using the $d-q$ analysis, the number of rotor turns is calculated at no-load for the increased grid voltage. With the voltage and current achieved as described in the previous chapter, the reactive power capability is searched at rated operation. As shown in the flowchart of Figure6.3. the procedure is hastened by having the designs that satisfy design requirements going to be optimised for grid specifications. The 4 topologies (surface-PM and buried PM) as mentioned above, with variables as shown in Figure 6.4. are evaluated with 2,500 possible designs each, resulting in a sum of 10,000 design evaluations. Each design topology consumed varied simulation time depending on the optimisation method utilised as given in Table 6.4. This is discussed in techniques that make use of meta-heuristic methods [87, 88, 103, 106](e.g., GSA, ,PSO, NSGA-II) have been shown to be scalable, but one or two orders of magnitude slower than those that use heuristic methods [8, 76] (e.g., MMFD or SQP). With the MMFD having the least time and NSGA-II the longest time of up to 18 days on a typical desktop computer with dual core processor and 16GB RAM. It should be noted that the longer times could be due to other programs running or the interfacing of other softwares that included MagNet solver, Visual DOC, Python scripts, and Notepad scripts. A faster evaluation is possible with the use of parallel computing [77], or CE-FEA as in [107, 108]with multiple cores.

Table 6.4: Comparison of simulation time for NSGA-II with PSO and MMFD optimisation algorithms.

Power level (kW)	NSGA-II	PSO	MMFD
13	0.274	0.061	0.000945
100	0.275	0.063	0.0018
1000	0.26	0.083	0.0013

6.4 $d-q$ modelling

The proposed model allows for each generator design to be evaluated specifically with regard to topology as well with individual design performance. The overall model is chosen to converge to a solution with minimal computation time to estimate the control strategy on the wind generator system. With the afore-mentioned aims, the modelling is based on the steady state $d-q$ equations of the generator, equations (6.3) - (6.8) and the phasor diagram represented in Figure 6.6. According to these objectives, a classical first harmonic model based on a synchronous $d-q$ reference frame is developed in (6.3) - (6.5). The novelty of this model is that it can be solved by using flux linkages in $d-q$ reference frame taking into account the currents at no-load and rated operation while considering grid-compliance.

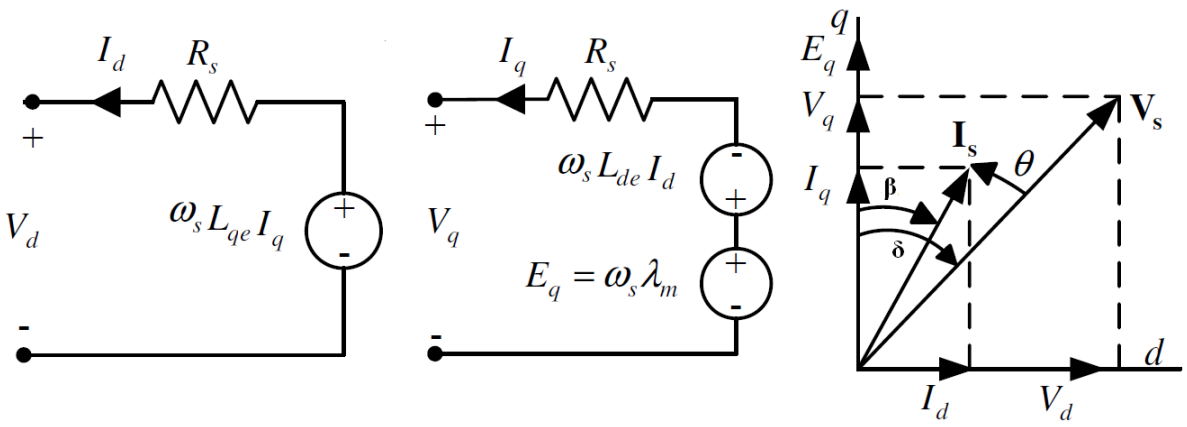

Figure 6.6: $d-q$ equivalent circuits and phasors for modelling the grid-compliant PM VFSG models.

The operation at both states is such that the magnetic saturation and armature reaction are evaluated. Secondly, the flux at both operation modes considers the excitation with PMs only and also a combination of excitation sources.

$$V_q = -R_s I_q - X_d I_q q + E_0 \tag{6.3}$$

$$V_d = -R_s I_d + X_q I_q \tag{6.4}$$

$$T = \frac{3}{4} p[(L_q - L_d) I_d I_q + \lambda_m I_q]. \tag{6.5}$$

The no-load voltage developed is from the PM flux and the rated speed using $E_0 = \lambda_m \omega_s$. The V_d and V_q voltages are dependent on the maximum grid voltage ($V_{max} = \sqrt{2} V_{rms}$) and the load angle ($\delta$)

$$V_d = V_{max} sin(\delta), \;\; V_q = V_{max} cos(\delta) \tag{6.6}$$

whereas the $d-q$ currents depend on the maximum stator current ($I_{max} = \sqrt{2} I_{rms}$) and the current angle (β)

$$I_d = I_{max} sin(\beta), \;\; I_q = I_{max} cos(\beta). \tag{6.7}$$

The voltage evaluation is done with $V_{max} = V_{grid}$ at nominal grid voltage (PM flux only), and when it is equal to $V_{max} = 1.1 V_{grid}$ (PM and rotor field coils flux).

6.4.0.1 Inductances and $d-q$ flux linkage calculation

The $d-q$ inductances are then found from the known flux linkages and currents as

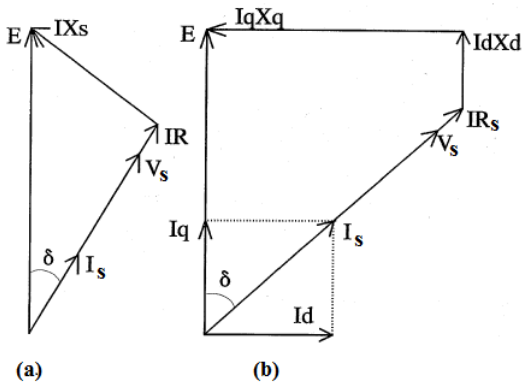

Figure 6.7: Phasor diagram at unity power factor for (a) surface-PM VFSG, and (b) buried-PM VFSG with inverse saliency.

$$L_d = \frac{\lambda_d - \lambda_m}{-I_d}, \quad L_q = \frac{\lambda_q}{-I_q} \tag{6.8}$$

The uniqueness of this $d-q$ modelling lies in getting the $d-q$ flux linkages. The $d-q$ flux linkages are acquired from FE static solutions as in [22, 50]. Each generator model is drawn in MagNet and its topology is unique. The *d-axis* flux-linkage takes into account the rotor MMF sources as well as the $d-axis$ stator current. On the other hand the $q-axis$ flux-linkage depends on the $q-axis$ current.

6.4.1 Current angle evaluation for maximum torque production

As the PM VFSG operates in an uncontrolled wind turbine system, the β has to be solved in order to simulate the steady state performance of the generator.

The variable-flux PMSG operates in an uncontrolled system as shown in Figure 2.2. Therefore the currents of (6.7) have to be solved in order to simulate the steady state performance of the generator. For quick simulation results the $d-q$ inductances of the generator are first determined as functions of current. Several methods are mentioned in literature such as the load test method. This study evaluates λ_m at no-load (stator current switched off), and the $d-q$ flux-linkages at different loads from static FE solutions. From the calculated values, and an arbitrary chosen value of β and then using (6.7).

Three unknowns, $d-q$ inductances and the load angle δ, can be solved from the three equations (6.6) - (6.8). The solution steps followed are:

1. I_{rms} is calculated from the rated power and the power factor,.

2. λ_m is calculated at no-load from the FE solution after the correct choice of stator turns. It is assumed that at load angle δ, and current-angle β are zero. λ_d and λ_q are then calculated from (6.8).

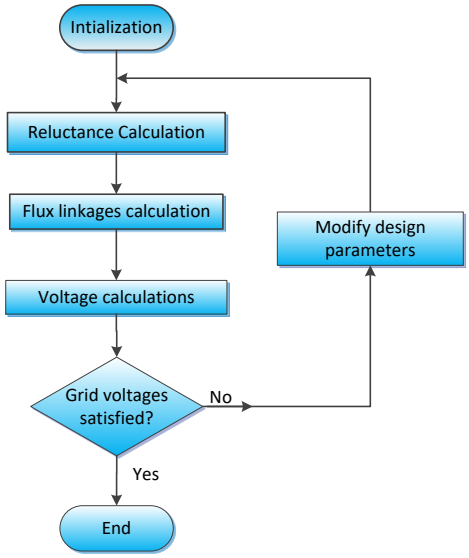

Figure 6.8: Flow chart of the iterative procedure in current calculation. (Note that the design parameters being modified are N_s, N_r, I_d, I_q, V_d, V_q, β and δ).

3. Initial values of I_d and I_q are calculated from the known value of I_{rms} and an arbitrary chosen current angle β.

4. The FE model uses the known currents and current angle to solve for L_d and L_q from their respective flux linkages as in (10). R_s is analytically calculated from the slot dimensions and the copper losses read from the FEM solution. End winding inductance L_{ew} is calculated analytically as in [] and added into the L_d and L_q values from $2-D$ FE values.

5. The initial values of L_d and L_q together with the λ_m and I_{rms} are then used to calculate new values of I_d , I_q and δ.

In the procedure of optimisation to satisfy reactive power and higher (boosting) no-load voltage, the procedure with the current evaluation follows the flow chart as in Figure 6.8. In the current evaluation process, the objective is to find the unique solution (of I_d, I_q, β, N_s, N_r, I_{rfc}) that satisfies each operating point of the generator (V_s, I_s and $\cos(\theta)$). Then, the generator performances (P_{rat}, Q_{grid}, η) associated with the operation as per the grid codes are determined.

6.4.1.1 Power and reactive power calculation

The active power generated is calculated from the voltage, current and power factor by

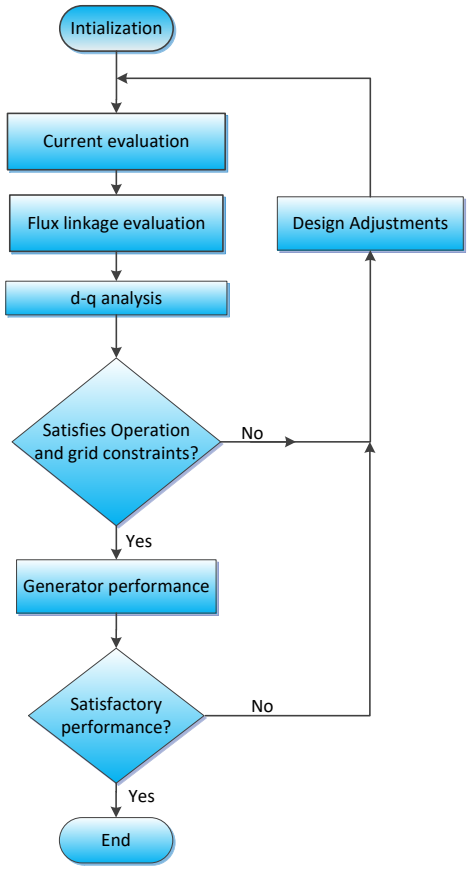

Figure 6.9: $d-q$ axis analysis and performance evaluation flow chart

$$P_{gen} = 3V_{rms}I_{rms}cos(\theta), \tag{6.9}$$

and the reactive power delivered to or absorbed from the grid as

$$Q_{gen} = 3V_{rms}I_{rms}sin(\theta). \tag{6.10}$$

6.4.1.2 Efficiency evaluation

The efficiency of the generator is then calculated from the torque, speed and losses as

$$\eta_{gen} = \frac{T\omega_s - P_{loss}}{T\omega_s} \tag{6.11}$$

where P_{loss} includes copper losses, eddy current losses, core losses and the windage-and-friction losses.

The $d-q$ axis analysis for grid-compliance and performance procedure follows a flow-chart summarised as shown in Figure 6.9. This calculation employs the $d-q$ equivalent model coupled into the optimization problem in the grid-compliance sub-process of Figure 6.3,to find the good control for required design and grid specifications.

6.5 Optimisation: summary of contributions and conclusions

There are three key novel aspects to the deployed design optimisation procedure, which have not been reported in the existing literature:

(i) This work has described three optimisation methods which are needed to achieve scalable design optimisation analysis for grid compliant PM VFSG. It is shown that $d-q$ analysis can be used with the three different optimisation algorithms in the design optimisation of wind generators with minimal computational cost.

(ii) The optimisation procedure incrementally evaluates each design candidate for design specifications as well as grid specifications using the $d-q$ equivalent circuits in the analysis. The procedure uses a novel extension in the $d-$ and $q-$ current calculation permitting incremental discovery of flux linkages in the current evaluation, even when the designs and performances are varied.

(iii) The design procedure uses a simple mechanism ($d-q$ steady state and no-load circuits) to solve several design problems in $d-q$ analysis including current and voltage information, current evaluation with iteration, and power and reactive power requirements including correct handling of incomplete design sub-phases. This allows it to analyse portions of the procedures in parts of the design procedures (e.g $d-q$ analysis at a specific voltage value or current angle calculation).

(iv) The need to achieve a scalable "fully grid-compliant sensitive" optimisation procedure, has been fulfilled by the use of a unified approach. Combining design analysis,

grid-compliance and separate current evaluation, it makes sure that the analysis representation to grow large, despite using a deterministic field-sensitive representation in parts of the procedure.

(v) Design optimisation analysis is efficient and achieves convergence times that are comparable to non-grid-compliant designs using the same methods. This result indicates that, given a target analysis time budget, a generator design engineer can choose to implement either a gradient-based optimisation method (such as MMFD), or a non-gradient-based approach (such as PSO or NSGA-II algorithms with refinements). Finally, this scalability makes the procedure efficient enough to be reasonable for inclusion in commercial design tools (such as, Visual DOC).

The design optimisation procedure described is efficient and can be used in other methods and power levels. These application specifics do not affect the theoretical time bounds of the optimisation algorithm, but can make the design procedure faster on some PCs or programs. It is shown that the design procedure is extremely fast in practice (it takes less than 10hrs to obtain an optimum design with 15 or more variables), uses very little memory, and scales very well in analysis time and memory footprint for 10 benchmark solutions of MMFD solutions.

The method as a research contribution is achieved by using d_{pm} variable, which allows the optimisation to analyse both surface-PMs and buried-PMs VFSG topologies. Then key design details using $d-q$ analysis described make the design optimisation procedure efficient enough to achieve the objectives and carry out the necessary test points (of reactive power, nominal and over voltage and PM plus rotor field coil flux). These application specifics do not affect the general design procedure of a generator, but in-cooperate novel characteristics satisfying both design and grid specifications.

Chapter 7

Results and Discussion

The optimisation procedure of the grid-compliant PM VFSG for a slip-synchronous system described in chapter 6 is directly aimed at improving the performance of the wind-turbine application, that is for a PM VFSG to achieve grid-compliance through variable flux capability. The interesting aspects include: 1) How will the different optimisation algorithms perform when following the proposed method? 2) What is the aggregate performance impact of the optimisations? 3) What contribution to the aggregate impact does each optimisation make? Also, because Chapter 5 and 6 did not evaluate the performance impact with regard to higher power levels, it is done here. To quantify these aspects of the optimisations, the optimisations were ran on the same set of programs and on the same computer, with the same tools that were used to evaluate FEM modelling in Chapter 5 and Chapter 6.

7.1 Optimisation methods

The design optimisation of the studied grid-compliant PM VFSG was implemented in Visual DOC tool. Making use of $d-q$ transformation equations, FE analysis in MagNet solver and three optimisation algorithms (MMFD, PSO and NSGA-II that are in VisualDOC suite) with the procedure being automated using a python script. The script has initial values that are used to open the MagNet solver, draw the generator model, assign materials, solve static solution and then write out an output file. This output file is then used in a separate script with analytical equations and exports the output file to visualDOC for optimisation. The optimisation procedure solves the problem according to the inputs, variables, constraints and objectives and writes out an output file that is updated for a repeat to be sent to MagNet via the python script.

VisualDOC calls the python script, applies standard optimisation procedures to each task and links the initial input files and solutions to provide an output file for the iterative process. At first, the input files from the optimisation setup are computed into the script to draw the model into MagNet solver that has been opened by the script. The FE analysis solves static solutions and returns the solution to the python script for further analysis and

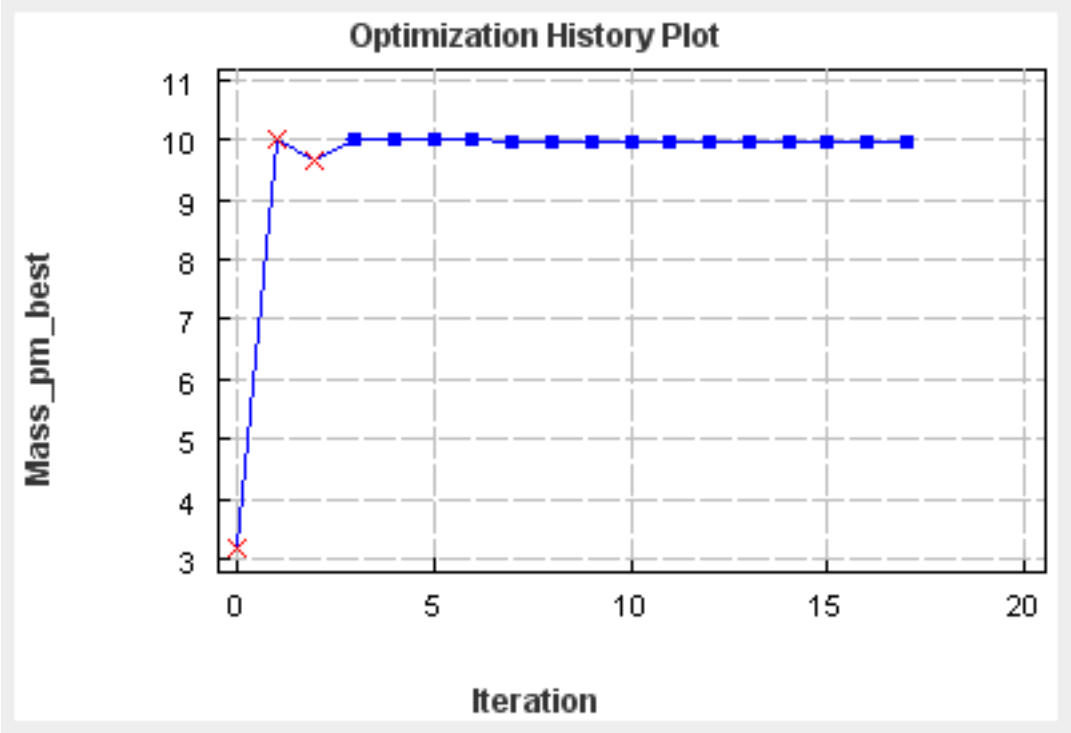

Figure 7.1: Convergence of solution using MMFD algorithm for buried-PM design with the mass PM in kgs .

additional analytical evaluations. The solutions are then passed into VisualDOC for the optimisation. Finally the optimum solution is printed out after all constraints are satisfied or otherwise and the procedure is terminated.

MMFD algorithm solves a single objective problem and gives a single output solution. The convergence rate is fast as shown in Figure 7.1. However, due to the problem of local minima, the starting points of the initial conditions are chosen for 10 different solutions. The advantage of this method is that after analytical evaluation of the design, the design space is small and the method is viable.

The PSO algorithm is of a scalar objective, which utilises a fitness function with a unique solution just like the MMFD. The advantage of the PSO algorithm is that the stopping criteria can be set for example once the solution repeats for a certain number of times say 10 or 15 times. As shown in Figure 7.2a the solution does not change after 40 iterations and the algorithm could have stopped after 55 iterations. This is unlike for NSGA-II that has to run all the iterations, as depicted in Figure 7.2b.

In the result presented in Figure 7.3 it is shown the variation of efficiency with increase in the total active mass for optimum surface-PM VFSG designs. A mass range of between 210 and 245 kgs can be chosen from the design optimisation. For the buried-PM VFSG designs, a total active mass of between 192 to 206 kg is shown.

The NSGA-II on the other hand has the advantage of multi-objective problem formula-

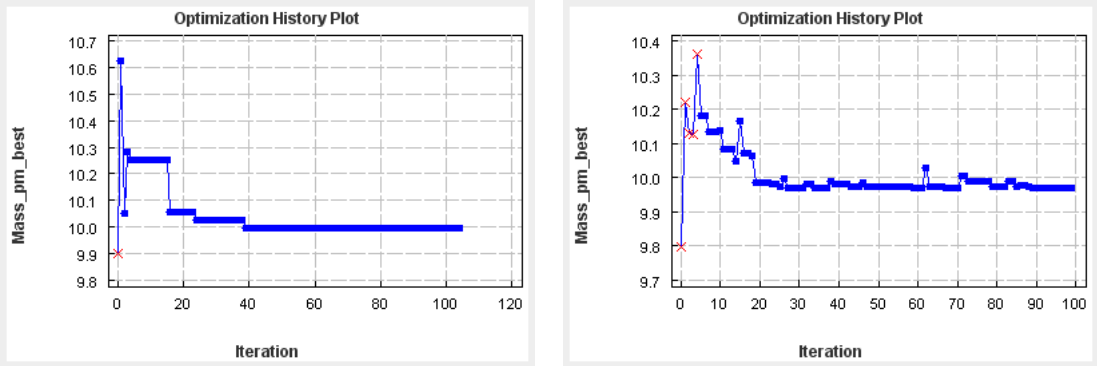

(a) PSO algorithm. **(b)** NSGA-II.

Figure 7.2: Convergence of PSO and NSGA-II algoritms for the buried-PM design and mass PM in kgs.

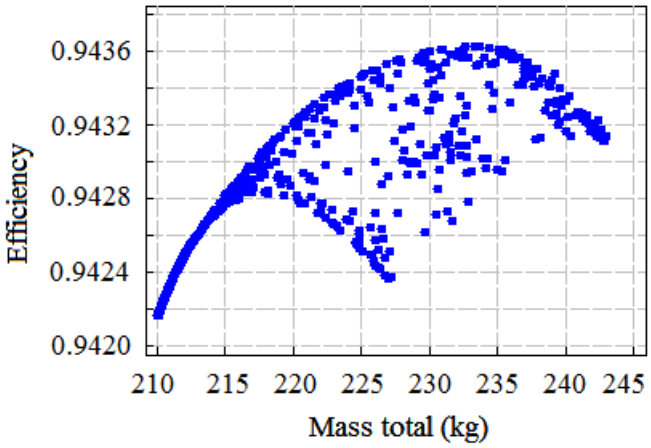

Figure 7.3: Pareto front for total active mass versus efficiency for a surface-PM VFSG design.

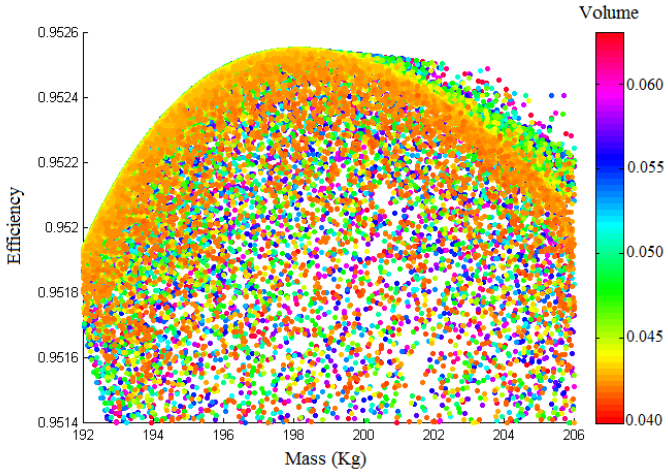

Figure 7.4: Pareto front for variation of Efficiency with total active mass buried-PM for 13kW generator.

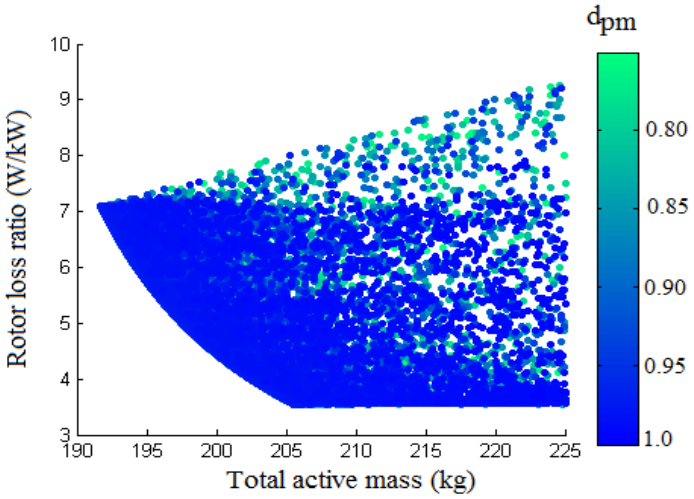

Figure 7.5: Pareto-front for rotor loss ratio with increase in total mass for buried-PM VFSG with colour code of how deep the magnets are buried in the rotor teeth.

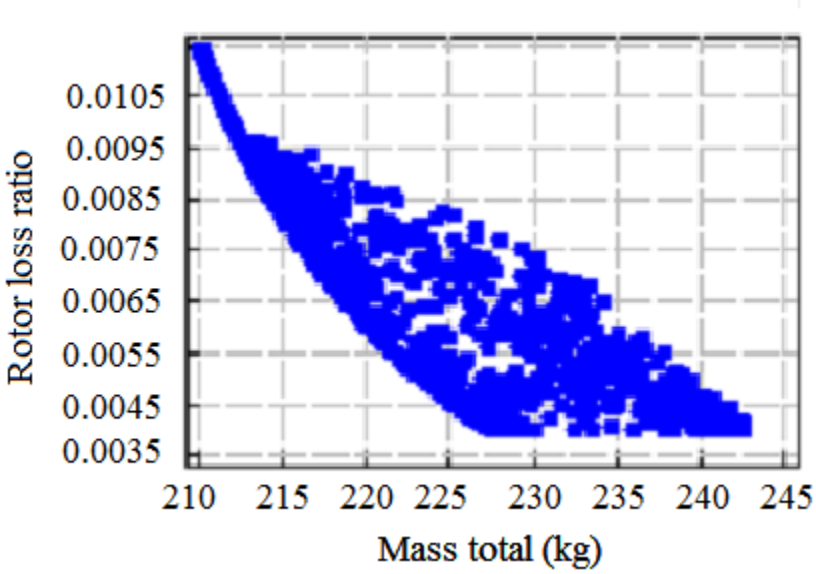

Figure 7.6: Pareto-front for rotor-loss-ratio versus mass of optimum surface-PMs VFSGs.

Table 7.1: Comparison of efficiency and mass values from the three optimisation methods.

Performance	MMFD	PSO	NSGA II
Mass surface-PM	200	200	218
Mass buried-PM	190	190	197
Efficiency surface-PM	0.938	0.94	0.943
Efficiency buried-PM	0.946	0.95	0.952

tion with a set of viable solutions, as shown in Figures 7.4 and 7.5. The solutions displayed in the pareto-front, allow an informed choice of the best solution of the optimum designs. This is as shown in Table 7.1, where the optimum design is selected by the designer putting in consideration other performances, for this study the rotor-loss ratio output.

7.1.1 Rotor-loss ratio

The rotor loss ratio defined as the loss of rotor field coils in watts to the rated power in kilo-watt (W/ kW) is shown in Figure 7.5 and 7.6. For this study, the rotor copper losses are evaluated twice: one when the generator is operating at rated load but can generate 0.223pu and secondly when the generator is running at no load and with 1.1 pu voltage. The higher copper loss is then used then used for the graphs. Each optimum design in the graphs are then depicted in colour to indicate the depth at which the PMs are buried in the rotor tooth-core as depicted in Figure 7.5. The $X - axis$ of the graphs shows the variation in total mass which ranges from 192 to 225 kgs. The $Y - axis$, on the other hand, depends on the ratio of the maximum amount of rotor copper loss to rated power for each candidate design.

From this results, it can be observed that the two objectives of minimum mass and minimum rotor loss-ratio are contradicting hence the use of multi-objective optimisation. A slight increase in mass results in better copper utilisation. This is an important characteristic for the designed machine as the PM VFSG needs to be competitive to both the PMSG (no field excitation losses) and non-PMSG (with field excitation losses). Obtaining a low copper mass for the excitation is a positive result for this research study.

7.2 Grid compliant 13 kW generator power level

For MMFD and PSO algorithms, the results of the optimum designs are one solution that is displayed. However, for the NSGA II, the optimisation results are pareto-fronts of non dominant solutions, the objective functions of which are depicted in Figures 7.5-7.4. The efficiency variation with increase in mass has the colour variation of each generator design with reference to their respective active volume. It was observed that the increase in mass due to the rotor field coils do not impede the generator efficiency performance. It is noted that an increase in the volume (attributed to an increase in the air-gap diameter) has a

Table 7.2: Comparison of time taken for the three optimisation methods to run 40 and 200 iterations of the 13kW generator.

Iterations	NSGA-II	PSO	MMFD
40	0.274	0.061	0.000945
200	1	1.31	0.000945

Table 7.3: Optimum key dimensions of the generators with 13kW.

	Surface-PM VFSG (Open slots)	Buried-PM VFSG
D_g[mm]	620	620
D_{out}[mm]	694.8	672.8
D_{in}[mm]	523.2	511
L_{stk}[mm]	135	135
h_{ss}[mm]	38.97	38.67
b_{ss}[mm]	13.47	13.47
h_{rs}[mm]	18.55	16.2
b_{rs}[mm]	15.8	15.8
N_s[turns]	80	140
$V_{no-load}$	1pu	0.995pu

penalty on the efficiency of the generator which reduces form the 95 % achieved by the optimum generator design. An interesting result is that a 16% increase in the generator mass still has a high efficiency output.

From the results of the design optimisation in Fig. 7.5, colour variation for each generator design candidate is used to show how deep the PMs are embedded in the rotor tooth core. It is observed that most of the optimum solutions have the PMs buried deep in the rotor tooth core (0.8 to 1with 1 being completely at the bottom of the tooth).

Table 7.2. shows that the choice of the optimisation method and the number of iterations influences the performance of the optimisation procedure. A choice with a high number of iterations, makes NSGA-II competitive with the PSO's solution time. For optimisation procedures with maximum number of iterations chosen to be 40, PSO has a faster convergence than NSGA-II. It takes 25 % of the time taken by NSGA-II (from Table 7.2) to converge but the accuracy of the minimum mass result does not consider the rotor copper-loss ratio.

The choice of the number of iterations is key in the optimisation of generator designs especially as it curbs the computational cost of optimisation algorithms.

With the properties of a fast non-dominated sorting procedure, an elitist strategy, a parameter-less approach and a simple yet efficient constraint-handling method, NSGA-II, is deemed the best choice for generator designs with many diverse solutions.

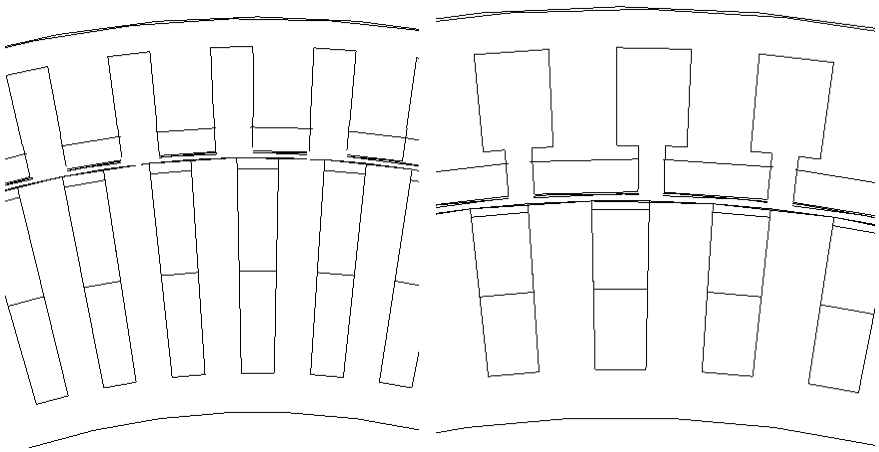

Figure 7.7: Wire-frame for drawing the designs in MagNet FE before material assignment for surface-PM generator designs with a) open slots, and b) semi-closed slots topologies.

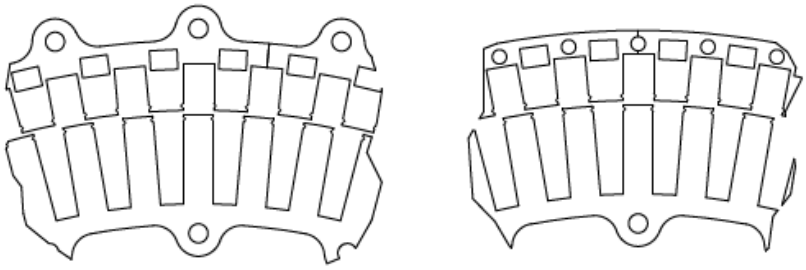

Figure 7.8: Buried-PM generator topology showing two different options to bolt the laminations into a stack.

7.2.1 Optimum generator design parameters

Comparison of the optimum generators of surface-PM and buried-PM shows that the buried-PM achieves higher efficiency and reduced rotor mass as shown in Table 7.1. The key dimensions of the topologies are given in Table 7.3. Cross-sections of the optimum designs are shown in Figures 7.7 to 7.9. As depicted in Figure 7.7, open slotted surface-PM design has a narrower slot size unlike for the semi-closed slots design which narrow teeth are applicable as the magnets have a pole-shoe for their placement. The flux densities in all the designs were ranging between 2 T to 2.26 T. This is with the highest being achieved by the surface-PM with semi-closed slots. The burried-PM topology has a low average flux density in the teeth and cores. However, around the magnets there is higher saturation. In the prototype design, this was put in consideration and the slots filed into circular ends. The full diagrams of the designs shown in Figure 7.10.

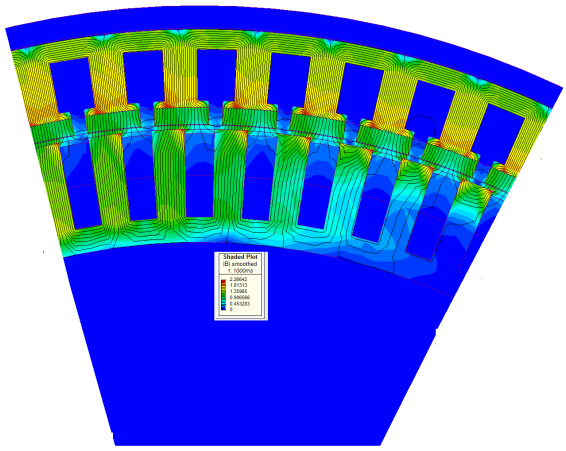

(a) Surface-PM VFSG design with semi-closed slots.

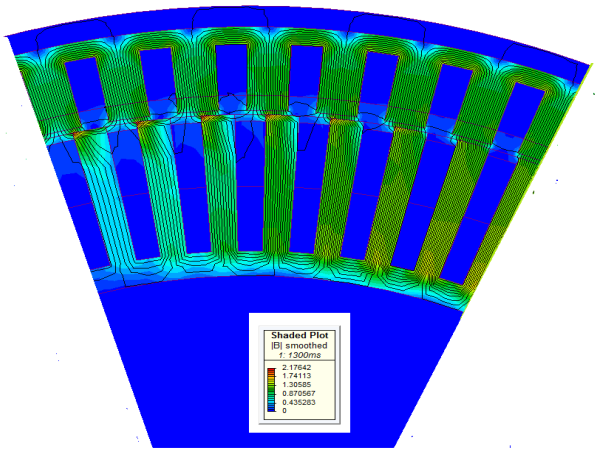

(b) Surface-PM open-slots design.

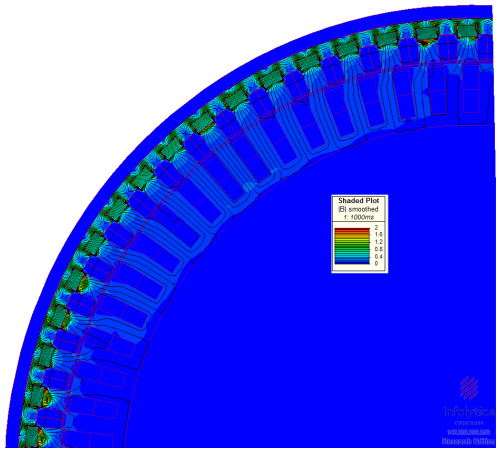

(c) Buried-PM design.

Figure 7.9: Flux density distribution in 2-D FEM for the three generator topologies.

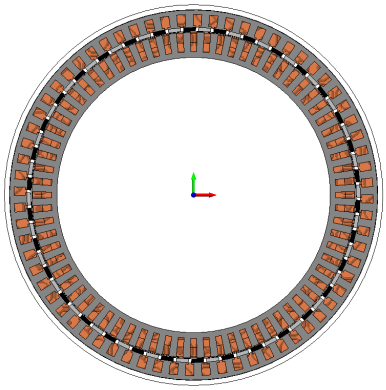

(a) Surface-PM with semi-closed slots

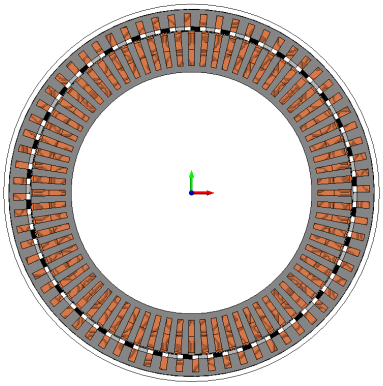

(b) Surface-PM with open slots

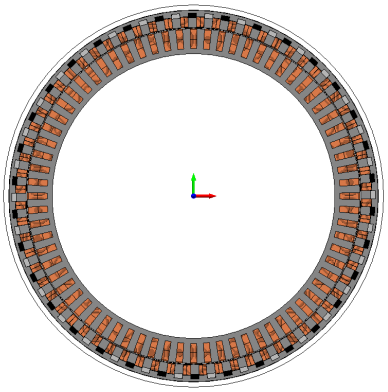

(c) Buried-PM design

Figure 7.10: Full PM VFSG designs in MagNet 2-D FEM for transient analysis.

Table 7.4: Time taken per unit for the non-gradient based optimisation methods (NSGA-II and PSO) to run 200 iterations for 13 kW, 100 kW and 1 MW power levels.

Power level (kW)	NSGA-II	PSO
13	1	1.31
100	0.925	0.915
1000	0.952	0.939

Table 7.5: Comparison of convergence time for a 13 kW generator with higher power levels to run 40 iterations.

Power level (kW)	NSGA-II	PSO	MMFD
13	0.274	0.061	0.000945
100	0.275	0.063	0.0018
1000	0.26	0.083	0.0013

7.3 Comparison with optimum designs of higher power levels

The larger generator designs achieve a higher efficiency due to the low current density, and larger air-gap diameter. With the core loss having a great influence on the large designs, a pan shape is achieved where the air-gap diameter is large but there is a short stack length, as shown in Figure 7.11.

The iron and copper masses for the various power levels are shown in Figure 7.12 where a very steep increase in iron mass is observed. This is attributed to the large diameters for the higher power levels and the need to achieve shallow slots.

7.3.1 Goodness functions for an optimum generator with power levels from 13 kW to 1 MW

The multi-objective comprises the minimisation of a total active mass and the rotor copper loss ratio. The total active mass of the generator constitutes $M_{tot} = M_{Fe} + M_{Cu} + M_{pm}$ i.e. M_{Fe} is the sum of stator and rotor iron masses, M_{Cu} is stator and rotor copper masses, as well as the PM mass M_{pm}. The goodness functions are defined from the rated power, total active mass, rated torque, air-gap volume, rotor copper loss, PM mass and the total loss in the generators. The five goodness functions are evaluated as follows

$$G_1 = Mass/Power,\ (kg/kW) \tag{7.1}$$

$$G_2 = Torque/volume,\ (kN/m^3) \tag{7.2}$$

$$G_3 = P_{Cu,r}/P_{rated},\ (W/kW) \tag{7.3}$$

$$G_4 = PMmass/volume,\ (kg/m^3) \tag{7.4}$$

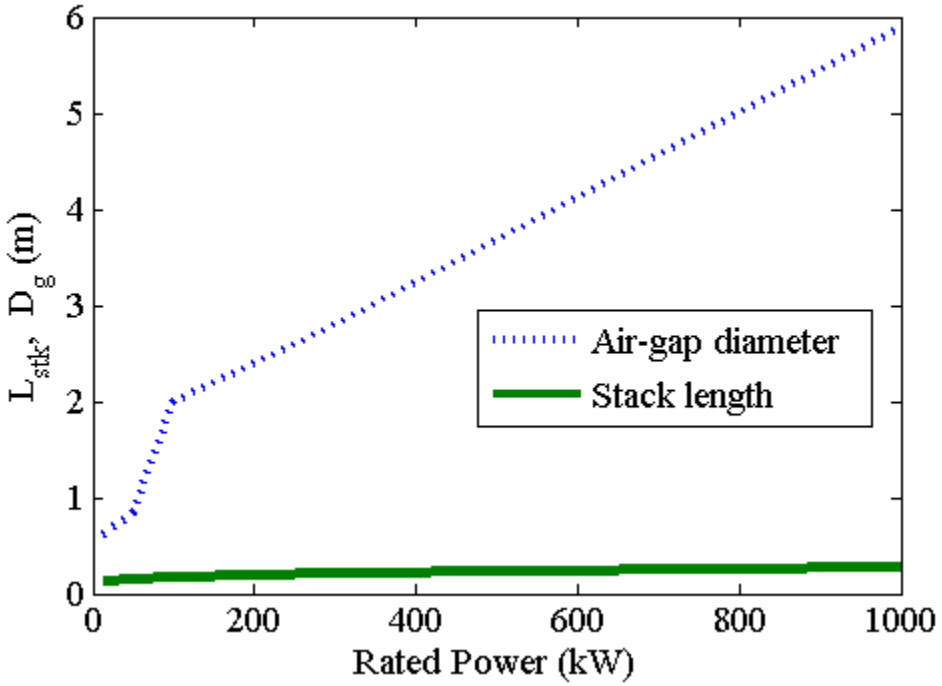

Figure 7.11: Stack length and air-gap diameter versus Power

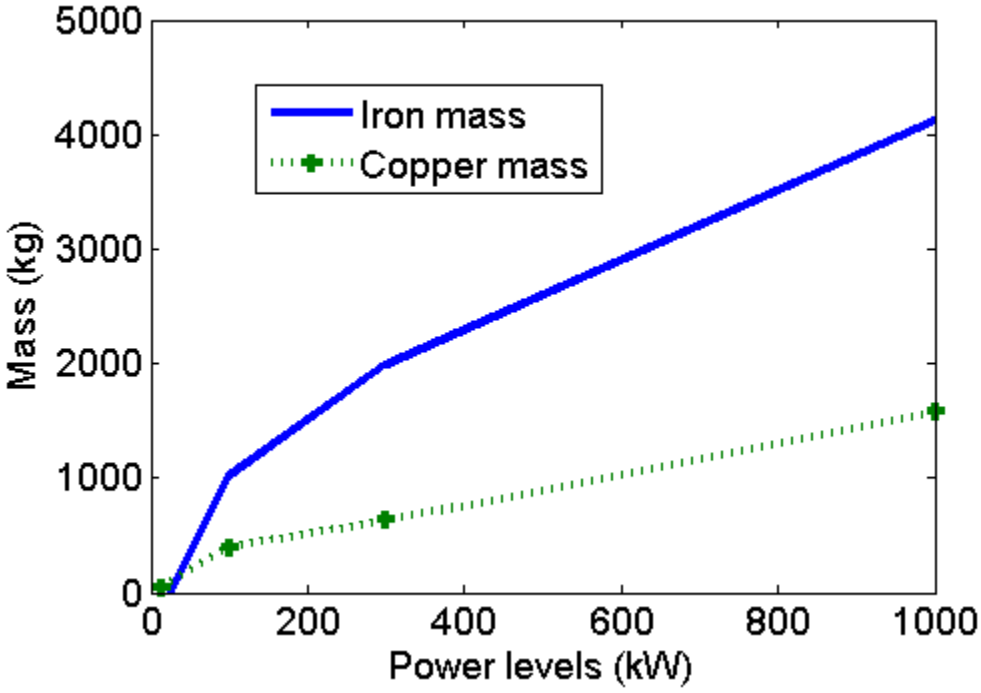

Figure 7.12: Variation in copper and iron mass with increase in power level.

Table 7.6: Optimisation results for optimum generators chosen from the pareto-fronts

Power level (kW)	13	100	1000
Efficiency	0.952	0.966	0.97
Current density J_s	4.12	4.0	4.0
Mass/power (kg/kW)	14.6	6.1	5.4
Torque density (kNm/m^3)	31.7	39.3	56.4
Torque per square root loss ($T_{rat}/\sqrt{P_{loss}}$)	1.75	11.71	75.8

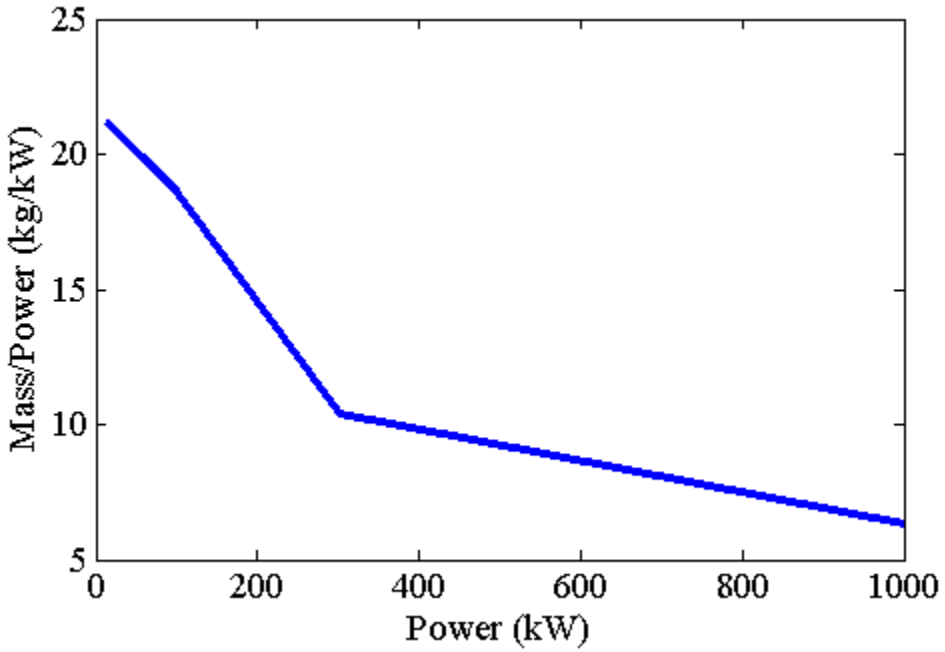

Figure 7.13: Mass/Power ratio -G_1 (kg/kW) as a function of power

$$G_5 = T_{rated}/\sqrt{P_{loss}},\ (kNm/kW) \tag{7.5}$$

7.3.1.1 Mass per power

The G_1 characteristic decreases with three different gradients with increase in rated power as shown in Figure 7.13. This is the total active mass for the electromagnetic part only. The weight of the generator structure is expected to be much higher than the active weight with an increase in power levels and should be evaluated as recommended for clarity. The results of mass per power can be compared to the one in literature such as [109], where 18 kg/kW was achieved for a 10 kW machine.

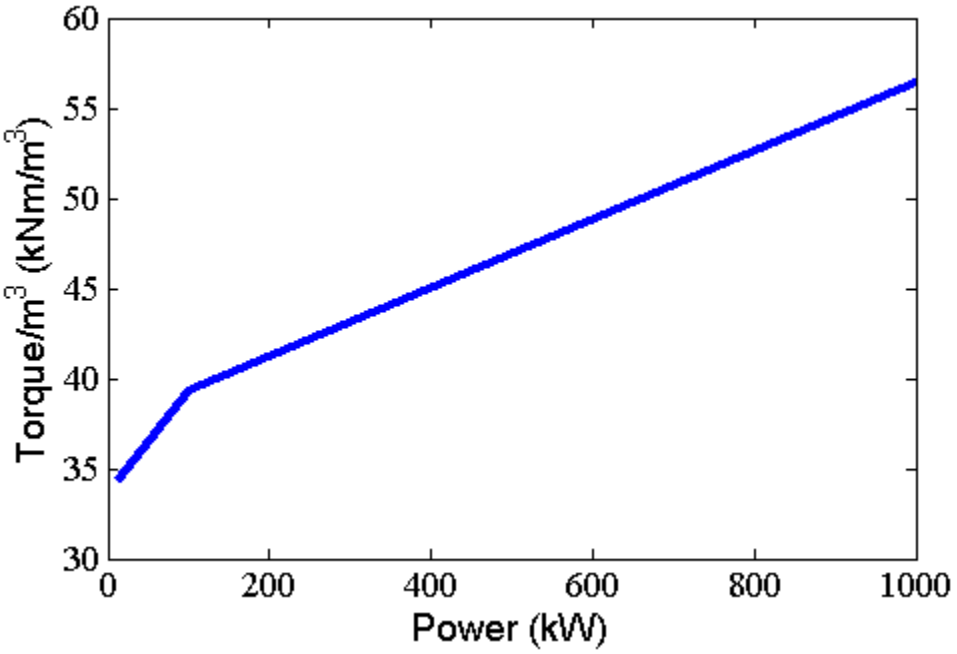

Figure 7.14: Torque densityG_2varies with rated power

7.3.1.2 Torque per Volume

The torque per volume of the generators increases with the rated power levels by a factor of 1.6 as shown in Figure 7.14. The established torque density of 56.4 kNm/m^3 for the 1 MW is very close to that of a 10 MW transverse flux generator with 57.42 kNm/m^3 achieved in [110].

7.3.1.3 PM mass per Volume

The volume used in this comparison is the air-gap volume. From Figure 7.15, it was observed that for power levels lower than 200 kW the PM mass per volume decreases steeply, then afterwards by a slight gradient as the power level increases. The larger generators have a lower minimum flux density in the magnets than the smaller ones, this reduces the demagnetisation risk, but none of the generators runs a risk of irreversible demagnetisation of the permanent magnets.

7.3.1.4 Torque per square root loss

The goodness function G_5 is as defined in [53] using the Response Surface (RS) and Differential Evolutionary (DE) algorithms on a permanent magnet synchronous motor (PMSM) design with 5 independent variables and a strong non-linear multi-objective pareto-front and on a function with 11 independent variables.

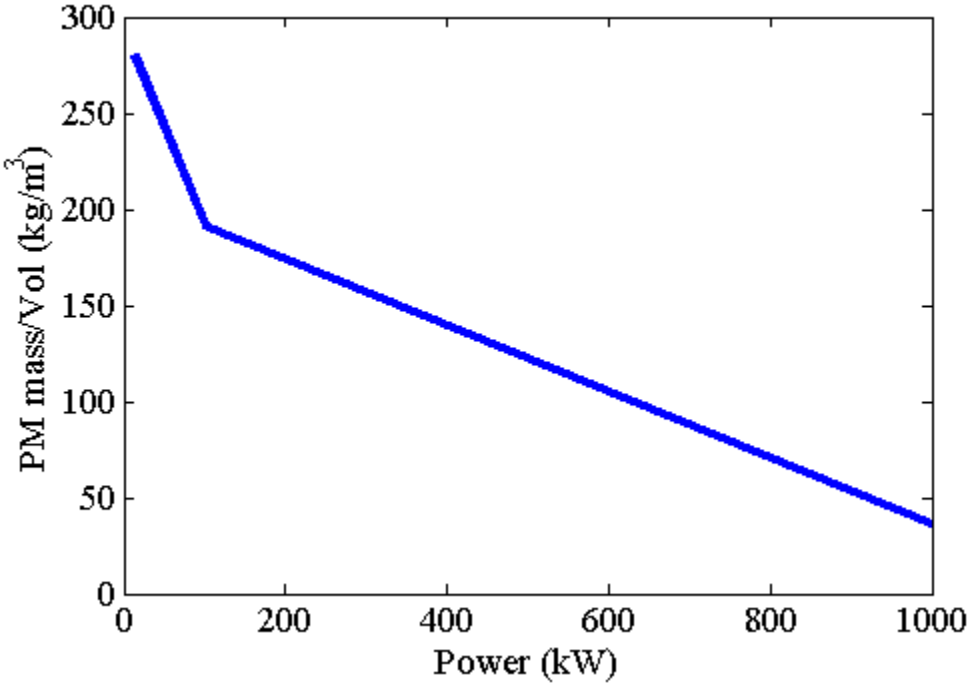

Figure 7.15: G_4versus power

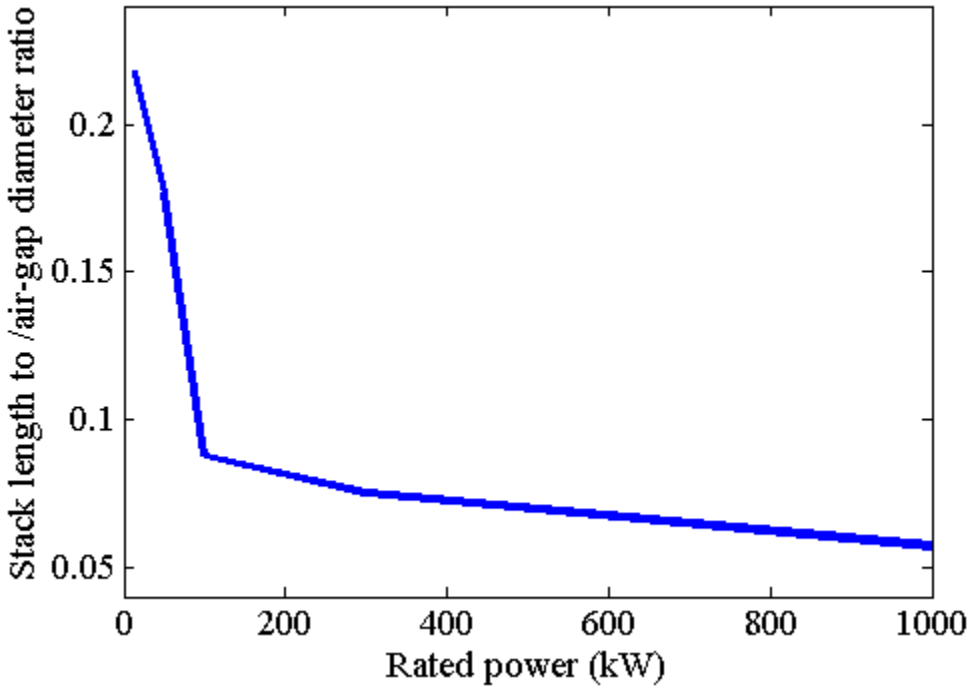

Figure 7.16: Stack length to air-gap diameter ratio for different power levels.

Table 7.6 presents the results of G_5 goodness function showing that for direct drive grid compliant generators, larger power levels are a good choice.

7.4 Observations and Conclusions

In this chapter makes the following major research contributions beyond those described in Chapter 6 are made:

(i) Detailed performance results for a 13 kW buried- and surface-PM VFSG and the optimum results of higher power levels are presented and discussed. It is shown that the buried-PM VFSG improves the rotor mass by 25% , and the magnets do not experience the influence of the harmonics from the non-overlap concentrated winding used in the stator.

(ii) The MMFD method is used iteratively and is faster than NSGA-II. However, the NSGA-II has the pareto-fronts that give the generator designer an opportunity to make an informed choice of the optimum design.

(iii) An extension of the $d-q$ analysis transformation is presented to optimise 100 kW generators and further a 1 MW generator and yields good results.

(iv) From the defined goodness factors defined in this work, it is observed that for direct drive wind turbine systems with direct grid connection, high power levels are a better choice for example the torque per volume for 13 kW is 1.7 times that of 1 MW generator, and 13 kW power level requires 7 times more of PM mass per volume (kg/m^3) when compared to a 1 MW grid compliant wind generator.

Finally, it is noted that the main contribution of this dissertation, to achieve a design through optimisation in FE has been achieved. This is shown by the optimum design candidates being obtained when the d_{pm} variable is close to one (i.e buried completely in the rotor tooth) specifically at the high power levels.

Chapter 8

Prototype

8.1 Rotor

The buried-PM topology had the rotor lamination cut in four pieces, one of which is shown in Figure 8.1a, then stacked together as shown in Figure 8.1c. The rotor-field-coils of this design are single layered, hence only 34 pre-formed coils needed to be manufactured. The coils were slid into the slots and a wedge placed at the end of the slots. A series connection of the rotor-field coils is then carried out.

The surface-PM design's lamination were cut into quarters for manufacturing issues as discussed in chapter 3. The PMs are glued in the rotor surface and latter winding done into the slots. Due to the semi-closed slots, prewound coils could not be used. The PMs are segmented to reduce losses. The segmentation is due to the non-overlap winding used in the stator which induces currents in the surface PMs.

From the experience in building the two rotor types, the advantages of pre-wound coils and their ease in manufacturing process was observed. The other advantage on the PM usage was on the buried-PM design where the magnets were easily fitted into the rotor cores. This is unlike in the surface-PM designs where the mounting of the PMs and gluing them was quite a task.

8.2 Stator

The stator assembly experience is generally as shown in Figure 8.3. The lamination as shown, has the teeth protruding to the outside, making it easy to fit pre-formed coils. The 72 coils with double layer configuration, can is also shown. From the top-view of the assembly of the stator the top and bottom placement of the coils is visible. The 2 mm air-gap size adopted for the generator made it easy to assemble the full stator into the rotor assembly as also shown in Figure 8.3.

Figure 8.1: Buried-PM rotor construction: showing the full lamination, quarter lamination, Inner view of the rotor stack with with single layer coils and wedges, side-view of the fully assembled rotor stack, series connection of coils yet to be done, top-view with the holed back plate, and lastly connected rotor coils.

Figure 8.2: Surface-PM rotor construction showing the lamination with outer bolting, surface mounted PMs and rotor field coils, closer view of the PM segmentation and the rotor coils, full view of the fully assembled rotor, and the ready polished rotor.

Figure 8.3: Stator prototype construction : stator lamination with teeth protruding to the outside, top-view of the stator with its support structure, side view showing wedges covering the slots, view of the double layer coils, and assembly of the stator into the rotor.

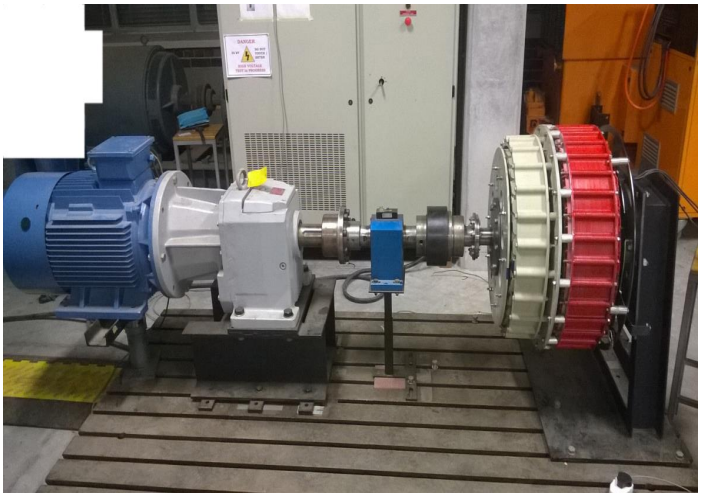

(a) Test-bench of the VFSG testing.

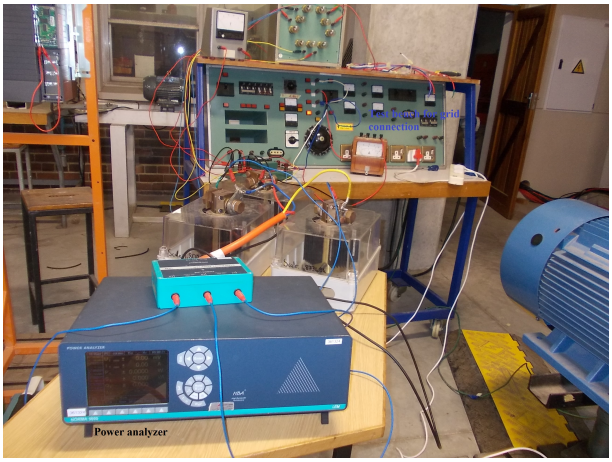

(b) Grid-connection

(c) Slip-coupler and VFSG with DC supply.

Figure 8.4: Test bench set-up a) The slip-synchronous generator connected to the prime-mover (an induction machine) through a shaft, b) power analyser and the grid connection bench, c) The slip-coupler and VFSG together, DC supply and grid power-electronics units.

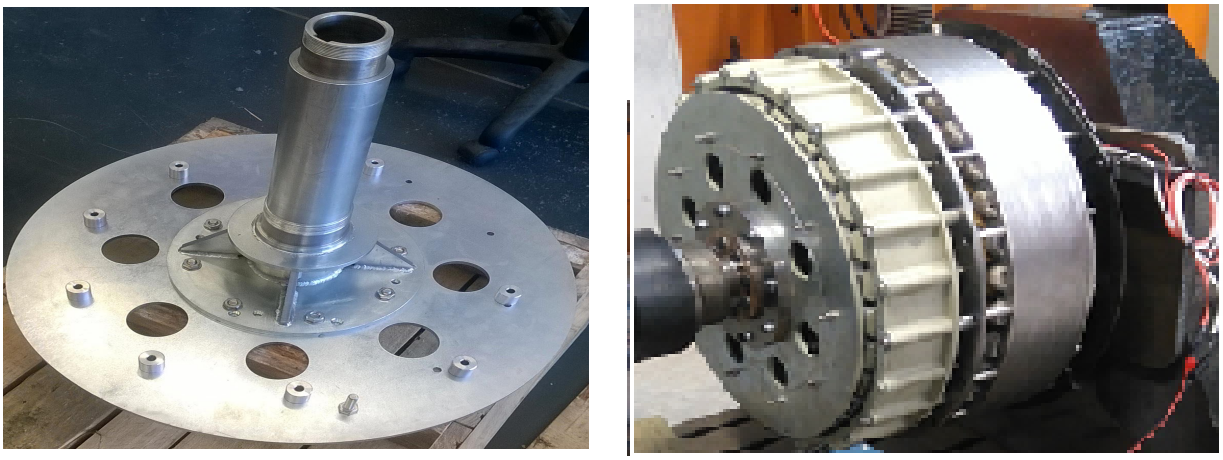

(a) Back-plate **(b)** Slip-IG and buried-PM VFSG

Figure 8.5: Slip-synchronous generator a) the back-plate for mounting of the slip-IG and support to the shaft. b) The slip-IG and SG assembled together.

8.3 Test-bench

Figure 8.4 shows the full test bench set up comprising a power analyser and the grid connection set-up, the rotor DC supply and grid requirements monitoring unit and the generator unit driven by a 45 kW induction machine and with a torque sensor in between them. The generator (S-SG unit) has its output directly connected to the grid via the norma.

8.4 Grid compliance test

8.4.1 No-load test

The rotor of the generator is rotated at the nominal speed by the prime mover. This no-load test was carried out with the objectives of i) to estimate the air gap flux density; ii) to determine the PM-induced voltage; iii) to study the no-load induced voltages (PM and I_{rfc}); iv) to build the no-load characteristic and v) to reveal the stator iron and mechanical losses. The initial test was the no-load PM induced voltage must be 1 pu (= 400 V line to line) as per the grid code requirement.

The first test was performed by measuring the open circuit back-EMF for the two generators with only PM excitation and at constant rated speed operation. The predicted no-load voltage waveform and that from the prototype tests depicted in Figure 8.6, a good agreement is observed. It is noted that the two generators have the same stator and the flux densities in the middle of the air-gap are thus as shown from Figure 8.7 in correlation of the two generator types.

Figure shows the no-load PM-induced phase voltage distributions in one phase. The measured RMS value for the surface-PM topology gave PM-induced line voltage of 395 V,

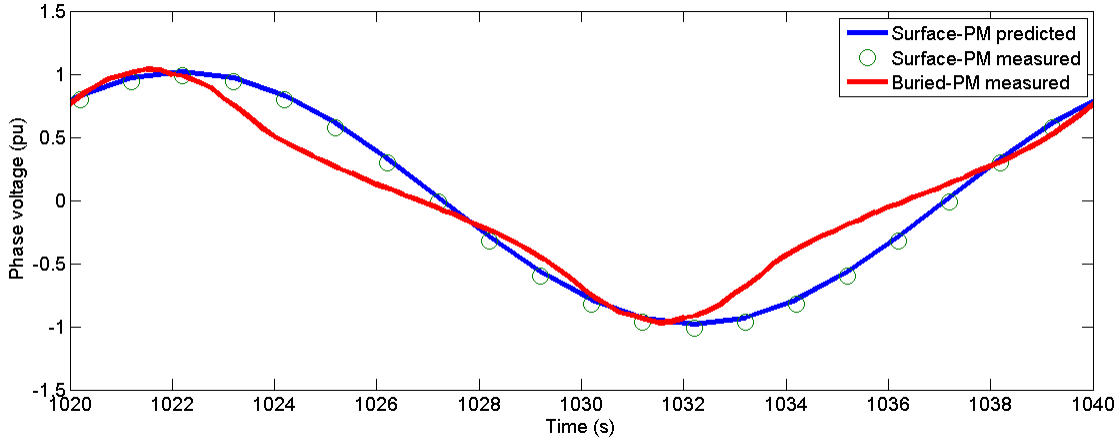

Figure 8.6: Comparison of measured and FEM no-load back-EMFs waveforms at rated speed for the prototype machines.

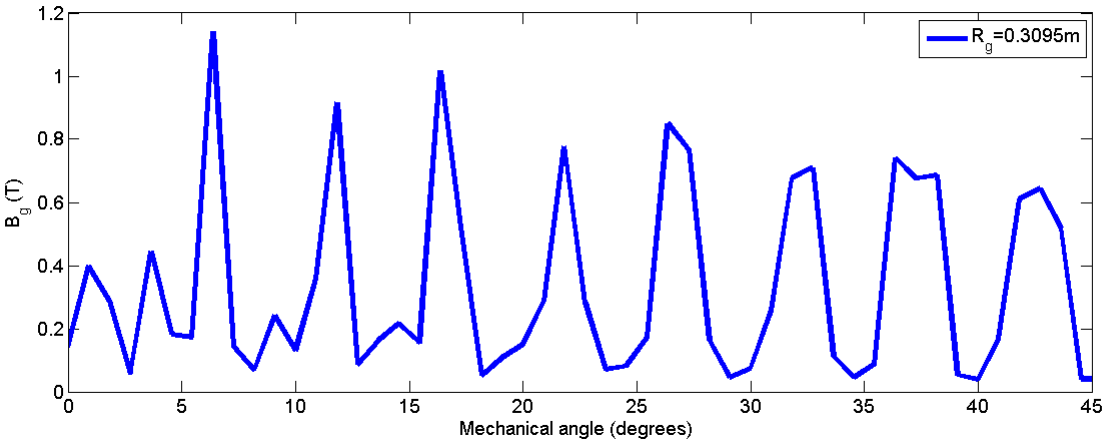

(a) Buried-PM generator

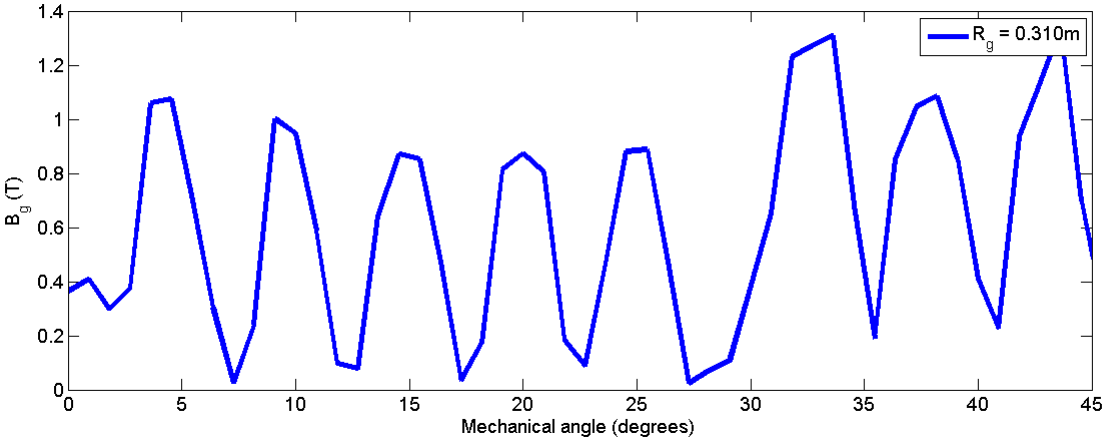

(b) Surface-PM generator

Figure 8.7: Comparison of air-gap flux densities for the prototype generators.

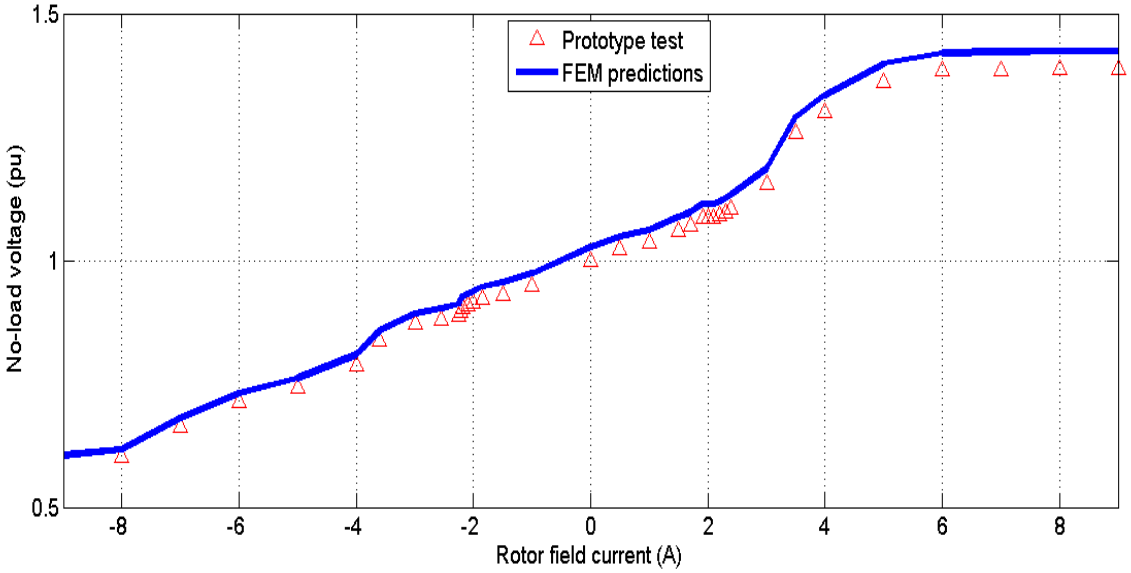

Figure 8.8: Rotor field current characteristics at no-load

while the predicted calculated value was 400 V, which is in good agreement. The buried-PM topology however had a discrepancy of 6.5 % between the measured and predicted. This discrepancy can be explained partly by the fact that the rotor bridge of 1mm allowed for a higher flux leakage. To increase the air-gap flux density and reduce the leakage a thinner rotor bridge can be adopted. Other possible reasons could be on manufacturing inaccuracies of the rotor poles or a slight variation in the PM material properties.

To measure the effect of the rotor field coil winding on the generators PM excitation, the stator winding of the prototype is open circuited and the field winding supplied with different DC currents values. The effect of these currents is The positive and negative direction of the rotor field current has an influence on the PM output voltage from 0.6 pu to 1.42 pu as illustrated in Figure 8.8. For the buried-PM topology, voltage variation had good agreement with predicted results as shown in Figure 8.8.

8.4.2 Thermal test

Thermal issues in PM machines are of importance. Hence, in this subsection, a thermal test is carried out to investigate the performance of the VFSG. The generator topology with the buried-PMs is adopted for this study. This is with the consideration that by the PMs being buried in the tooth core, natural cooling that is proposed for the generator designs might not be as effective as that with PMs on the rotor surface. The test is carried out at NO-load operation with two rotor field currents, 1 pu and 3 pu. The temperature rise in the rotor coils is shown in Figure 8.9a where for the two rotor field currents, the temperature rise does not go beyond 50^0 C. For the measurement in the rotor back yoke as depicted, in Figure 8.9b, the temperature variation is higher than in the coil ends. Temperatures

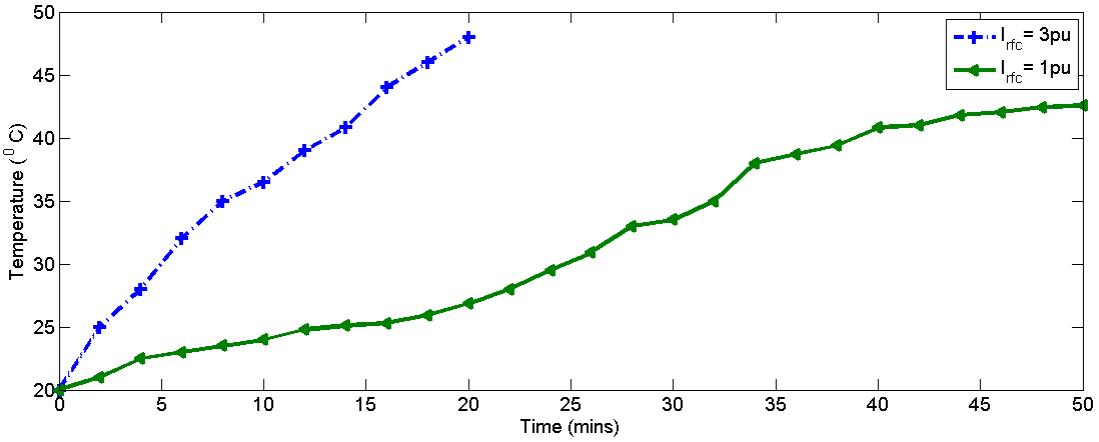

(a) Temperature variation in the rotor coils

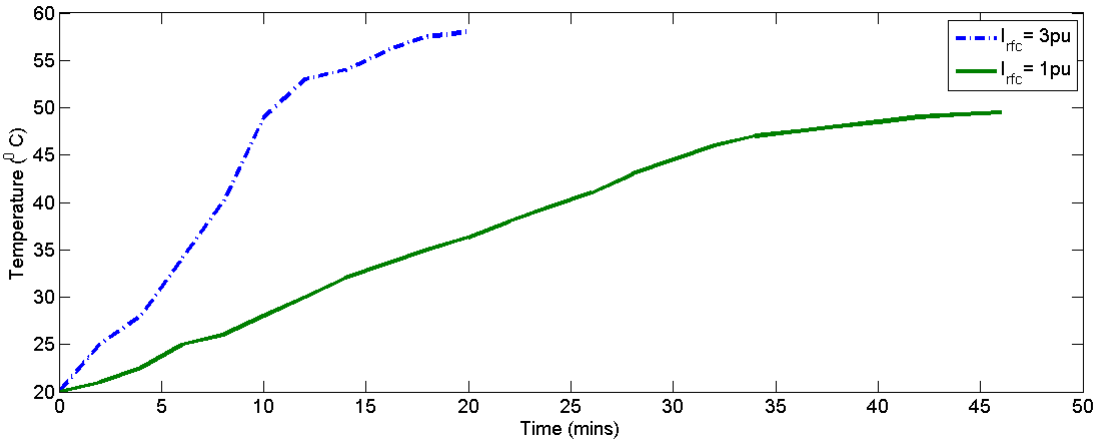

(b) Temperature variation in the rotor back yoke.

Figure 8.9: Temperature increase for the buried-PM VFSG operating at 1 pu and 3 pu (rotor current) boosting operation at NO-load.

with I_{rfc}= 3 pu reaching 60^0C in 20 minutes. The increase in the temperature is as was initially considered is due to the enclosed yoke mass whereas the coils are freely hanging and exposed to air circulation. These results conclude that a thinner lamination if considered would decrease the generators iron loss hence better cooling. With the buried-PM design, it is concluded that by burying the PMs in the rotor core does not impact on the thermal performance of the VFSG.

Chapter 9

Conclusions and Contributions

In this work, a direct-drive, radial flux, grid compliant PM VFSG is designed, optimised, built and tested. The generator is for use in a direct-drive directly grid connected slip-synchronous wind turbine system. The design is carried out using NdFeB rare earth PMs, copper coils and non-overlap concentrated windings in the stator. Analytical and FEM models are fully developed from design principles and important machine equations. An iterative analytical design is first carried out based on the total MMF requirement and general equations. Then an FE analysis is used for a detailed rotor design analysis and investigations. An optimisation procedure that uses FE and $d-q$ analysis is then carried out for further investigations and final adjustments. The topology allows PMs to be on the rotor surface or buried in the rotor tooth core. The topology further allows for non-overlap concentrated windings with short end windings. This enhances efficiency, cost (material and manufacturing cost are lower) and power to mass ratio.

The constant PM flux, is varied by the introduced rotor slots that are filled with coils. Depending on the direction of the current, the flux is either boosted or weakened. To further reduce the copper mass, the effective air-gap size is reduced by introducing slots in the rotor teeth where the PMs are placed. The teeth are straight to allow for pre-formed coils. The laminations are laser cut and produced in quarter sections.

The prototype generators were manufactured and tested. The results show good agreement between, theoretical predictions and practical measurements.

With regard to grid compliance, an important design consideration discussed in this dissertation is the choice of having the PMs produce the MMF required in the normal operation of the wind generator. In case of failure in the rotor field coils, the generator can still perform to its rated specifications. Another design consideration is the choice of rotor field coils excitation and the subsequent impact on the wind generator output voltage meeting the set grid code specifications from power system operators. It was found that the copper mass of the buried-PM VFSG is 42 % lower than that of the electrical excitation.

Optimum designs with power levels from 13 kW to 1 MW were further evaluated. They are all feasible as wind turbine generators with direct grid connection. The active weight

per kW and total cost per kW are about the same for all the generator sizes. The outer diameter of the proposed generator type, however, is not much larger than the conventional generator systems as the stator is on the inside.

From the conclusions stated and contributions, mentioned in section 9.1, one main conclusion with regard to the generator type optimised with the proposed method is that the use of buried-PM VFSG is the best topology for grid compliant wind turbine systems. This is shown from the results where the generator achieves the required flux-variation that lacks in PM generators and a mass saving when compared to the the conventional SG that is electrically excited. In addition it makes use of a converter with a very low power rating.

9.1 Contributions

A method to to carry out a design optimisation that considers both design and grid specifications has been demonstrated. This generic optimisation procedure for a PM VFSG is independent of the algorithm, and useful for sub 100 kW to MW level generators.

A design of a radial-flux PM VFSG with PMs buried in the rotor tooth has been presented for the first time. This design has the advantage that the PMs are not affected by MMF harmonics, and the design achieves a copper mass saving of 42% when compared to the non-PM excited SGs.

A first time demonstration of an optimum low speed PM VFSG compliant to grid codes (of voltage, power factor and reactive power control) is carried out.

This research forms an important foundation for direct-drive grid compliant PM VFSGs at low and high power levels for wind turbine application.

Bibliography

[1] G. Bywaters, V. John, J. Lynch, P. Mattila, G. Norton, J. Stowell, M. Salata, O. Labath, A. Chertok, D. Hablanian, and A. Laxson, "Northern power systems windpact drive train alternative design study report," National Renewable Energy Laboratory, Tech. Rep., 2005.

[2] F. Spinato, P. Tavner, G. van Bussel, and E. Koutoulakos, "Reliability of wind turbine subassemblies," *IET Renewable Power Generation*, vol. 3, no. 4, p. 387, 2009.

[3] H. Polinder, J. A. Ferreira, B. B. Jensen, A. B. Abrahamsen, K. Atallah, and R. A. McMahon, "Trends in wind turbine generator systems," *IEEE Journal of Emerging and Selected Topics in Power Electronics*, vol. 1, no. 3, pp. 174–185, Sep 2013.

[4] Y. Duan, R. Harley, and T. Habetler, "A useful multi-objective optimization design method for pm motors considering nonlinear material properties," in *Energy Conversion Congress and Exposition, 2009. ECCE 2009. IEEE.* IEEE, 2009, pp. 187–193.

[5] J. H. J. Potgieter and M. J. Kamper, "Design optimization of directly grid-connected pm machines for wind energy applications," *IEEE Transactions on Industry Applications*, vol. 51, no. 4, pp. 2949–2958, Jul 2015.

[6] L. L. Amuhaya and M. J. Kamper, "Effect of rotor field winding mmf on performance of grid-compliant hybrid-pm slip synchronous wind generator," *2016 IEEE PES PowerAfrica*, Jun 2016.

[7] J. Ribrant and L. M. Bertling, "Survey of failures in wind power systems with focus on swedish wind power plants during 1997–2005," *IEEE Transactions on Energy Conversion*, vol. 22, no. 1, pp. 167–173, Mar 2007.

[8] M. Ployard, A. Ammar, J. Iamamura, F. Gillon, L. Vido, and D. Laloy, "Multi-structure model to optimize a hybrid excitation synchronous generator," *2014 International Conference on Electrical Machines (ICEM)*, Sep 2014.

[9] H. Bali, Y. Amara, G. Barakat, R. Ibtiouen, and M. Gabsi, "Analytical modeling of open circuit magnetic field in wound field and series double excitation synchronous machines," *IEEE Transactions on Magnetics*, vol. 46, no. 10, pp. 3802–3815, 2010.

[10] L. L. Amuhaya and M. J. Kamper, "Design analysis of a hybrid-pm synchronous generator for wind energy applications," *2015 International Conference on the Domestic Use of Energy (DUE)*, Mar 2015.

[11] L. Amuhaya and M. Kamper, "Design by optimisation of a buried pm variable-flux wind generator for grid connection," in *Optimization of Electrical and Electronic Equipment (OPTIM) & 2017 Intl Aegean Conference on Electrical Machines and Power Electronics (ACEMP), 2017 International Conference on*. IEEE, 2017, pp. 305–310.

[12] V. D. Colli, F. Marignetti, and C. Attaianese, "Analytical and multiphysics approach to the optimal design of a 10-mw dfig for direct-drive wind turbines," *IEEE Transactions on Industrial Electronics*, vol. 59, no. 7, pp. 2791–2799, 2012.

[13] J. H. Potgieter and M. J. Kamper, "Design specifications and optimisation of a directly grid-connected pm wind generator," in *Energy Conversion Congress and Exposition (ECCE), 2013 IEEE*. IEEE, 2013, pp. 882–889.

[14] A. Daghigh, H. Javadi, and H. Torkaman, "Design optimization of direct-coupled ironless axial flux permanent magnet synchronous wind generator with low cost and high annual energy yield," *IEEE Transactions on Magnetics*, vol. 52, no. 9, pp. 1–11, 2016.

[15] S. Brisset, D. Vizireanu, and P. Brochet, "Design and optimization of a nine-phase axial-flux pm synchronous generator with concentrated winding for direct-drive wind turbine," *IEEE Transactions on industry applications*, vol. 44, no. 3, pp. 707–715, 2008.

[16] D. Svechkarenko, J. Soulard, and C. Sadarangani, "A novel transverse flux generator in direct-driven wind turbines," in *Proc. Nordic Workshop on Power and Industrial Electronics*, 2006.

[17] A. Zavvos, A. McDonald, and M. Mueller, "Electromagnetic and mechanical optimisation of direct-drive generators for large wind turbines," 2010.

[18] A. Zavvos, D.-j. Bang, A. McDonald, H. Polinder, and M. Mueller, "Structural analysis and optimisation of transverse flux permanent magnet machines for 5 and 10 mw direct drive wind turbines," *Wind Energy*, vol. 15, no. 1, pp. 19–43, 2012.

[19] J. B. A. Westlake and E. Spooner, "Damping the power-angle oscillations of a permanent-magnet synchronous generator with particular reference to wind turbine applications," *IEE Proc. Electric Power Applications*, vol. 143, no. 3, p. 269, 1996.

[20] A. B. M. T. H. Muller, M. Poller and J. Poster, "Grid compatibility of variable speed wind turbines with directly coupled synchronous generator and hydro-dynamically controlled gearbox," in *in Sixth International Workshop on Large-scale integration of*

wind power and transmission networks for offshore wind farms, Delft, Netherlands, Delft, Netherlands, 2006.

[21] K. Kamiev, A. Parviainen, and J. Pyrhonen, "Hybrid excitation synchronous generators for small hydropower plants," *2016 XXII International Conference on Electrical Machines (ICEM)*, Sep 2016.

[22] M. Ployard, F. Gillon, A. Ammar, D. Laloy, and L. Vido, "Hybrid excitation topologies of synchronous generator for direct drive wind turbine," in *Energy Conversion Congress and Exposition (ECCE), 2016 IEEE*. IEEE, 2016, pp. 1–7.

[23] D. Fodorean, A. Djerdir, I.-A. Viorel, and A. Miraoui, "A double excited synchronous machine for direct drive applicationâdesign and prototype tests," *IEEE Transactions on Energy Conversion*, vol. 22, no. 3, pp. 656–665, 2007.

[24] Y. Amara, L. Vido, M. Gabsi, E. Hoang, A. H. B. Ahmed, and M. Lecrivain, "Hybrid excitation synchronous machines: Energy-efficient solution for vehicles propulsion," *IEEE Transactions on Vehicular Technology*, vol. 58, no. 5, pp. 2137–2149, 2009.

[25] G. Borocci, F. G. Capponi, G. De Donato, and F. Caricchi, "Mixed-pole hybrid-excitation machine," *2014 International Conference on Electrical Machines (ICEM)*, Sep 2014.

[26] K. Kamiev, J. Nerg, J. Pyrhönen, V. Zaboin, V. Hrabovcová, and P. Rafajdus, "Hybrid excitation synchronous generators for island operation," *IET electric power applications*, vol. 6, no. 1, pp. 1–11, 2012.

[27] M. Liserre, R. Cardenas, M. Molinas, and J. Rodriguez, "Overview of multi-mw wind turbines and wind parks," *IEEE Transactions on Industrial Electronics*, vol. 58, no. 4, pp. 1081–1095, 2011.

[28] H. Nakai, K. Hiramoto, Y. Otani, and Y. Inaguma, "Novel field-weakening control method for an axial-flux permanent-magnet motor using an adjustable gap length," *JIASC IEEJ*, vol. 3, no. 64, pp. 337–342, 2007.

[29] R. O. . Z. Q. Z. . J. B. W. . D. A. S. . I. Urquhart, "Mechanically adjusted variable-flux concept for switched-flux permanent-magnet machines," 2011.

[30] L. Ma, M. Sanada, S. Morimoto, Y. Takeda, and N. Matsui, "High efficiency adjustable speed control of ipmsm with variable permanent magnet flux linkage," in *Industry Applications Conference, 1999. Thirty-Fourth IAS Annual Meeting. Conference Record of the 1999 IEEE*, vol. 2. IEEE, 1999, pp. 881–887.

[31] L. Del Ferraro, F. Caricchi, and F. G. Capponi, "Analysis and comparison of a speed-dependant and a torque-dependant mechanical device for wide constant power speed

range in afpm starter/alternators," *IEEE transactions on power electronics*, vol. 21, no. 3, pp. 720–729, 2006.

[32] L. Del Ferraro, F. G. Capponi, R. Terrigi, F. Caricchi, and O. Honorati, "Ironless axial flux pm machine with active mechanical flux weakening for automotive applications," in *Industry Applications Conference, 2006. 41st IAS Annual Meeting. Conference Record of the 2006 IEEE*, vol. 1. IEEE, 2006, pp. 1–7.

[33] M. M. Swamy, T. Kume, A. Maemura, and S. Morimoto, "Extended high-speed operation via electronic winding-change method for ac motors," *IEEE Transactions on Industry Applications*, vol. 42, no. 3, pp. 742–752, 2006.

[34] V. Ostovic, "Memory motors," *IEEE Industry Applications Magazine*, vol. 9, no. 1, pp. 52–61, 2003.

[35] ——, "Memory motorsâa new class of controllable flux pm machines for a true wide speed operation in proc [c]. thirty-sixth ias annual meeting," in *Conference Record of the 2001 IEEE*, vol. 4, no. 9, 2001, p. 9.

[36] X. Zhu, M. Cheng, W. Hua, J. Zhang, and W. Zhao, "Design and analysis of a new hybrid excited doubly salient machine capable of field control," in *Industry Applications Conference, 2006. 41st IAS Annual Meeting. Conference Record of the 2006 IEEE*, vol. 5. IEEE, 2006, pp. 2382–2389.

[37] L. Xiping, L. Heyun, Y. Chengfeng, F. Shuhua, and G. Jian, "A novel dual-stator hybrid excited synchronous wind generator," *2007 7th International Conference on Power Electronics and Drive Systems*, Nov 2007.

[38] E. B. Sulaiman and A. M. Arab, "Fundamental study of outer-rotor hybrid excitation flux switching generator for grid connected wind turbine applications," in *Research and Development (SCOReD), 2015 IEEE Student Conference on*. IEEE, 2015, pp. 716–720.

[39] L. Ma, M. Sanada, S. Morimoto, and Y. Takeda, "Advantages of ipmsm with adjustable pm armature flux linkage in efficiency improvement and operating range extension," in *Power Conversion Conference, 2002. PCC-Osaka 2002. Proceedings of the*, vol. 1. IEEE, 2002, pp. 136–141.

[40] N. Bianchi, S. Bolognani, M. D. Pre, and G. Grezzani, "Design considerations for fractional-slot winding configurations of synchronous machines," *IEEE transactions on industry applications*, vol. 42, no. 4, pp. 997–1006, 2006.

[41] N. Bianchi, S. Bolognani, and M. Dai Pre, "Magnetic loading of fractional-slot three-phase pm motors with nonoverlapped coils," *IEEE Transactions on Industry Applications*, vol. 44, no. 5, pp. 1513–1521, Sep 2008.

[42] J. Baek, M. M. Rahimian, and H. A. Toliyat, "Optimal design and comparison of stator winding configurations in permanent magnet assisted synchronous reluctance generator," in *Proc. IEEE Int. Electric Machines and Drives Conf*, May 2009, pp. 732–737.

[43] A. Di Gerlando, G. Foglia, M. F. Iacchetti, and R. Perini, "Axial flux pm machines with concentrated armature windings: Design analysis and test validation of wind energy generators," *IEEE Transactions on Industrial Electronics*, vol. 58, no. 9, pp. 3795–3805, Sep 2011.

[44] A. EL-Refaie, "Fractional-slot concentrated-windings synchronous permanent magnet machines: Opportunities and challenges," *IEEE Transactions on Industrial Electronics*, vol. 57, no. 1, pp. 107–121, Jan 2010.

[45] K. Ahsanullah, R. Dutta, and M. Rahman, "Analysis of low-speed ipmms with distributed and fractional slot concentrated windings for wind energy applications," *IEEE Transactions on Magnetics*, 2017.

[46] L. Amuhaya and M. Kamper, "Design and optimisation of variable-flux synchronous generators over the grid-code range using analytical and pso methods," in *Domestic Use of Energy (DUE), 2017 International Conference on*. IEEE, 2017, pp. 160–166.

[47] J. Y. Chen, C. Nayar, and L. Xu, "Design and fe analysis of an outer-rotor pm generator for directly-coupled wind turbine applications," *Conference Record of 1998 IEEE Industry Applications Conference. Thirty-Third IAS Annual Meeting (Cat. No.98CH36242)*.

[48] O. Laldin, S. D. Sudhoff, and S. Pekarek, "An analytical design model for wound rotor synchronous machines," *IEEE Transactions on Energy Conversion*, vol. 30, no. 4, pp. 1299–1309, Dec 2015.

[49] Magnet. [Online]. Available: http://www.infolytica.com

[50] L. Amuhaya and M. Kamper, "Design and optimisation of grid compliant variable-flux pm synchronous generator for wind turbine applications," in *Energy Conversion Congress and Exposition (ECCE), 2015 IEEE*. IEEE, 2015, pp. 829–836.

[51] H. Gorginpour, H. Oraee, and R. A. McMahon, "A novel modeling approach for design studies of brushless doubly fed induction generator based on magnetic equivalent circuit," *IEEE Transactions on Energy Conversion*, vol. 28, no. 4, pp. 902–912, 2013.

[52] X. Wang, T. D. Strous, D. Lahaye, H. Polinder, and J. A. Ferreira, "Finite element modeling of brushless doubly-fed induction machine based on magneto-static simulation," in *Electric Machines & Drives Conference (IEMDC), 2015 IEEE International*. IEEE, 2015, pp. 315–321.

[53] Y. Duan and D. M. Ionel, "A review of recent developments in electrical machine design optimization methods with a permanent-magnet synchronous motor benchmark study," *IEEE Transactions on Industry Applications*, vol. 49, no. 3, pp. 1268–1275, 2013.

[54] X. Meng, S. Wang, J. Qiu, J. G. Zhu, Y. Wang, Y. Guo, D. Liu, and W. Xu, "Dynamic multilevel optimization of machine design and control parameters based on correlation analysis," *IEEE Transactions on magnetics*, vol. 46, no. 8, pp. 2779–2782, 2010.

[55] J. Legranger, G. Friedrich, S. Vivier, and J. C. Mipo, "Combination of finite-element and analytical models in the optimal multidomain design of machines: Application to an interior permanent-magnet starter generator," *IEEE Transactions on Industry Applications*, vol. 46, no. 1, pp. 232–239, 2010.

[56] N. Boules, "Design optimization of permanent magnet dc motors," *IEEE Transactions on Industry Applications*, vol. 26, no. 4, pp. 786–792, 1990.

[57] S. B. Kwon, S. J. Park, and J. H. Lee, "Optimum design criteria based on the rated watt of a synchronous reluctance motor using a coupled fem and sumt," *IEEE Transactions on Magnetics*, vol. 41, no. 10, pp. 3970–3972, 2005.

[58] S. J. Mun, Y. H. Cho, and J. H. Lee, "Optimum design of synchronous reluctance motors based on torque/volume using finite-element method and sequential unconstrained minimization technique," *IEEE Transactions on Magnetics*, vol. 44, no. 11, pp. 4143–4146, 2008.

[59] D. A. Kocabas, "Novel winding and core design for maximum reduction of harmonic magnetomotive force in ac motors," *IEEE Transactions on Magnetics*, vol. 45, no. 2, pp. 735–746, 2009.

[60] L. Chedot, G. Friedrich, J.-M. Biedinger, and P. Macret, "Integrated starter generator: The need for an optimal design and control approach. application to a permanent magnet machine," *IEEE Transactions on Industry Applications*, vol. 43, no. 2, pp. 551–559, 2007.

[61] K. Idir, L. Chang, and H. Dai, "Error-based global optimization approach for electric motor design," *IEEE transactions on magnetics*, vol. 34, no. 5, pp. 2861–2864, 1998.

[62] V. Gradinaru, L. Tutelea, and I. Boldea, "25 kw, 15 krpm, 6/4 pmsm: Optimal design and torque pulsation reduction via fem," in *Optimization of Electrical and Electronic Equipment, 2008. OPTIM 2008. 11th International Conference on.* IEEE, 2008, pp. 249–256.

[63] F. Messine, B. Nogarede, and J.-L. Lagouanelle, "Optimal design of electromechanical actuators: a new method based on global optimization," *IEEE transactions on magnetics*, vol. 34, no. 1, pp. 299–308, 1998.

[64] M. Celebi, "Weight optimisation of a salient pole synchronous generator by a new genetic algorithm validated by finite element analysis," *IET Electric Power Applications*, vol. 3, no. 4, pp. 324–333, 2009.

[65] S.-Y. Jung, J.-K. Kim, H.-K. Jung, C.-G. Lee, and S.-K. Hong, "Size optimization of steel-cored pmlsm aimed for rapid and smooth driving on short reciprocating trajectory using auto-tuning niching genetic algorithm," *IEEE Transactions on Magnetics*, vol. 40, no. 2, pp. 750–753, 2004.

[66] Y. Del Valle, G. K. Venayagamoorthy, S. Mohagheghi, J.-C. Hernandez, and R. G. Harley, "Particle swarm optimization: basic concepts, variants and applications in power systems," *IEEE Transactions on evolutionary computation*, vol. 12, no. 2, pp. 171–195, 2008.

[67] V. Cingoski, K. Kaneda, H. Yamashita, and N. Kowata, "Inverse shape optimization using dynamically adjustable genetic algorithms [electric machine design]," *IEEE Transactions on Energy Conversion*, vol. 14, no. 3, pp. 661–666, 1999.

[68] L. Jolly, M. Jabbar, and L. Qinghua, "Optimization of the constant power speed range of a saturated permanent-magnet synchronous motor," *IEEE Transactions on Industry Applications*, vol. 42, no. 4, pp. 1024–1030, 2006.

[69] ——, "Design optimization of permanent magnet motors using response surface methodology and genetic algorithms," *IEEE Transactions on Magnetics*, vol. 41, no. 10, pp. 3928–3930, 2005.

[70] O. A. Mohammed and G. Uler, "A hybrid technique for the optimal design of electromagnetic devices using direct search and genetic algorithms," *IEEE Transactions on Magnetics*, vol. 33, no. 2, pp. 1931–1934, 1997.

[71] N. Bianchi and S. Bolognani, "Design optimisation of electric motors by genetic algorithms," *IEE Proceedings-Electric Power Applications*, vol. 145, no. 5, pp. 475–483, 1998.

[72] G. F. Uler and O. A. Mohammed, "Utilizing genetic algorithms for the optimal design of electromagnetic devices," in *Southeastcon'95. Visualize the Future., Proceedings., IEEE.* IEEE, 1995, pp. 92–95.

[73] Y. Ahn, J. Park, C.-G. Lee, J.-W. Kim, and S.-Y. Jung, "Novel memetic algorithm implemented with ga (genetic algorithm) and mads (mesh adaptive direct search) for

optimal design of electromagnetic system," *IEEE Transactions on Magnetics*, vol. 46, no. 6, pp. 1982–1985, 2010.

[74] J. Robinson and Y. Rahmat-Samii, "Particle swarm optimization in electromagnetics," *IEEE transactions on antennas and propagation*, vol. 52, no. 2, pp. 397–407, 2004.

[75] R. Wrobel and P. H. Mellor, "Design considerations of a direct drive brushless machine with concentrated windings," *IEEE Transactions on energy conversion*, vol. 23, no. 1, pp. 1–8, 2008.

[76] A. Røkke, "Gradient based optimization of permanent magnet generator design for a tidal turbine," in *Proc. Int. Conf. Elect. Mach.(ICEM)*, 2014, pp. 1199–1205.

[77] Y. Duan and R. G. Harley, "A novel method for multiobjective design and optimization of three phase induction machines," *IEEE Transactions on Industry Applications*, vol. 47, no. 4, pp. 1707–1715, 2011.

[78] H.-I. Lee and M. D. Noh, "Optimal design of radial-flux toroidally wound brushless dc machines," *IEEE Transactions on Industrial Electronics*, vol. 58, no. 2, pp. 444–449, 2011.

[79] K. R. Davey and B. B. Gamble, "Numerical design of synchronous generators," *IEEE transactions on magnetics*, vol. 41, no. 8, pp. 2391–2397, 2005.

[80] W. Wu, J. B. Dunlop, S. J. Collocott, and B. A. Kalan, "Design optimization of a switched reluctance motor by electromagnetic and thermal finite-element analysis," *IEEE Transactions on Magnetics*, vol. 39, no. 5, pp. 3334–3336, 2003.

[81] M. A. Alhamadi and N. Demerdash, "Optimization of the skew angle of rotor poles in permanent magnet machines based on the inverse problem method," *IEEE Transactions on Energy Conversion*, vol. 14, no. 4, pp. 1496–1501, 1999.

[82] S. Sivanandam and S. Deepa, "Genetic algorithms," in *Introduction to Genetic Algorithms*. Springer, 2008, pp. 15–37.

[83] A. H. Isfahani, B. Ebrahimi, and H. Lesani, "Design optimization of a low-speed single-sided linear induction motor for improved efficiency and power factor," *IEEE transactions on magnetics*, vol. 44, no. 2, pp. 266–272, 2008.

[84] D. Lee, S. Lee, J.-W. Kim, C.-G. Lee, and S.-Y. Jung, "Intelligent memetic algorithm using ga and guided mads for the optimal design of interior pm synchronous machine," *IEEE Transactions on Magnetics*, vol. 47, no. 5, pp. 1230–1233, 2011.

[85] S.-H. Kim and S.-Y. Jung, "Optimal design of direct-driven wind generator using genetic algorithm combined with expert system," *Journal of the Korean Institute of Illuminating and Electrical Installation Engineers*, vol. 24, no. 10, pp. 149–156, 2010.

[86] S. Han, I. Muta, T. Hoshino, T. Nakamura, and N. Maki, "Optimal design of superconducting generator using genetic algorithm and simulated annealing," *IEE Proceedings-Electric Power Applications*, vol. 151, no. 5, pp. 543–554, 2004.

[87] V. Puri, Y. K. Chauhan, and N. Singh, "Design optimization of permanent magnet synchronous machine for vertical axis wind turbine using gravitational search algorithm," in *Recent Advances in Engineering & Computational Sciences (RAECS), 2015 2nd International Conference on*. IEEE, 2015, pp. 1–6.

[88] S. Mendaci, M. Boulouh, S. Gouaidia, and A. Ladjimi, "Ant colony for optimal design of pm synchronous generator for direct-drive wind turbines," in *Electrical Sciences and Technologies in Maghreb (CISTEM), 2014 International Conference on*. IEEE, 2014, pp. 1–8.

[89] A. Tessarolo, F. Luise, P. Raffin, and V. Venuti, "Multi-objective design optimization of a surface permanent-magnet slotless alternator for small power wind generation," in *Clean Electrical Power (ICCEP), 2011 International Conference on*. IEEE, 2011, pp. 371–376.

[90] M. M. A. Bazghaleh, M. Naghashan, "Optimum design of single-sided linear induction motors for improved motor performance," *IEEE Trans. Magn.*, vol. 46, no. 11, pp. 3939–3947, 2010.

[91] S. K. C. L. J. Seo, C. Im and H. Jung, "An improved particle swarm optimization algorithm mimicking territorial dispute between groups for multimodal function optimization problems," *IEEE Transactions on Magnetics*, vol. 44, no. 6, p. 1046â1049, 2008.

[92] S. K. J. Seo and H. Jung, "Rotor-design strategy of ipmsm for 42 v integrated starter generator," *IEEE Transactions on Magnetics*, vol. 46, no. 6, p. 2458â2461, 2010.

[93] L. Z. B. L. dos Santos Coelho and L. Lebensztajn, "Multiobjective particle swarm approach for the design of a brushless dc wheel motor," *IEEE Transactions on Magnetics*, vol. 46, no. 8, p. 2994â2997, 2010.

[94] V. Huang, A. Qin, K. Deb, E. Zitzler, P. Suganthan, J. Liang, M. Preuss, and S. Huband, "Problem definitions for performance assessment of multi-objective optimization algorithms," 2007.

[95] G. B. L. C. A. Coello and D. A. V. Veldhuizen, *Evolutionary Algorithms for Solving Multi-Objective Problems*. Springer, 2007.

[96] K. K. S. Huang and J. Lee, "Homogeneous particle swarm optimizer for multi-objective optimization problem," 2005.

[97] K. Deb, A. Pratap, S. Agarwal, and T. Meyarivan, "A fast and elitist multiobjective genetic algorithm: Nsga-ii," *IEEE Transactions on Evolutionary Computation*, vol. 6, no. 2, pp. 182–197, Apr. 2002.

[98] T. Bazzo, J. F. Kolzer, R. Carlson, F. Wurtz, and L. Gerbaud, "Optimum design of a high-efficiency direct-drive pmsg," in *Energy Conversion Congress and Exposition (ECCE), 2015 IEEE*. IEEE, 2015, pp. 1856–1863.

[99] T. d. P. M. Bazzo, J. F. Kölzer, R. Carlson, F. Wurtz, and L. Gerbaud, "Multidisciplinary design optimization of a direct-drive pmsg including the power converter cost and losses," in *Electrical Machines (ICEM), 2016 XXII International Conference on*. IEEE, 2016, pp. 1909–1914.

[100] A. McDonald and N. A. Bhuiyan, "On the optimization of generators for offshore direct drive wind turbines," *IEEE Transactions on Energy Conversion*, vol. 32, no. 1, pp. 348–358, 2017.

[101] J. K. Nøland, F. Evestedt, J. J. Pérez-Loya, J. Abrahamsson, and U. Lundin, "Design and characterization of a rotating brushless outer pole pm exciter for a synchronous generator," *IEEE Transactions on Industry Applications*, vol. 53, no. 3, pp. 2016–2027, 2017.

[102] P. Han, M. Cheng, Y. Jiang, and Z. Chen, "Torque/power density optimization of a dual-stator brushless doubly-fed induction generator for wind power application," *IEEE Transactions on Industrial Electronics*, 2017.

[103] E. L. Engevik, A. Røkke, and R. Nilssen, "Evaluating hybrid optimization algorithms for design of a permanent magnet generator," in *Electrical Machines & Power Electronics (ACEMP), 2015 Intl Conference on Optimization of Electrical & Electronic Equipment (OPTIM) & 2015 Intl Symposium on Advanced Electromechanical Motion Systems (ELECTROMOTION), 2015 Intl Aegean Conference on*. IEEE, 2015, pp. 711–718.

[104] T. D. Strous, X. Wang, H. Polinder, and J. B. Ferreira, "Finite element based multi-objective optimization of a brushless doubly-fed induction machine," in *Electric Machines & Drives Conference (IEMDC), 2015 IEEE International*. IEEE, 2015, pp. 1689–1694.

[105] W. Qiao, L. Qu, and R. G. Harley, "Control of ipm synchronous generator for maximum wind power generation considering magnetic saturation," *IEEE Transactions on industry applications*, vol. 45, no. 3, pp. 1095–1105, 2009.

[106] Z. Wu, R. Qu, J. Li, H. Fang, and Z. Fu, "Structure optimization of rotor supporting of permanent magnet direct drive synchronous generators for large wind turbine

based on genetic algorithm and finite element method," in *Electric Machines & Drives Conference (IEMDC), 2015 IEEE International*. IEEE, 2015, pp. 1755–1760.

[107] G. Y. Sizov, D. M. Ionel, and N. A. Demerdash, "Modeling and parametric design of permanent-magnet ac machines using computationally efficient finite-element analysis," *IEEE Transactions on Industrial Electronics*, vol. 59, no. 6, pp. 2403–2413, 2012.

[108] D. M. Ionel and M. Popescu, "Ultrafast finite-element analysis of brushless pm machines based on space–time transformations," *IEEE Transactions on Industry Applications*, vol. 47, no. 2, pp. 744–753, 2011.

[109] J. Pippuri, A. Manninen, J. Keränen, and K. Tammi, "Torque density of radial, axial and transverse flux permanent magnet machine topologies," *IEEE Transactions on Magnetics*, vol. 49, no. 5, pp. 2339–2342, 2013.

[110] A. Tovar-Barranco, D. Gómez, A. López-de Heredia, and I. Villar, "High torque density transverse flux permanent magnet machine design for wind power generation," in *Electrical Machines (ICEM), 2016 XXII International Conference on*. IEEE, 2016, pp. 782–788.